

POLITECNICO DI TORINO

Master's Degree in Nanotechnologies for ICT



Master's Degree Thesis

Sc-doped AlN: high performance piezoelectric MEMS resonators and high-polarization ferroelectric

Supervisors

Prof. Matteo COCUZZA

Prof. Stefano STASSI

Prof. Matteo RINALDI

Candidate

Gabriel GIRIBALDI

October 2020

Abstract

The present Master's Thesis regards the impact of Scandium doping on Aluminum Nitride (AlN) thin films. Two very interesting applications of Sc-doped AlN (ScAlN) are treated in depth, namely the improvement in MEMS piezoelectric resonator performances and the study of its ferroelectric properties. While the first study poses itself as an optimization of something already present, the second one represents a step towards the opening of new research lines. The present work is divided into three main Chapters.

The first one is the introduction of the Thesis work, describing the state of the art in the field of MEMS resonators. Moreover, physical descriptions of the phenomena of piezoelectricity and ferroelectricity, the ones on which the studied technologies rely, are given. Finally, the electrical description of piezoelectric MEMS resonators, together with the working mechanisms of a specific topology of filters which uses them as building blocks, are given.

The second chapter introduces a relatively new technology of piezoelectric MEMS resonators called Cross-Sectional Lamé' Mode Resonator (CLMR) and explains why it poses itself as an improvement to the current state of the art. A systematic optimization study is performed on AlN CLMRs, concerning both the geometrical structure and the electrode materials. Moreover, the impact of Scandium doping of AlN thin films is quantified as regards the performances of CLMRs, obtaining noteworthy improvements compared to the case of pure AlN. In addition, two experimental plans have been designed and clearly described in order to verify the theoretical and simulation analysis, one on AlN and the other on 30% doped ScAlN.

The third chapter regards ScAlN ferroelectricity. Firstly, an explanation of the appearance of this phenomenon is given, together with the applications that such a discovery is able to open in the field of RF MEMS. After that, descriptions of the employed thin films sputtering and characterization tools are given. With those, experimental results obtained on ScAlN ferroelectric capacitors fabricated in-house are shown, with interesting considerations on how the film properties vary according to different deposition and measurement parameters. Finally, for the first time, a Finite Element Model (FEM) utilizing the commercial software COMSOL Multiphysics able to describe the behaviour of ferroelectric materials is developed and clearly explained. Starting from an empiric mathematical model, the hysteresis and butterfly curves are obtained from COMSOL with a desirable level of agreement, at least for this early stage of development. Moreover, the model is embedded in the simulation of a reconfigurable resonator, opening the possibility of simulating this kind of MEMS devices.

Note about the impact of Covid-19 on the present work

The present work has been carried out during the infamous year of the COVID-19 pandemic. I started my research in the second half of February, and by mid March the lab was closed, together with the cleanroom. Unluckily, this fact had great impact on my Thesis work: in the original plans, I should have followed a highly experimental-oriented project named DARPA TUFEN. In this project framework, I would have mastered the usage of an industrial tool (EVATEC-clusterline) used to sputter AlN and doped AlN, optimizing the recipe in order to deposit high quality films. Moreover, I would have characterized them, and I would have fabricated structures such as suspended resonators to extract the mechanical, dielectric and piezoelectric coefficients, and study how those quantities and its ferroelectric behavior vary with the different Scandium concentration up to 40%.

Since everything was closed, I had to come up with new ideas. Chapter 2 of the present work is a really interesting analysis, and the topic is strictly bound to ScAlN and MEMS resonator technology. Concerning the third chapter, since one of the focus of the Thesis would have been ScAlN ferroelectricity, a tool to make simulative analysis of ferroelectric materials has been developed. Its presence will play a vital role in the second phase of the TUFEN project, in which innovative structures will be fabricated taking advantage of the possibilities of simulating them in advance.

Anyway, in the last month the lab reopened and I could also work on something practical, i.e. the characterization of ScAlN thin films which were in-house fabricated.

Acknowledgements

First of all, I would like to thank professor Matteo Rinaldi for having given me the opportunity of doing research in his group.

Then, many thanks are to Luca Colombo, the post-doc and friend who followed me during the months of my thesis, and helped me in growing as a researcher and as a person.

I also want to thank all the members of the SMART center at Northeastern University for their support.

Many thanks to my friends and colleagues Matteo Castellani, Fabio Bersano, Dario Cattozzo Mor, Matilde Pavese and Marco Abrate, with whom I shared the house during the Coronavirus pandemic, who were friends but in this period have become like a second family for me.

I really want to thank my family, my parents, my brother, my sister, for the incredible support they gave me in these past months and for the (even more incredible) support that they have given me in the past years, leading me to the moment I am living now. I am proud of this accomplishment, and I owe a great part to them, for which I am extremely grateful.

Last but not least, my gratitude goes to my Girlfriend, Farah, whose presence (even if telematic) has helped me going through the past troubled months. Even if a pandemic and half world distance are separating us, I never felt so close to you.

Many thanks to everyone has always supported me, directly or indirectly, the thesis is my work, but this accomplishment is shared by all of you.

Table of Contents

Note about the impact of Covid-19 on the present work	ii
List of Tables	VII
List of Figures	VIII
1 Introduction	1
1.1 Introduction	1
1.2 Physics of piezoelectricity	4
1.3 BVD Model	10
1.4 MEMS resonator ladder filters	12
1.5 Fundamentals of ferroelectricity	16
1.5.1 Introduction to ferroelectrics	16
1.5.2 Ferroelectric hysteresis	17
2 ScAlN Cross-sectional Lamé' Mode resonators	21
2.1 Introduction	21
2.2 Cross-sectional Lamé' Mode Resonator	25
2.3 Transducer design	29
2.4 Scandium doping of CLMRs	33
2.5 Simulation of CLMRs	34
2.5.1 2D simulations	34
2.5.2 3D simulations	44
2.6 AlN experimental plan	49
2.7 ScAlN experimental plan	52
2.7.1 Resonator design	52
2.7.2 Filter design	56
3 ScAlN ferroelectricity and FEM model of ferroelectrics	59
3.1 Ferroelectric ScAlN	59
3.2 Ferroelectric reconfigurable resonators	61
3.3 Experimental demonstration of ScAlN thin film ferroelectricity . . .	62

3.3.1	AixDBLI tool description	66
3.3.2	Measured samples and results	71
3.3.3	Leakage current compensation	75
3.4	FEA of ferroelectric materials	79
4	Conclusions and future work	97
5	Appendix A: Modeling of the static capacitance of CLMRs	99
6	Appendix B: Modeling of the parasitic resistance of CLMRs	104
	Bibliography	108

List of Tables

2.1	Density, Young's Modulus, Acoustic Impedance and Resistivity of the studied metals.	30
2.2	Comparison between the material constants of AlN and of ScAlN at 0% doping.	33
2.3	Values of IDT and BE thickness for the various electrode materials that allow to obtain the k_t^2 vs. h_{ScAlN}/λ_x curves with the highest EM coupling coefficients. For the LFE and BE case, when using Pt as electrode material, the metallization ratio α has been changed to 0.35 and 0.3, respectively, in order to shift a spurious mode due to the electrodes out of the frequency range of interest. This is the reason why the curves for the LFE CLMR with Pt electrodes of Figs. 2.12 and 2.14 are different.	38
2.4	Comparison of the best EM coupling coefficients for the TFE, LFE and BE CLMRs for 0% and 40% Sc doping.	41
2.5	List of k_t^2 , λ_x and f_s of each of the resonators of the bank of filters. S stands for series and p for parallel, i.e. the series and parallel resonator of the filter in Fig. 2.31.	56
3.1	Values of time, polarization, dielectric constant and piezoelectric coefficient used in the simulation of Fig. 3.31.	95

List of Figures

1.1	Drawing of a mass-damper-spring resonant structure, from [5]. . . .	2
1.2	Simplified structure of a quartz crystal with metal electrodes on top and bottom. In a), the crystal is in the original state without any mechanical load. In b) and c) the longitudinal and transverse piezoelectric effect, respectively, are shown. The centers of charge, namely C_{Q+} and C_{Q-} are also included. The figure is from [9]	5
1.3	Notation used for the piezoelectric constitutive equations with respect to the cartesian xyz three-dimensional coordinate system. The figure is from [9]	8
1.4	Butterworth-Van Dyke model of a piezoelectric MEMS resonator. .	10
1.5	Example of the admittance of a MEMS resonator with resonant and anti-resonant frequency.	11
1.6	Showcase of the scattering parameters of a first order ladder filter made by MEMS resonators. This specific filter has been included in the tapeout described in Section 2.7.2.	13
1.7	Schematic of a third-order ladder filter. A single L-network is highlighted.	14
1.8	Showcase of how the resonance of the series resonator and the anti-resonance of the shunt one should overlap in order to maximize the filter transmission at the pass-band center frequency	15
1.9	Showcase of the effect of the poling process. As it can be observed, before poling the ferroelectric domain are all oriented in random ways, leading to a net zero polarization. On the other hand, after the process, the domains have the polarization oriented in a specific direction, restoring the ferroelectric properties of the material. The figure is taken from [16]	18
1.10	Example of a P vs. E hysteresis curve in ferroelectric materials. The coercive fields, saturation and remnant polarization are shown. The insets show the switching state inside the ferroelectric. The figure is taken from [16]	19

1.11	a) Simplified version of a S vs. E curve (butterfly curve) for a ferroelectric material. The figure is taken from [16] and b) real experimental curve of a 500 nm thick ScAlN ferroelectric capacitor.	20
2.1	a) Simple view of an FBAR. As it can be observed, it is characterized by the presence of a piezoelectric thin film sandwiched between two metal electrodes, which act as terminals, b) commercial filter made up of seven FBARs, made by Broadcom, the biggest player in the MEMS resonator industry.	21
2.2	COMSOL® simulation of an FBAR device, showing a) the displacement and b) the stress distribution.	22
2.3	COMSOL® simulation of FBARs. They consist of a 10 μm thick AlN film and they have 500 nm of Al on top and on bottom (blue curve). In order to show the frequency tunability allowed by mass loading and trimming, keeping the thickness of the bottom electrode constant, 300 nm have been selectively (red curve) removed, increasing the resonant frequency and (yellow curve) added, decreasing it.	23
2.4	COMSOL® simulation of CMRs. In a) and b) the geometry is the same of FBARs, but the mode shape is different, having displacement in the lateral direction. a) shows the displacement, while b) the stress distribution. On the contrary, c) shows the structure presented in [18], in which a number N of CMRs is mechanically coupled in order to set the desired static capacitance C_0 .	24
2.5	COMSOL® simulation CLMRs showing a) the displacement and b) the stress field.	25
2.6	Investigated CLMR topologies: a) TFE b) LFE and c) BE CLMR. For each configuration, the terminal scheme is shown, together with the geometrical dimensions.	29
2.7	Von Mises Stress distribution inside a TFE CLMR with W electrodes as its thickness increases. It is clearly visible that the points with higher values tend to shift inside the metal, thus reducing the overall EM coupling. The figure has been obtained using Finite Element Analysis with COMSOL®.	31
2.8	Scaling of mechanical (C), piezoelectric (d, e) and dielectric (ϵ_r) properties of ScAlN with dopant concentration ranging from 0 to 0.4. The plots are based on the ab-initio equations derived in [22].	32
2.9	a) Variation of the equivalent stiffness constants for the CLM (C_{lat}, C_{thic}) with the Sc concentration, b) variation of the piezoelectric coupling constant of the CLM (K_{CLM}^2) with Sc-doping.	34

2.10	a) Resonant frequency of CLMRs in ScAlN normalized to the one of pure AlN, b) variation of the ratio of h_{ScAlN}/λ_x to excite a non-degenerate CLM with the Sc-doping level.	35
2.11	Comparison of the admittance Y_{11} vs. frequency f for two ScAlN TFE CLMR with W electrodes and 20% Sc concentration. The resonator horizontal acoustic wavelength λ_x is a) $8\mu m$ and b) $2\mu m$, which inserts the resonant frequencies in the Ultra High Frequency (UHF) and Super High Frequency (SHF) ranges, respectively. As it can be observed from the f_{res} in the insets, its value in b) is exactly four times the one in a). The k_t^2 is precisely the same.	36
2.12	k_t^2 vs. h_{ScAlN}/λ_x curves for the structures of TFE (a), LFE (b) and BE CLMR (c). The wavelength is $8\mu m$, the IDT thickness t_{IDT} is set to be $0.04\lambda_x$ and the one of the BE is $0.02\lambda_x$. The doping level is 0%. The presence of a single maximum means that only a specific ratio creates a non-degenerate CLM. In b) the Pt case has two peaks, but it is just the effect of a spurious mode close to the resonance induced by the electrodes that reduces the EM coupling for some ratios. As it can be observed, the value of the optimal ratio is different from 0.5.	37
2.13	k_t^2 vs. h_{ScAlN}/λ_x curves for the structures of TFE (a), LFE (b) and BE CLMR (c-d) for different IDT and BE thicknesses with W electrodes. The curves show the optimization step followed in the study of the best IDT and BE thickness for the various topologies. Figures a)-c) show the optimization of the IDTs, while in d), once found the best thickness of the electrodes for the BE CLMR, the BE has been swept to find the optimal value.	39
2.14	k_t^2 vs. h_{ScAlN}/λ_x curves for the structures of TFE (a), LFE (b) and BE CLMR (c) obtained using the optimized geometries. The values of t_{IDT} and of t_{BE} as function of λ_x are listed in Table 2.3.	40
2.15	k_t^2 vs. α curves for the TFE structure which has been chosen as a showcase.	40
2.16	k_t^2 vs. h_{ScAlN}/λ_x curves for the structures of TFE (a), LFE (b) and BE CLMR (c) for different Sc concentrations, namely 0, 20 and 40%. The electrode material is W. The curves clearly show the k_t^2 boost introduced by the Sc-doping. The increase in EM coupling is non-linear with the dopant concentration. The maximum of each curve is highlighted.	41
2.17	k_t^2 vs. h_{ScAlN}/λ_x curves for the structures of TFE (a), LFE (b) and BE CLMR (c) obtained using the optimized geometries. The doping level is 40%. The values of t_{IDT} and of t_{BE} as function of λ_x are the same as of the 0% case and are listed in Table 2.3.	42

2.18	Contour plots of k_t^2 vs. t_{top} and t_{bot} for h_{ScAlN}/λ_x equal to 0.2, 0.3 and 0.4, for a)-c) 0% Sc and d)-f) 40% Sc, showing the optimal geometrical dimensions.	43
2.19	Optimal t_{top} (a) and t_{bot} (b) values to maximize the k_t^2 . The black dots are the points taken from Fig. 2.18a-c, while the dashed line represents the quadratically fitted function.	44
2.20	Comparison of two k_t^2 vs. h_{ScAlN}/λ_x curves for two TFE CLMR with Al on top and Mo on bottom. The non-optimized case has $t_{top} = t_{bot} = 0.02\lambda_x$, while the optimized one has them following the fitting functions of Fig. 2.19a-b. The EM coupling increase is clearly visible.	45
2.21	3D COMSOL® model of a LFE CLMR, including the substrate and the PML.	46
2.22	Closer look at the 3D model of the LFE CLMR. The relevant dimensions are shown.	47
2.23	Comparison of the resonant curve for the CLM for the 2D and 3D model. In order to better compare the responses, the C_0 of the first has been reduced to match the latter, and the frequency has been slightly increased. As it can be observed, the k_t^2 is the same.	47
2.24	a) Behaviour of the motional resistance R_m (left) and of the k_t^2 (right) vs. the IDT length and b) showcase of the suppression of the spurious modes between f_s and f_p of the CLM due to the reduction of the inactive region length.	48
2.25	Expected curves of k_t^2 vs. h/λ_x for the CLMRs in AlN. In particular, in a) the TFE, in b) the LFE and in c) the BE CLMRs are shown.	50
2.26	S_{21} scattering parameter vs. frequency for the filters made of a) TFE CLMRs and b) BE CLMRs.	51
2.27	Showcase of the layers of which a TFE CLMR is composed. Each layer leads to the fabrication of a different lithographic mask.	53
2.28	Example of a TFE CLMR as it appears on Klayout.	54
2.29	Example of a first order TFE CLMR filter as it appears on Klayout.	54
2.30	a) curves of f_{res} and k_t^2 vs. h_{ScAlN}/λ_x expected to reproduce with the resonators included in the tape-out, b) curve of metallization ratio α vs. h_{ScAlN}/λ_x expected from the tape-out.	55
2.31	Schematic of a first order ladder filter made with resonators.	56
2.32	a) curves of f_{res} and k_t^2 vs. h_{ScAlN}/λ_x expected to reproduce with the resonators included in the tape-out, b) curve of metallization ratio α vs. h_{ScAlN}/λ_x expected from the tape-out.	57

3.1	$Sc_xAl_{1-x}N$ hysteresis curves for Sc contents of 0.27, 0.3, 0.32, 0.36, 0.4 and 0.43. The curve of PZT 52/48 is also shown for comparison. On the right, the atomic structure of the nitride is shown for the unpolarized and polarized material. The figure is from [15].	60
3.2	Simplified building block schematic of the RF front-end of a commercial wireless device (a) and of an ideal device in which all the filters have been replaced by reconfigurable ones (b). The picture is from [29]	62
3.3	a) Impedance curve of a ferroelectric resonator in the on stage (in red) and in the off stage (in black). The modified BVD (m-BVD) fitting is also present, b) S_{21} parameter of a switchable filter in the on (in blue) and off (in red) state. The figures are from [29].	63
3.4	Picture of the Evatec-Clusterline industrial sputtering tool. A schematic of the tool is depicted in the inset.	63
3.5	Atomic Force Microscope (AFM) images of the surface of ScAlN thin films for different nitrogen/argon ratio, both at the center and at the edge of the wafer. It can be observed that increasing the ratio, the presence of anomalous grains is considerably reduced. The best case is shown on the left, when the carrier gas is constituted only by nitrogen. This picture was taken from an IFCS presentation.	65
3.6	Transmission Electron Microscope (TEM) image of the material stack onto the silicon wafer showing, from bottom to top, the titanium adhesion layer, the Pt bottom electrode, the ScAlN film and then a protective layer used in the TEM imaging process. The insets show the ferroelectric film at the top and bottom interfaces. On the top one, a 5-6 nm thick native oxide is clearly visible.	66
3.7	Picture of the lithographic mask to define the ferroelectric capacitors on the ScAlN film, as it appears on the GDSII file. On the mask, the different pads are highlighted with the parameters that can be extracted by measuring them.	67
3.8	Picture of a the wafer with 250 nm of 30% ScAlN onto which four chips have been patterned.	68
3.9	Picture of the AixDBLI tool. On the right, the case, amplifier and system to suppress vibrations. The DBLI is on the left, together with the chuck, onto which wafers or single chips are placed to be tested.	69
3.10	Schematic of the optical setup of the AixDBLI characterization tool.	70
3.11	Showcase of a DHM measurement with, on the left, the input signal, and on the right the hysteresis curve. The picture is from the AixPlover manual.	71

3.12	Showcase of the laser placing and probing of a small circle 100 μm ferroelectric capacitor.	72
3.13	Showcase of a PM measurement with, on the left, the input signal, and on the right the output response. The picture is from the AixPlover manual.	73
3.14	Evolution of different parameters with the Sc concentration for the thicknesses taken into account in the present work. The studied parameters are surface Roughness, film thickness, rocking curve and stress.	74
3.15	Showcase of the data collected with the Aixacct tool. In particular, the blue curve shows the hysteresis with respect to the applied voltage, while the red one shows the butterfly curve.	75
3.16	On the left, there is the result of the PUND measurement on the 250 nm thick capacitors. In the insets on the right, the curves have been post processed with MatLab to isolate the switching from the non-switching part of the hysteresis curve.	76
3.17	On the left, the result of a PUND measurement on a 20 nm thick ferroelectric capacitor. In the figure, it can be observed that there is a probably unphysical phenomenon for which the negative relaxed remnant polarization is positive. On the right, the high asymmetry in the current for the positive and negative voltages is shown. . . .	76
3.18	Butterfly curves for the 500, 250 and 100 nm-thick capacitors. For each thickness, three different Sc concentrations are taken into account, namely 28, 31 and 36%.	77
3.19	Evolution of the d_{33} piezoelectric coefficient with the Sc content for different thicknesses, compared to the ab-initio values from [22]. . .	78
3.20	a) COMSOL 3D simulated geometry. The terminal and ground are shown. b) Input signal given to the terminal, with maximum and minimum value highlighted.	81
3.21	Hysteresis curve of P vs. V (a) and curve of P vs t (b) for the simulated structure of Fig. 3.20.	82
3.22	Hysteresis curve of P vs. V when the function described in Eq. (3.13) is employed, enabling the description of the polarization of an unpolarized sample.	83
3.23	Butterfly curve of u v. V (a) and curve of u vs. t (b) for the simulated structure of Fig. 3.20.	84
3.24	Comparison of the experimental curves of P vs. V (a) and u vs. V with the ones extracted with COMSOL.	85
3.25	Comparison of the experimental curves of P vs. V with the model made by the 2-points-fit described in [35].	88

3.26	Comparison of the experimental curves of P vs. V (a) and of u vs. V with the improved model made by the 4-points-fit described in [35].	90
3.27	Comparison of the extracted curve of ε_r vs. V from the experimental data with (a) the extracted curve from the old model and (b) the one obtained with the new one. The y-axis has been limited in order to be able to better capture the plots. The singularity is due to the smoothed edges of the hysteresis curves obtained with analytical models.	91
3.28	Showcase of the correct functionality of the model's extension to the stationary study case.	92
3.29	Curve of the piezoelectric coefficient d_{33} extracted by deriving the butterfly curve with respect to the electric field. The function is shown either in its natural form and in a smoothed form. The latter is the function that has been given to COMSOL.	93
3.30	Comparison of the admittance curves of 30% ScAlN FBARs. In a), a piezoelectric resonator has been simulated. In b), the same resonator but with the ferroelectric model with $t = 0$ is show. As it can be observed, the curves coincide.	94
3.31	Showcase of the admittance of the ferroelectric FBAR for different times.	95
5.1	Showcase of the static capacitance of an FBAR.	100
5.2	Showcase of the static capacitance of a LFE CLMR.	100
5.3	Showcase of the static capacitance of a TFE CLMR.	102
5.4	Showcase of the static capacitance of a BE CLMR.	102
5.5	Example of the schematic of the capacitance for a BE CLMR with four electrodes (three pairs).	103
6.1	Left: visualization of the routing elements that introduce electrical loading as they appear on the GDSII file. On the right, the complete lumped model of the resistance of a CLMR.	105
6.2	All the lumped model contributions to the parasitic resistance in a CLMR with the relative equations. The VIAs resistance is missing since it has been considered to the fixed value of 1Ω .	107

Chapter 1

Introduction

1.1 Introduction

In the past decades, Micro-Electromechanical Systems (MEMS) have proven to be a killer application in very different fields, including telecommunications, transportation, health care, internet of things (IoT) and automation in general. MEMS are defined as any device including moving parts or fluid in the μm - mm range, and which use a photolithography process for manufacturing [1]. This definition is very general, and Micro-Electromechanical (MEM) devices vary from relatively simple structures to extremely complex systems, in which the devices are monolithically integrated with microelectronics. The concept of continuous miniaturization of devices, which led to today's micro and nano-sized sensors and actuators, was introduced in 1959 by the physicist Richard Feynman in his famous speech "*There's Plenty of Room at the Bottom*". The speech had a great response, to the point that MEMS technology has radically changed our lifestyle in just half a century. The first techniques of surface micromachining, key step for the fabrication of MEMS, were developed in 1980s by U.C. Berkeley [2]. In 1990s, Analog Devices Inc. used a MEM accelerator in a commercial product, namely an accelerometer for automotive applications. From there, the MEMS market has been in a continuous growth [1], and is expected to keep growing in the following, with a forecast of Compound Annual Growth Rate (CAGR) of 6.34% until 2025 [3]. The expected growth lies in the always higher interest in IoT, smart consumer electronics, wearable devices. There is almost no field that has not taken advantage of the MEMS technology.

It is accurate to say that modern communication has been enabled by MEMS. The reason lies in the high performances, compact footprint at Radio Frequency (RF) and low cost associated to them. In particular, MEMS resonators have allowed the replacement of bigger quartz resonators and the simpler integration of the devices with electronic circuits. Moreover, filters made with MEMS resonators constitute

the RF front-end (FE) of most of the commercial devices in the communication sector, and the main player in the MEMS market is Broadcom, a company involved in RF, communication and resonators.

The first paper regarding an electromechanical resonating structure was published in 1967 [4]. In a vibrating mechanical system, there is a continuous conversion between kinetic and potential energy [5]. The transfer of energy is optimum (i.e. the losses are minimized) at specific frequencies, called the resonant frequencies of the system. At those frequencies, the system response peaks and its motion follows a particular unique pattern known as mode shape. The simplest resonator structure is constituted by a mass-spring system. Losses can be taken into account by a damper. The equation describing the motion of a uni-dimensional mass-damper-spring system shown in Fig. 1.1 is [5]:

$$M_{eff} \frac{d^2x}{dt^2} + \xi_{eff} \frac{dx}{dt} + K_{eff}x = F_{in} \quad (1.1)$$

where M_{eff} , ξ_{eff} and K_{eff} are the effective mass, losses and stiffness of the system, respectively, and F_{in} is the applied force. The transfer function of the system can be expressed as:

$$H(s) = \frac{X(s)}{F_{in}(s)} = \frac{1}{M_{eff}s^2 + \xi_{eff}s + K_{eff}} = \frac{1}{K_{eff}} \cdot \frac{\omega_0^2}{s^2 + \frac{\omega_0}{Q}s + \omega_0^2} \quad (1.2)$$

where s is the complex frequency, ω_0 the undamped (natural) frequency of the system and Q the quality factor. In particular, ω_0 is defined as:

$$\omega_0 = 2\pi f_0 = \sqrt{\frac{K_{eff}}{M_{eff}}} \quad (1.3)$$

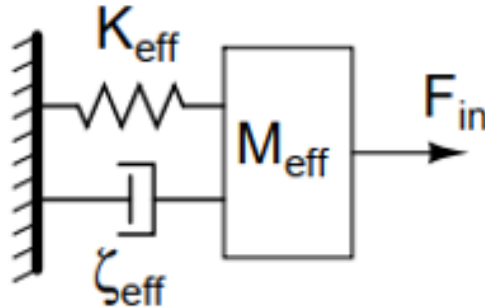


Figure 1.1: Drawing of a mass-damper-spring resonant structure, from [5].

while the quality factor is:

$$Q = 2\pi \frac{\text{Average energy stored}}{\text{Energy lost per cycle}} \quad (1.4)$$

Therefore, the Q is an effective measure of the loss mechanisms inside the device.

A MEMS resonator is a mechanically vibrating micro-structure brought in resonance by an electrical signal. The transduction mechanisms, i.e. the mechanisms through which the electrical signal can effectively put the system in resonance and sense it, are numerous. The most exploited ones are the capacitive, the thermal/piezoresistive and the piezoelectric one [5]. A brief description of each of them is given in the following. It has to be pointed out that the choice of the particular mechanism has a strong impact on the resonator performances, size, efficiency in energy conversion, ease of implementation and power consumption.

1. **Capacitive:** the exploited mechanism consists of the induced motion of a plate free to move when a voltage is applied between its electrodes. Conversely, the change in capacitance induced as a result of one of the plates movement, generates an electric current. Usually the resonant body constitutes one of the electrodes of the capacitive resonator. Thus, as a requirement, it has to be highly conductive. Doped Silicon and polysilicon have been the most natural choice [6]. The principle is very simple as the physical implementation. Thus, it is not surprising that the first micromachined resonator to be published was based on such a mechanism [4]. For the same reason, capacitive MEMS resonators are still today a very common choice.

Concerning the physics of the transduction, it is shown in [5] that the electromechanical coupling factor η , i.e. the ratio of the output mechanical force and the input electrical voltage, has the form:

$$\eta = V_p \frac{dC}{dx} \quad (1.5)$$

where V_p is the polarization voltage, C the capacitance and x the displacement of the resonating plate. The coupling factor tends to have really low values, showing that the transduction mechanism is not very efficient. Improvements can be done by reducing the gap between the electrodes or increasing the capacitive area. Nevertheless, it is difficult to scale those kind of resonators to frequencies higher than 100 MHz. An alternative can be found by filling the gap with a compliant dielectric, and high-Q capacitive resonators with this feature have been proven to work at frequencies beyond 1 GHz [7].

2. **Thermal/piezoresistive:** unlike the capacitive mechanism, which is able to actuate and sense, both the thermal and the piezoresistive can just do one

of them (one-way transduction), that's why they are combined together. In particular, the first is used in the actuation, and the latter in the sensing. The two mechanisms are characterized by their ease of implementation, which counterbalances the drawback of the one-way transduction. In fact, only a conductive material is needed: an electric current is made pass through it to either generate heat (thermal actuation) or measure resistance (piezoresistive sensing). Concerning the actuation part, the resonant vibration is excited once there is a matching between the thermal wave induced by the current and the mechanical resonance frequency. This kind of actuation is especially desired when a large force is needed to put in resonance structures immersed in fluid. The efficiency depends on the thermal time constant of the system. As regards the sensing, the piezoresistive effect consists of a change in resistivity in response to stress. Concerning the materials, single crystalline Silicon has incredibly sensing capabilities due to its high piezoresistive coefficients [8]. Piezoresistivity increases its effect when scaling, as opposed to other transduction mechanisms, that's why it's a common choice for very small scale resonators. Moreover, it is CMOS-compatible.

3. **Piezoelectric:** resonators based on piezoelectricity exploit the capability of converting mechanical stress in electric polarization (direct effect) or vice versa (indirect piezoelectricity). More detailed analysis on the physical effect is given in the next section. Piezoelectric resonators are the most popular, and the reasons are their self-generating nature (i.e. piezoelectricity is intrinsic in the material and does not require any external input) and large electromechanical couplings. The main complication in such a technology, is the difficulty in integration with electronics. In particular, single crystal materials such as Quartz and Lithium Niobate (LN) are not CMOS-compatible in their machining. AlN is one of the most promising piezoelectric materials and is nowadays the most commercially exploited, even though its resonator performances are much lower compared to the ones of the single crystal piezo-material. In particular, as well explained in Section 2.1, thin-Film Bulk Acoustic Resonators (FBARs) are the most common choice when it comes to build filters for wireless communications. Piezoelectric resonators are the focus of the present work.

1.2 Physics of piezoelectricity

Piezoelectricity was first discovered by the Curie brothers in 1880 on materials such as quartz, topaz and tourmaline, which showed the presence of electric charges when mechanical forces were applied to them (direct piezoelectric effect). The term piezoelectricity, in fact, comes from the Greek and means "electricity due to pressure".

The inverse effect was mathematically derived the next year by Lippmann, and confirmed experimentally by the Curie brothers immediately after. The piezoelectric effect provides a linear interaction between mechanical and electrical quantities, and finds a great number of applications, from process measurement technology to medicine, from energy harvesting to consumer electronics. All materials showing piezoelectricity are called piezoelectric. This effect is related to their lattice structure, i.e. to their particular crystal symmetry. There are 32 identified crystal point groups. Among them, 21 are noncentrosymmetric, necessary condition to show the piezoelectric effect. Only 20 of them are piezoelectric, and are often referred to piezoelectric point groups.

For the sake of clarity, let's consider the example of a Quartz (i.e. SiO_2) crystal described in [9] and shown in a simplified view in Fig. 1.2. The material, consisting of the chemical bonds between Silicon and Oxygen atoms, has the top and bottom surfaces metallized. In Fig. 1.2a, no force is acting on it, while in Fig. 1.2b-c, it is mechanically loaded with the force F in two different directions, which leads to different deformations. As can be observed, when no force is applied, the center

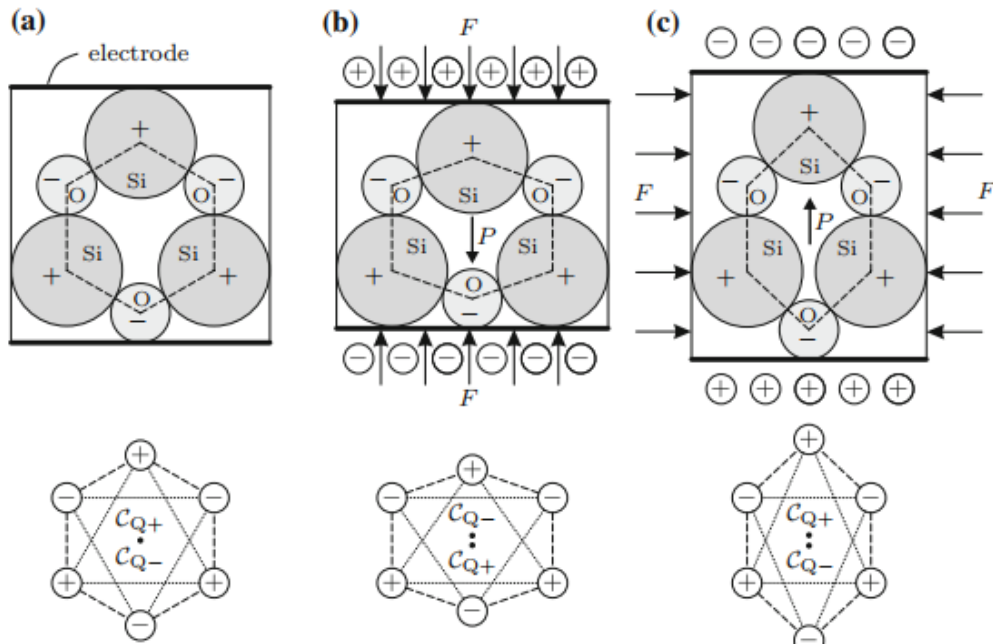


Figure 1.2: Simplified structure of a quartz crystal with metal electrodes on top and bottom. In a), the crystal is in the original state without any mechanical load. In b) and c) the longitudinal and transverse piezoelectric effect, respectively, are shown. The centers of charge, namely C_{Q+} and C_{Q-} are also included. The figure is from [9]

C_{Q-} of negative charges (the Oxygen ions) geometrically coincides with the center C_{Q+} of positive charges (the Silicon ions). This results in an electrically neutral material to the outside. On the other hand, when a mechanical force is applied, the centers of the charges are shifted, and do not coincide anymore, creating electric dipole moments from C_{Q-} to C_{Q+} . The dipole moment shows electric polarization P . To compensate it, i.e. an electric imbalance inside the material, charges are electrostatically induced on the electrodes. If there exist a short circuit between them, a current flow will occur. Conversely, for the inverse piezoelectric effect, the same process takes place but in the opposite direction: an electric voltage applied to the electrodes electrostatically induces charges on them, constituting an electric imbalance compensated by a dipole moment inside the material. As can be observed in Fig. 1.2b-c, in a general case the direction of the applied force generates a different dipole moment. In this case, in Fig. 1.2b the moment has the same direction of the applied field (longitudinal mode), while in Fig. 1.2c they are perpendicular (transverse mode).

Concerning the math behind piezoelectricity, as shown in [9], it can be derived from the first law of thermodynamics:

$$dU = dW + dQ = dW_{mech} + dW_{elec} + dQ \quad (1.6)$$

This formula states that a change of internal energy dU in a closed system is equal to the work dW done on the system and the heat energy dQ added to it. All those quantities are per unit of volume. For a piezoelectric material, the work can be divided into its electrical and mechanical components. Under the assumption of small changes, Eq. (1.6) can be rewritten as:

$$dU = E_m dD_m + T_{ij} dS_{ij} + \theta d\mathcal{S} \quad (1.7)$$

Where E_m and D_m are the electric field intensity and flux density, respectively, T_{ij} and S_{ij} are the mechanical stress and strain and θ and \mathcal{S} the temperature and entropy, respectively. Therefore, dU results from changes in D_m , S_{ij} and \mathcal{S} , which are called extensive variables. However, from a practical point of view, the description of the phenomenon is preferred as a function of the others, called intensive variables. Therefore, the Gibbs free energy G is introduced:

$$\mathcal{G} = U - E_m D_m - T_{ij} S_{ij} - \theta \mathcal{S} \quad (1.8)$$

When the condition of thermodynamic equilibrium is reached, the Gibbs free energy is minimized, meaning:

$$d\mathcal{G} = 0 = -D_m dE_m - S_{ij} dT_{ij} - \mathcal{S} d\theta \quad (1.9)$$

From it, the extensive state variables can be computed:

$$D_m = -\left(\frac{\partial \mathcal{G}}{\partial E_m}\right)_{T,\theta}, \quad S_{ij} = -\left(\frac{\partial \mathcal{G}}{\partial T_{ij}}\right)_{E,\theta}, \quad \mathcal{S} = -\left(\frac{\partial \mathcal{G}}{\partial \theta}\right)_{T,E} \quad (1.10)$$

In this way, the linearized state equations for the extensive variables can be written as:

$$dD_m = \left(\frac{\partial D_m}{\partial E_n}\right)_{T,\theta} dE_n + \left(\frac{\partial D_m}{\partial T_{kl}}\right)_{E,\theta} dT_{kl} + \left(\frac{\partial D_m}{\partial \theta}\right)_{T,E} d\theta \quad (1.11)$$

$$dS_{ij} = \left(\frac{\partial S_{ij}}{\partial E_n}\right)_{T,\theta} dE_n + \left(\frac{\partial S_{ij}}{\partial T_{kl}}\right)_{E,\theta} dT_{kl} + \left(\frac{\partial S_{ij}}{\partial \theta}\right)_{T,E} d\theta \quad (1.12)$$

$$d\mathcal{S} = \left(\frac{\partial \mathcal{S}}{\partial E_n}\right)_{T,\theta} dE_n + \left(\frac{\partial \mathcal{S}}{\partial T_{kl}}\right)_{E,\theta} dT_{kl} + \left(\frac{\partial \mathcal{S}}{\partial \theta}\right)_{T,E} d\theta \quad (1.13)$$

In the previous equations, each partial derivative represents a material parameter that characterizes a specific linearized coupling mechanism. The ones of interest are described later in this section. If temperature changes are neglected, i.e. isothermal change in state, the two material laws of piezoelectricity can be derived from Eqs. (1.11)-(1.12):

$$dD_m = \varepsilon_{mn}^T dE_n + d_{mkl} dT_{kl} \quad (1.14)$$

$$dS_{ij} = d_{ijn} dE_n + s_{ijkl}^E dT_{kl} \quad (1.15)$$

where the partial derivative have been substituted with the related material parameters: ε is the dielectric constant, d the piezoelectric strain coefficient and s the elastic compliance. The variables in the superscripts indicate that the parameter has been computed with it taken as constant. They are tensors, respectively of rank 2,3 and 4. Assuming that D_m , E_n , S_{ij} and T_{kl} are zero in the initial state, the equations can be rewritten as:

$$D_m = \varepsilon_{mn}^T E_n + d_{mkl} T_{kl} \quad (1.16)$$

$$S_{ij} = d_{ijn} E_n + s_{ijkl}^E T_{kl} \quad (1.17)$$

Eqs. (1.16) and (1.17) represent the so called d -form of the material law for linear piezoelectricity, also named strain-charge form. There exist another very used form called the e -form or stress-charge:

$$D_m = \varepsilon_{mn}^S E_n + e_{mkl} S_{kl} \quad (1.18)$$

$$T_{ij} = -e_{ijn}E_n + c_{ijkl}^E T_{kl} \quad (1.19)$$

where e is the piezoelectric stress coefficient and c the elastic stiffness constant. There exist other forms but they are not relevant for the studies of this work. Thanks to symmetries, the tensors equations can be transformed in matrices by making use of the Voigt Notation:

$$\mathbf{D} = [\varepsilon^T]\mathbf{E} + [\mathbf{d}]\mathbf{T}, \quad \mathbf{S} = [\mathbf{d}]^t\mathbf{E} + [\mathbf{s}^E]\mathbf{T} \quad (1.20)$$

$$\mathbf{D} = [\varepsilon^S]\mathbf{E} + [\mathbf{e}]\mathbf{S}, \quad \mathbf{T} = -[\mathbf{e}]^t\mathbf{E} + [\mathbf{c}^E]\mathbf{S} \quad (1.21)$$

The vectors \mathbf{D} and \mathbf{E} contain three components, while \mathbf{T} and \mathbf{S} have six independent ones. Therefore, the elastic, piezoelectric and dielectric matrices will be 6×6 , 3×6 and 3×3 , respectively, with 63 independent components in the most general case. The matrix equations for the d -form are shown, where the subscripts follow the notation of Fig. 1.3.

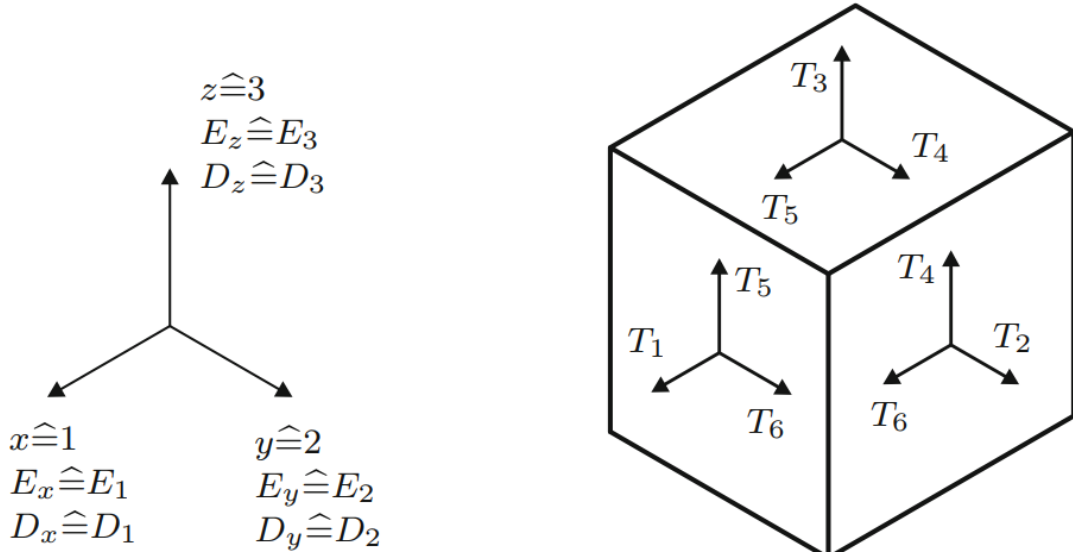


Figure 1.3: Notation used for the piezoelectric constitutive equations with respect to the cartesian xyz three-dimensional coordinate system. The figure is from [9]

$$\begin{bmatrix} D_1 \\ D_2 \\ D_3 \end{bmatrix} = \begin{bmatrix} \varepsilon_{11}^T & \varepsilon_{12}^T & \varepsilon_{13}^T \\ \varepsilon_{21}^T & \varepsilon_{22}^T & \varepsilon_{23}^T \\ \varepsilon_{31}^T & \varepsilon_{32}^T & \varepsilon_{33}^T \end{bmatrix} \begin{bmatrix} E_1 \\ E_2 \\ E_3 \end{bmatrix} + \begin{bmatrix} d_{11} & d_{12} & d_{13} & d_{14} & d_{15} & d_{16} \\ d_{21} & d_{22} & d_{23} & d_{24} & d_{25} & d_{26} \\ d_{31} & d_{32} & d_{33} & d_{34} & d_{35} & d_{36} \end{bmatrix} \begin{bmatrix} T_1 \\ T_2 \\ T_3 \\ T_4 \\ T_5 \\ T_6 \end{bmatrix} \quad (1.22)$$

$$\begin{bmatrix} S_1 \\ S_2 \\ S_3 \\ S_4 \\ S_5 \\ S_6 \end{bmatrix} = \begin{bmatrix} d_{11} & d_{21} & d_{31} \\ d_{12} & d_{22} & d_{32} \\ d_{13} & d_{23} & d_{33} \\ d_{14} & d_{24} & d_{34} \\ d_{15} & d_{25} & d_{35} \\ d_{16} & d_{26} & d_{36} \end{bmatrix} \begin{bmatrix} E_1 \\ E_2 \\ E_3 \end{bmatrix} + \begin{bmatrix} s_{11}^E & s_{12}^E & s_{13}^E & s_{14}^E & s_{15}^E & s_{16}^E \\ s_{21}^E & s_{22}^E & s_{23}^E & s_{24}^E & s_{25}^E & s_{26}^E \\ s_{31}^E & s_{32}^E & s_{33}^E & s_{34}^E & s_{35}^E & s_{36}^E \\ s_{41}^E & s_{42}^E & s_{43}^E & s_{44}^E & s_{45}^E & s_{46}^E \\ s_{51}^E & s_{52}^E & s_{53}^E & s_{54}^E & s_{55}^E & s_{56}^E \\ s_{61}^E & s_{62}^E & s_{63}^E & s_{64}^E & s_{65}^E & s_{66}^E \end{bmatrix} \begin{bmatrix} T_1 \\ T_2 \\ T_3 \\ T_4 \\ T_5 \\ T_6 \end{bmatrix} \quad (1.23)$$

Actually, thanks to symmetries of the crystals, the number of independent components is considerably reduced. For example, for the AlN and ScAlN which are treated in Chapter 2, they become:

$$\begin{bmatrix} D_1 \\ D_2 \\ D_3 \end{bmatrix} = \begin{bmatrix} \varepsilon_{11}^T & 0 & 0 \\ 0 & \varepsilon_{11}^T & 0 \\ 0 & 0 & \varepsilon_{33}^T \end{bmatrix} \begin{bmatrix} E_1 \\ E_2 \\ E_3 \end{bmatrix} + \begin{bmatrix} 0 & 0 & 0 & 0 & d_{15} & 0 \\ 0 & 0 & 0 & d_{15} & 0 & 0 \\ d_{31} & d_{31} & d_{33} & 0 & 0 & 0 \end{bmatrix} \begin{bmatrix} T_1 \\ T_2 \\ T_3 \\ T_4 \\ T_5 \\ T_6 \end{bmatrix} \quad (1.24)$$

$$\begin{bmatrix} S_1 \\ S_2 \\ S_3 \\ S_4 \\ S_5 \\ S_6 \end{bmatrix} = \begin{bmatrix} 0 & 0 & d_{31} \\ 0 & 0 & d_{31} \\ 0 & 0 & d_{33} \\ 0 & d_{15} & 0 \\ d_{15} & 0 & 0 \\ 0 & 0 & 0 \end{bmatrix} \begin{bmatrix} E_1 \\ E_2 \\ E_3 \end{bmatrix} + \begin{bmatrix} s_{11}^E & s_{12}^E & s_{13}^E & 0 & 0 & 0 \\ s_{12}^E & s_{11}^E & s_{13}^E & 0 & 0 & 0 \\ s_{13}^E & s_{13}^E & s_{33}^E & 0^E & 0 & 0 \\ 0 & 0 & 0 & s_{44}^E & 0 & 0 \\ 0 & 0 & 0 & 0 & s_{44}^E & 0 \\ 0^E & 0 & 0 & 0 & 0 & \frac{s_{11}^E + s_{22}^E}{2} \end{bmatrix} \begin{bmatrix} T_1 \\ T_2 \\ T_3 \\ T_4 \\ T_5 \\ T_6 \end{bmatrix} \quad (1.25)$$

As previously stated, piezoelectricity is a phenomenon that relates the electrical and mechanical domains. Nevertheless, in a piezo-material, not all the mechanical energy is converted to electrical and vice versa. The parameter k^2 , i.e. the electromechanical coupling, quantifies the efficiency of conversion. In particular, it is defined as:

$$k^2 = \frac{\text{mechanical energy converted into electrical energy}}{\text{mechanical input energy}} \quad (1.26)$$

$$k^2 = \frac{\text{electrical energy converted into mechanical energy}}{\text{electrical input energy}} \quad (1.27)$$

As demonstrated in [9], the electromechanical couplings the same for both the conversion directions, and is always lower than 1.

1.3 BVD Model

As seen in Section 1.1, the equations describing a resonator are not trivial. Moreover, MEMS resonators require laws relating the electrical and mechanical domain, resulting in very complicated transcendental equations. The Butterworth Van-Dike (BVD) model [10] provides a simple description of the piezoelectric device, modeling it as an electrical circuit. The schematic is shown in Fig. 1.4 for a one-port resonator. As it can be observed, it consists of two branches in parallel, namely the motional and the static one. The static branch consists of a capacitance, named the static capacitance of the system, which is the real electric capacitance between the electrodes of the resonator. Its value has to be tuned in order to match a specific value, typically 50Ω , as seen in Appendix A. Concerning the mechanical behaviour, it is represented by the motional branch, in which the inductor L_m represents the mass, the capacitor C_m the compliance of the structure and the resistor R_m the losses. The admittance of such a circuit is:

$$Y_{BVD} = j\omega C_0 + \frac{1}{R_m + j\omega L_m + 1/C_m} \quad (1.28)$$

and can be rewritten as:

$$Y_{BVD} = 2\pi j f C_0 \frac{1 - (f/f_a)^2 + j(f/f_a)Q_a^{-1}}{1 - (f/f_{res})^2 + j(f/f_{res})Q_r^{-1}} \quad (1.29)$$

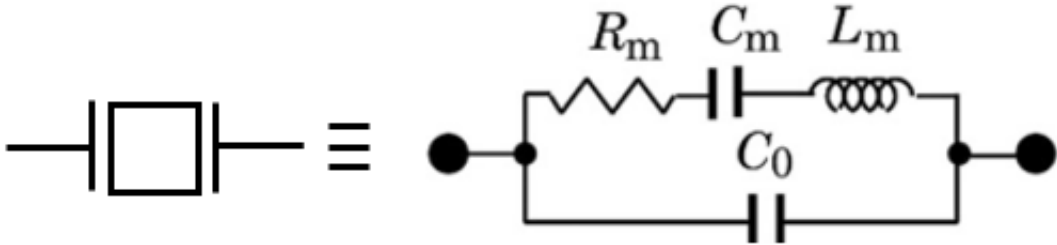


Figure 1.4: Butterworth-Van Dyke model of a piezoelectric MEMS resonator.

where j is the imaginary unit, f the frequency, f_{res} , Q_r and f_a , Q_a the frequency and the quality factor at resonance and anti-resonance, respectively. From Eqs. (1.28)-(1.29), the following quantities can be obtained [11]:

$$f_{res} = \frac{1}{2\pi\sqrt{L_m C_m}} \quad (1.30)$$

$$f_a = \frac{1}{2\pi\sqrt{L_m(C_m^{-1} + C_0^{-1})^{-1}}} \quad (1.31)$$

$$Q_r = \frac{2\pi f_{res} L_m}{R_m} \quad (1.32)$$

$$Q_a = \frac{2\pi f_a L_m}{R_m} \quad (1.33)$$

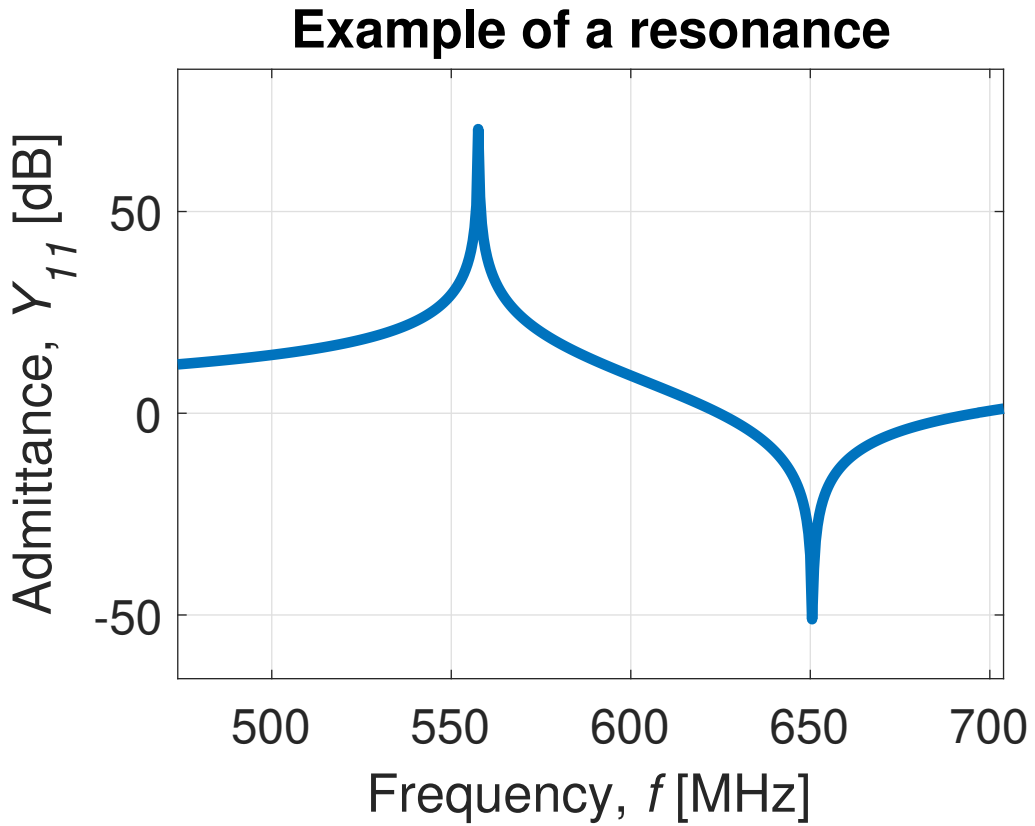


Figure 1.5: Example of the admittance of a MEMS resonator with resonant and anti-resonant frequency.

More often, anyway, the circuit parameters are not known, and are extracted from a simulated or experimental resonance. A typical one is shown in Fig. 1.5. As it can be observed, the admittance reaches its maximum value at resonance and its minimum at anti-resonance. The admittance value does not diverge at resonance thanks to the presence of the motional resistance. Given the knowledge of the static capacitance, of the resonant frequency and of the quality factor at resonance, the values of the circuit elements are found from:

$$R_m = \frac{\pi^2}{8} \frac{1}{k_t^2 Q_r C_0 \omega_{res}} \quad (1.34)$$

$$L_m = \frac{\pi^2}{8} \frac{1}{k_t^2 C_0 \omega_{res}^2} \quad (1.35)$$

$$C_m = \frac{8}{\pi^2} k_t^2 C_0 \quad (1.36)$$

Finally, the quantity k_t^2 , namely the electromechanical coupling defined in Section 1.2, can be directly extracted from the admittance curve [12]:

$$k_t^2 = \frac{\pi^8}{8} \frac{f_{res}^2 - f_a^2}{f_{res}^2} \quad (1.37)$$

1.4 MEMS resonator ladder filters

As stated in Section 1.1, MEMS resonators are building blocks for RF filters. In this section, a brief introduction on a specific topology, namely the ladder filter, is given. This filter topology allows to fabricate band-pass filters, i.e. filters that attenuate a signal unless its frequency is included in the pass-band. In order to better understand the filter characteristics, the Scattering parameters are introduced.

Let's consider the case of a N-port system. For it, a $N \times N$ scattering matrix can be defined. In particular, its elements, named scattering parameters, are defined as function of incident and reflected power waves, a_i and b_i , respectively, for the i -th port. Assuming that the reference impedance is the same for each port, these quantities are given by the following equations [13]:

$$a_i = \frac{1}{2} \frac{V_i + Z_0 I_i}{\sqrt{\text{Re}(Z_0)}} \quad (1.38)$$

$$b_i = \frac{1}{2} \frac{V_i - Z_0^* I_i}{\sqrt{\text{Re}(Z_0)}} \quad (1.39)$$

where $Re(Z_0)$ denotes its real part, the superscript $*$ the complex conjugate. V_i and I_i are complex amplitudes of voltage and current at the i -th port, respectively. These quantities are related by:

$$\mathbf{b} = \mathbf{S} \cdot \mathbf{a} \quad (1.40)$$

In a 2-port system, as in the case of a MEMS ladder filter, the explicit matrix equation becomes:

$$\begin{bmatrix} b_1 \\ b_2 \end{bmatrix} = \begin{bmatrix} S_{11} & S_{12} \\ S_{21} & S_{22} \end{bmatrix} \begin{bmatrix} a_1 \\ a_2 \end{bmatrix} \quad (1.41)$$

Fig. 1.6a-d shows the four scattering parameters of a first order ladder filter which was included in the experimental tapeout described in Section 2.7.2. The

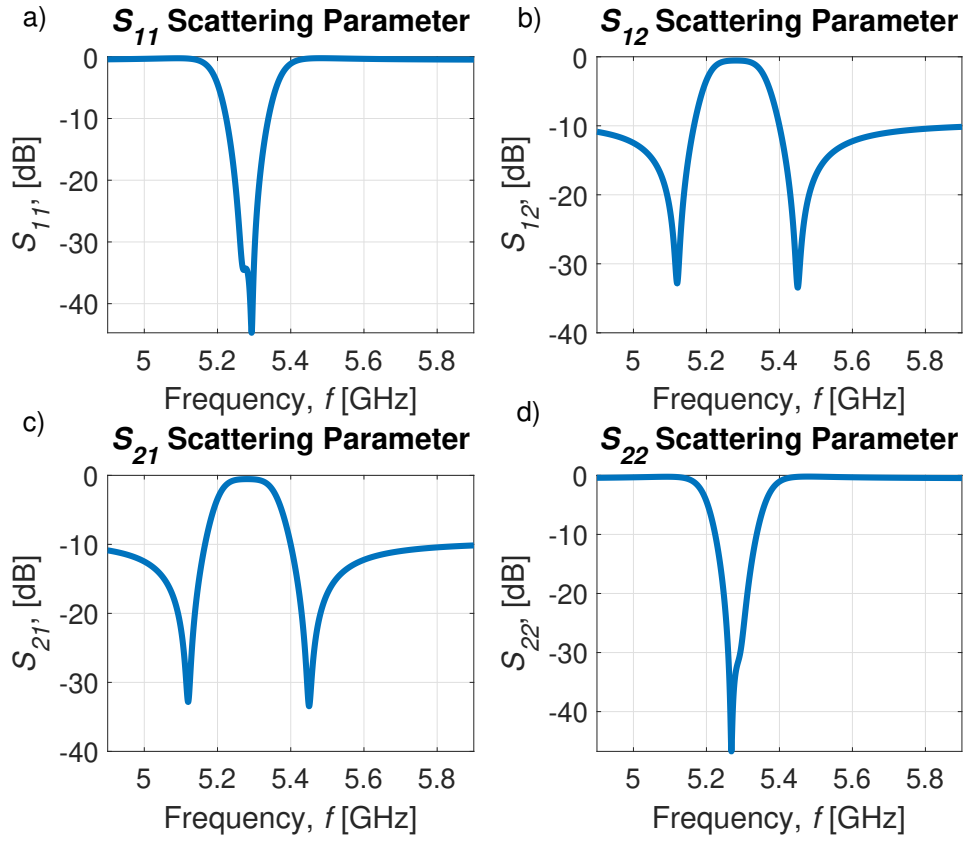


Figure 1.6: Showcase of the scattering parameters of a first order ladder filter made by MEMS resonators. This specific filter has been included in the tapeout described in Section 2.7.2.

most interesting of the parameters is S_{21} , from which the pass-band can be clearly observed. In this specific case, S_{12} and S_{21} are equal, and for this reason the network is called reciprocal.

Concerning the structure of a resonator ladder filter, it is shown in Fig. 1.7. It is constituted by the cascade of N resonator L-networks. The single L-network is highlighted in Fig. 1.7. The number N defines the order of the filter. All the series resonators have the same resonant and anti-resonant frequency, same thing for the parallel ones. The center frequency of the filter is set by the resonance of the series blocks. At that frequency, the series circuit branch has the lowest impedance, so the transmission is maximized. In order not to lose power in the parallel branch, it is important that at that frequency the parallel resonators have the maximum impedance. That's why the anti-resonant frequency of the shunt resonators have to match the one of the series ones as in Fig 1.8. Concerning the notches in Fig. 1.6c:

1. The first notch is originated by the resonance of the shunt resonators: at that frequency, the impedance of the shunt branches is minimized and all the signal is sent to ground.
2. The second notch comes from the anti-resonance of the series resonators, at which the impedance of the series branch is maximized and therefore the signal that passes from the first to the second port is minimized.

Let's define some important parameters of the filters, namely the out-of-band rejection S_{21rej} , the insertion loss IL and the fractional bandwidth FBW. The first one consist in the value of S_{21} outside the pass-band, the smaller, the better. This quantity is controlled by the capacitive voltage divider nature of the circuit and is

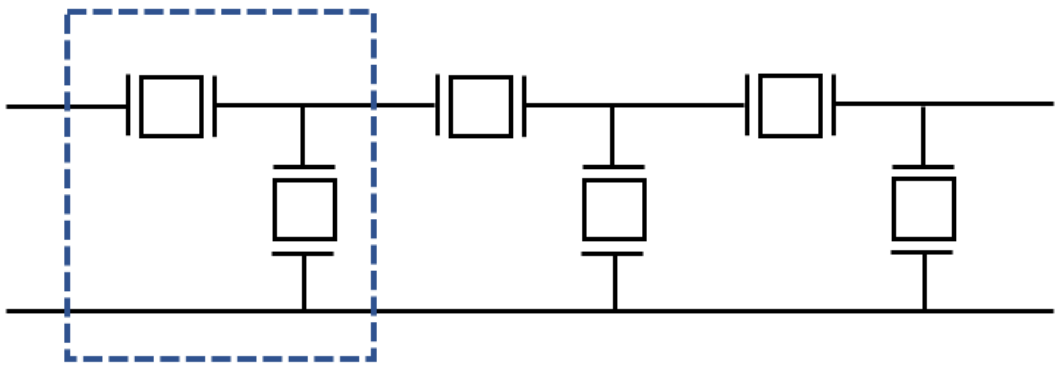


Figure 1.7: Schematic of a third-order ladder filter. A single L-network is highlighted.

in general expressed in dB. In particular, the equation describing it is [14]:

$$S_{21rej} \approx \frac{1}{\left(1 + \frac{C_{02}}{C_{01}}\right)^N} \quad (1.42)$$

where N is the number of L-networks and C_{01} and C_{02} are the static capacitances of the series and parallel resonators, respectively. Therefore, in order to increase the out-of-band rejection, the filter order or the capacitance ratio between the series and shunt resonators should be increased.

The second parameter is the IL, which is a measure of how much a signal in the pass-band passing through the filter is degraded and is also generally expressed in

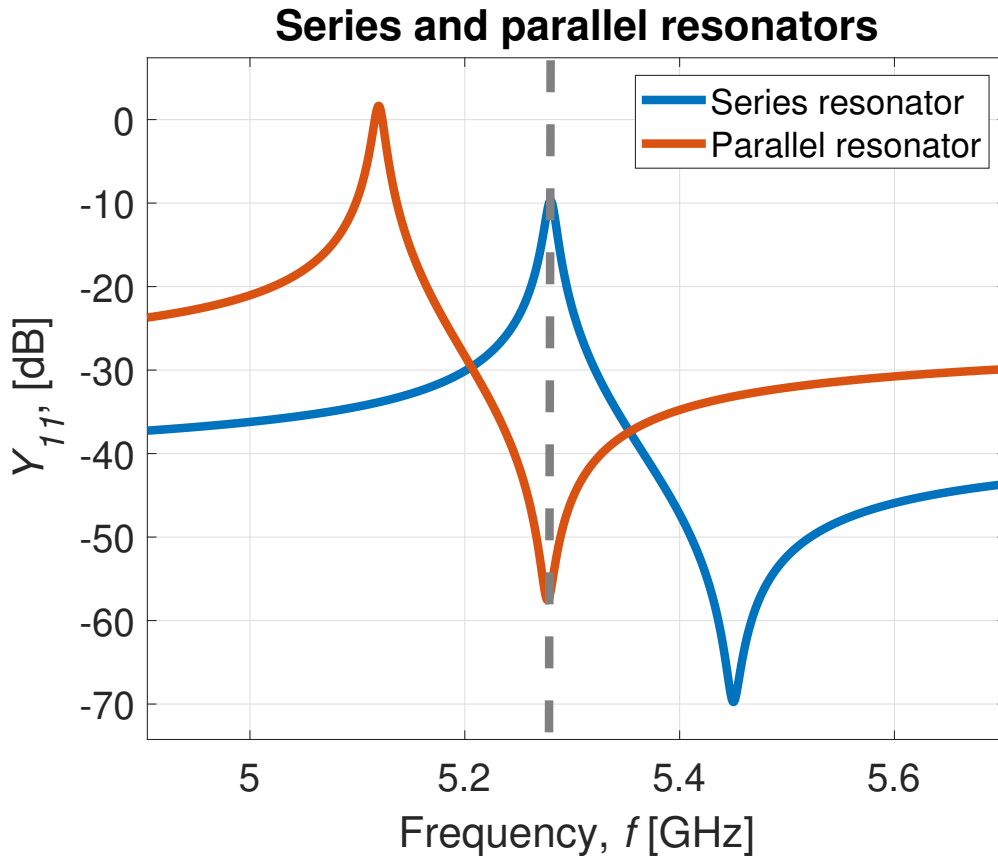


Figure 1.8: Showcase of how the resonance of the series resonator and the anti-resonance of the shunt one should overlap in order to maximize the filter transmission at the pass-band center frequency

dB. Its equation is [14]:

$$IL \approx 1 - \frac{N}{4\pi f_C C_{01} Z_0 k_t^2 Q_r} \quad (1.43)$$

where f_C is the filter center frequency. As it can be straightforwardly observed, the IL increases with an increasing number of series resonators. This makes sense, since the signal has to pass through more filter building blocks, meaning more signal dissipation through the motional resistances. Moreover, it is inversely proportional to the resonators quality factor.

Finally, the FBW is related to the electromechanical coupling of the resonators:

$$FBW = \frac{f_{a1} - f_{res2}}{f_C} \approx \frac{8}{\pi^2} k_t^2 \quad (1.44)$$

1.5 Fundamentals of ferroelectricity

1.5.1 Introduction to ferroelectrics

It was very recently demonstrated that Sc-doped AlN (ScAlN), the material focus of the present work, is ferroelectric [15]. A detailed discussion on its properties will be given in a later chapter, while in this section, the fundamentals of ferroelectricity are given.

As mentioned in Section 1.2, there are 21 non-centrosymmetric crystal point groups, 20 of them are piezoelectric. Among them, 10 point groups are characterized by a unique polar axis, which allows them to possess a spontaneous polarization P_s in the absence of an externally applied electric field. These material are called ferroelectrics. Since the polarization is a vector, and therefore possesses an orientation, ferroelectric materials have at least two equilibrium orientations for the spontaneous polarization. The material can then switch between them by the application of an electric field. These polarization states are stable and the name ferroelectricity was given in analogy to the ferromagnetism.

The presence of a ferroelectric behaviour is, in general, dependent on the temperature. In particular, this materials undergo a phase transition from a low-temperature, low-symmetric phase to a high-temperature, higher symmetric phase. The transition temperature is called Curie Temperature (T_c), and separates the ferroelectric from the non-ferroelectric (or paraelectric) phase. Above the Curie Temperature, the dielectric constant of such materials decreases according to the Curie-Weiss law [16]:

$$\varepsilon = \varepsilon_0 + \frac{C}{T - T_0} \quad (1.45)$$

where C is the Curie constant and T_0 the Curie-Weiss temperature. Some ferroelectrics undergo more than one phase transitions. An example is barium titanate.

In ferroelectric materials, especially the polycrystalline ones, the spontaneous polarization is not aligned in a uniform way along the whole crystal. In fact, there exist regions in which the net polarization vector points to a specific direction, which is not necessarily the same of the neighbouring regions. Between two domains, there is the domain wall. Inside the ferroelectric, the spontaneous polarization leads to the generation of a surface charge, and thus an imbalance inside the material. This imbalance produces an electric field, called the depolarizing field E_d , which is oriented in the opposite direction of P_s . The reason for the creation of the domains relies in the minimization of the electrostatic energy of depolarizing fields. In fact, when E_d is strong (i.e. of the order of MV/cm²), the single domain state is energetically unfavourable. In this case the energy is minimized when the polarization of the neighbouring domains is oppositely oriented. The splitting into ferroelectric domains may also be caused by a mechanical stress.

In real materials, since there exist a complex set of mechanical and electric boundary conditions at each grain, there is the splitting into many domains. Due to this effect, the net polarization across the material may be null, leading to the loss of piezoelectric and ferroelectric properties. In order to reorient domains and have a non-zero polarization, the material is poled. The poling process consists of applying strong electric fields, usually at high temperatures. The effect of poling is shown in Fig. 1.9. A single crystal that contains only one domain is said to be in a monodomain state. This particular state can also be achieved by poling.

1.5.2 Ferroelectric hysteresis

As previously introduced, a ferroelectric material possesses two stable states of polarization. Contrarily to piezoelectricity, which is modeled as a linear phenomenon, ferroelectricity is highly non-linear, and shows hysteresis. The two hysteretic behaviour regard the P vs. E and the S vs E curves, where S is the strain. This behaviour originates from the material domain-wall switching.

Let's start with the description of the Polarization vs. Electric field characteristic, which is shown in Fig 1.10.

Starting from a non-poled ferroelectric, for small AC electric fields, the polarization increases linearly with E following the piezoelectric equations, as it can be seen in the figure from point A to B. In this case the field is not strong enough to switch the ferroelectric domains. With increasing field, the domains start switching and rapidly increasing the polarization. As it can be observed, the behavior is not linear anymore, and the piezoelectric equations are no longer valid. This corresponds to the curve from B to C. When all the domains have switched, the polarization

saturates and the curve becomes linear again (segment CD). The intercept between the linear extrapolation of CD and the y-axis is called saturation polarization P_S . When the field starts decreasing, some domains switch again, but now, at zero field, the polarization is different from zero. Its value is called remnant polarization P_r . In order to bring the polarization to zero the field has to be furtherly decreased up to the coercive field $-E_c$ (EF on the curve). Then, the same thing as before happens for the opposite switching state. In an ideal curve, the positive and negative coercive fields and polarizations are the same, i.e. $|E_c| = |-E_c|$ and $|P_r| = |-P_r|$, respectively. This is not the case for real materials, for which those values are affected by several factors such as the thickness, the aging, the presence of mechanical stresses.

Concerning the Stress vs. Electric field curve, a simplified version is shown in Fig. 1.11a. As it can be observed, at zero electric field the strain (or the displacement) is zero. Then, the field is applied in the direction of the spontaneous polarization, and the material deforms linearly according to the piezoelectric equations (AB and BC) up to the maximum point of deformation (C). Then, the field starts decreasing but still being parallel to the spontaneous polarization. The response keeps being linear going from C to A, where the strain becomes null. Then the field is reversed, and has direction opposed to the polarization. For small values of E the response is a linear contraction of the material. Nevertheless, when the field is high enough, it starts switching the ferroelectric domains (D). When

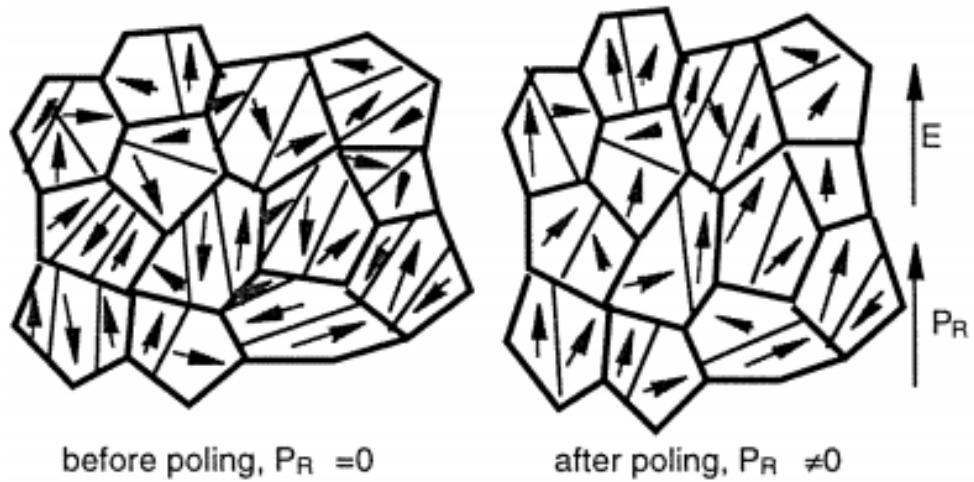


Figure 1.9: Showcase of the effect of the poling process. As it can be observed, before poling the ferroelectric domain are all oriented in random ways, leading to a net zero polarization. On the other hand, after the process, the domains have the polarization oriented in a specific direction, restoring the ferroelectric properties of the material. The figure is taken from [16]

the polarization reversal is completed, the latter returns parallel to the field and the strain abruptly changes polarity (E) and goes up to the point of maximum deformation (F). Then the field starts increasing and the same behavior of C-F is repeated in F-C. As can be observed, contrarily to the Polarization characteristics, there is no spontaneous strain in an ideal case. Nonetheless, in a real case such as the one of Fig. 1.11b, small deviation of the point A from zero strain origin due to fields inside the ferroelectric.

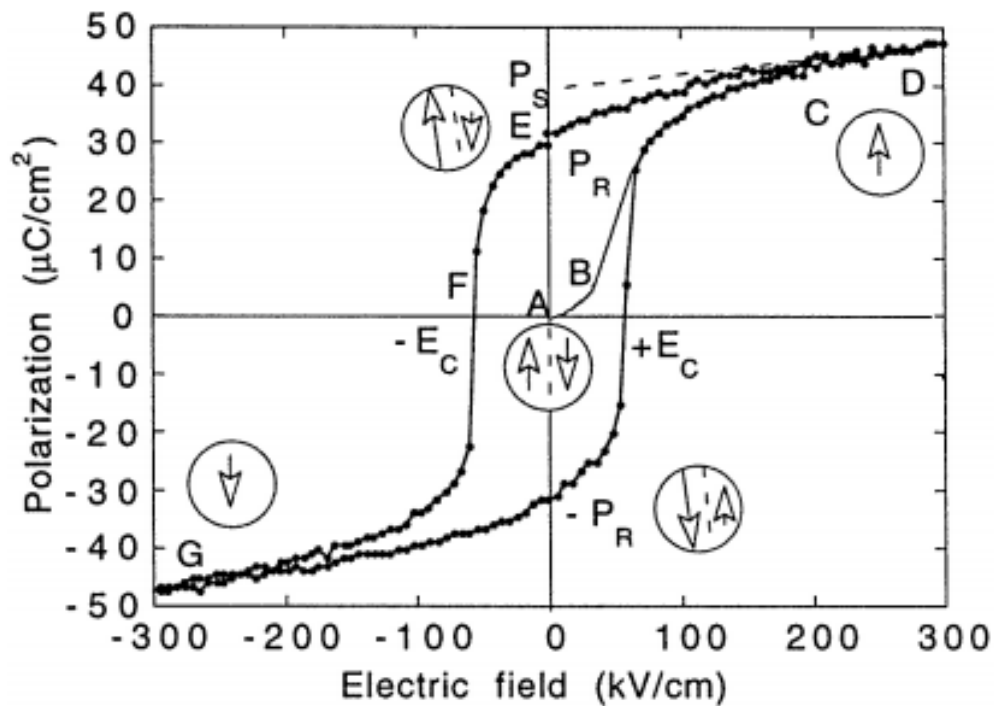


Figure 1.10: Example of a P vs. E hysteresis curve in ferroelectric materials. The coercive fields, saturation and remnant polarization are shown. The insets show the switching state inside the ferroelectric. The figure is taken from [16]

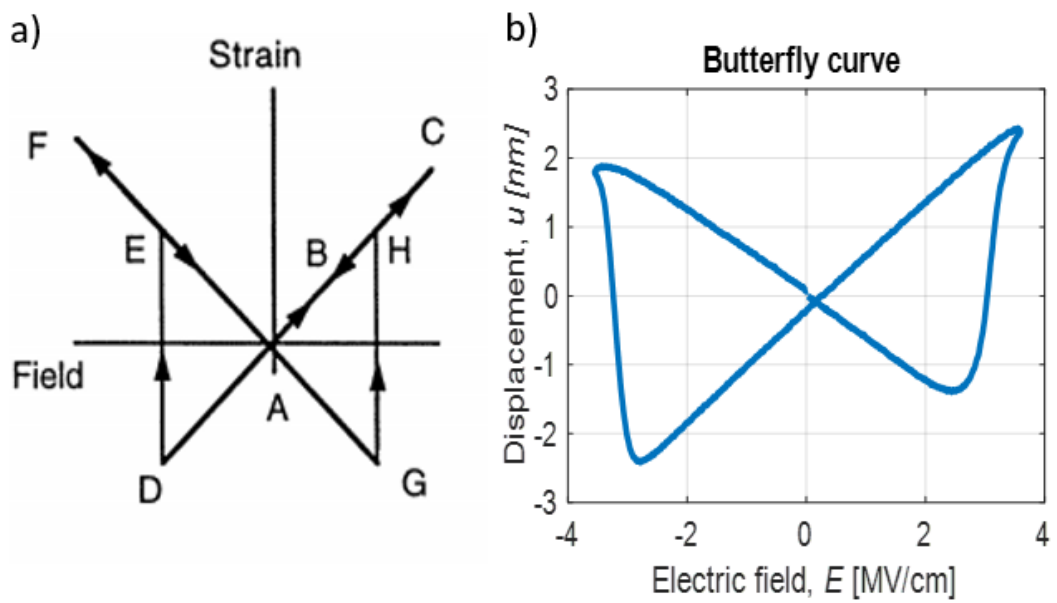


Figure 1.11: a) Simplified version of a S vs. E curve (butterfly curve) for a ferroelectric material. The figure is taken from [16] and b) real experimental curve of a 500 nm thick ScAlN ferroelectric capacitor.

Chapter 2

ScAlN Cross-sectional Lame' Mode resonators

2.1 Introduction

Nowadays, the MEMS resonator market is dominated by AlN FBARs (Fig. 2.1). The advantage of this kind of resonators relies in their high quality factor Q and electromechanical coupling coefficient k_t^2 . As shown in Fig. 2.1a, an FBAR consists of a sputtered piezoelectric layer sandwiched between a top and a bottom electrode [17]. The mode of vibration is the Lamb Wave S_1 mode, characterized by vibration along the vertical dimension which takes advantage from the e_{33} piezoelectric coefficient, whose value for AlN is 1.55 C/m^2 . The mode shape in Fig. 2.2a shows a minimum of the displacement at the center of the thickness and two maxima at the

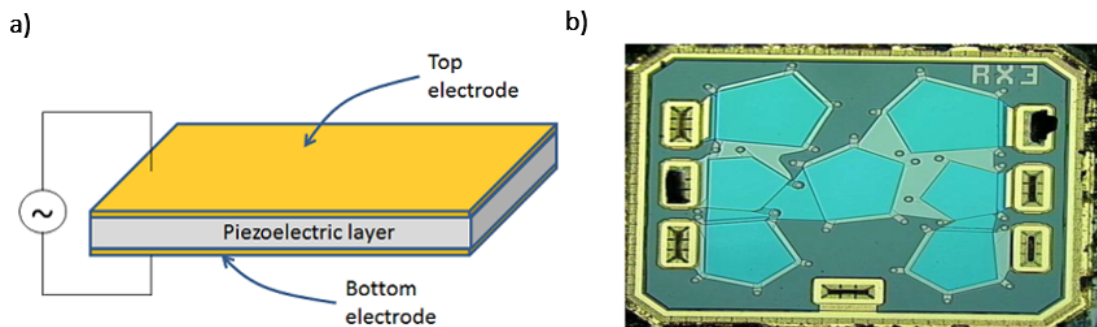


Figure 2.1: a) Simple view of an FBAR. As it can be observed, it is characterized by the presence of a piezoelectric thin film sandwiched between two metal electrodes, which act as terminals, b) commercial filter made up of seven FBARs, made by Broadcom, the biggest player in the MEMS resonator industry.

extreme points. Fig. 2.2b shows the stress distribution. It can be noticed that the points of maximum displacement correspond to the ones of minimum stress and vice versa. Although FBARs show great performances, they lack in easy tuning of the resonant frequency on the wafer. In fact, the resonant frequency of such resonators is:

$$f_{res} = \frac{1}{2h} \cdot \sqrt{\frac{C_{33}}{\rho}} \quad (2.1)$$

where h is the piezoelectric thickness, C_{33} is the involved stiffness coefficient, ρ is the density of the film. So, once the film thickness has been chosen, the resonant frequency is set. But, as shown in Sect. 1.4, since the filters made with microacoustic

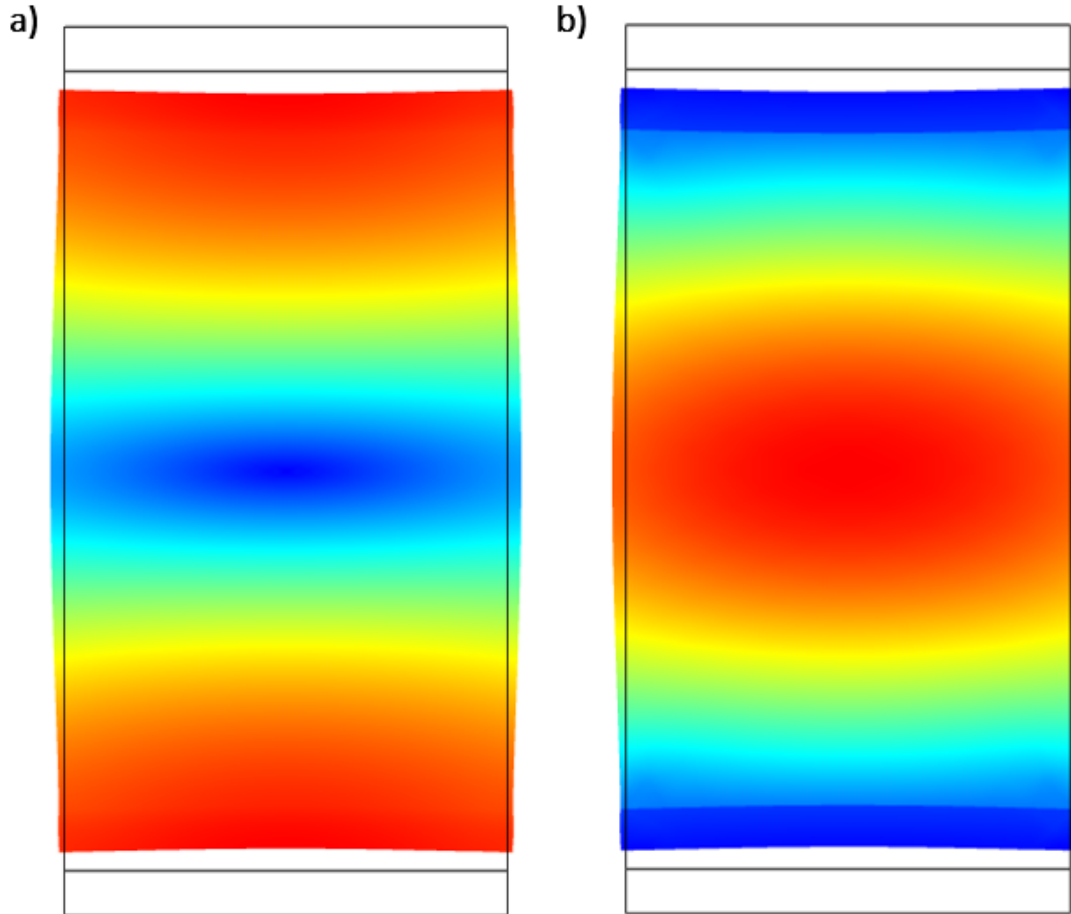


Figure 2.2: COMSOL® simulation of an FBAR device, showing a) the displacement and b) the stress distribution.

resonators need their building blocks to have different resonances, a way to tune them must be found. For FBARs it is not that trivial, and the fabrication process has to be complicated by introducing mass loading or trimming. The first is accomplished by depositing more metal, the latter by removing some. Fig. 2.3 shows how the resonance of an FBAR is modified by those effects. In particular, an FBAR with 500 nm thick electrodes is simulated using a 2D COMSOL® model. Then, 300 nm are removed or added in order to reproduce the trimming and mass loading conditions, respectively. The electrode material is Al, which is a 'light' metal. In the case of a heavy metal, the frequency shift would be much higher. Concerning the fabrication process of commercial FBARs, it has reached a complexity level such that it consists of more than twenty lithographic masks, with mass loading and trimming with a resolution of Å.

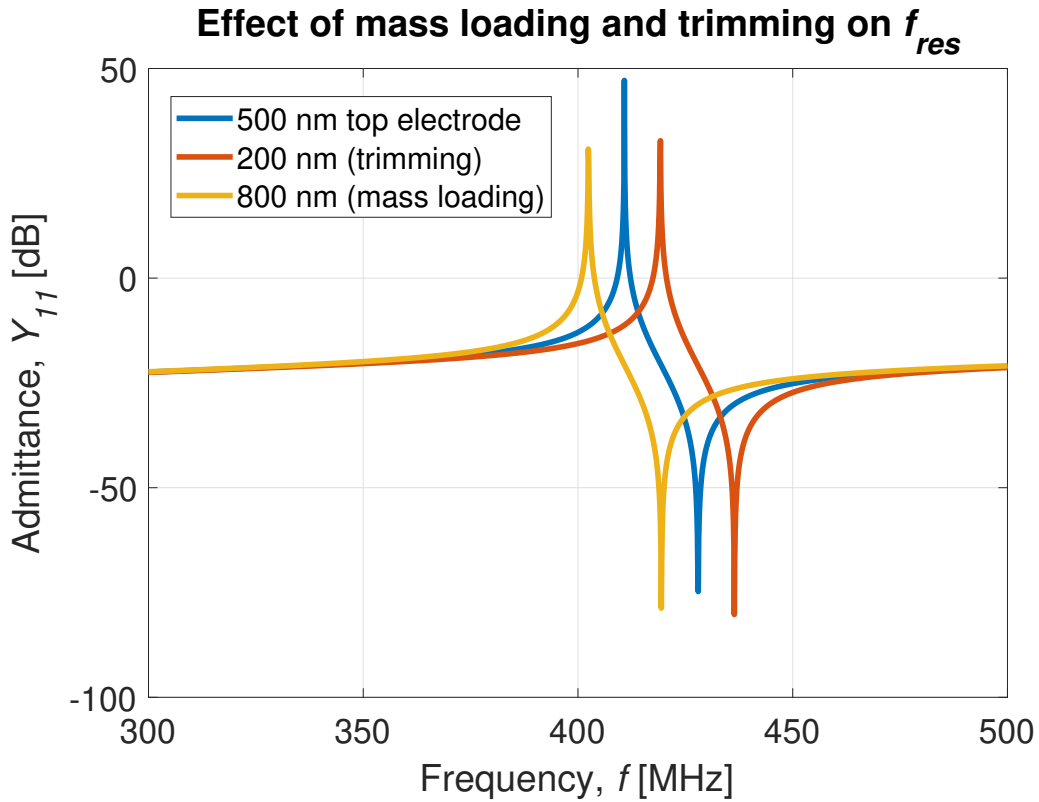


Figure 2.3: COMSOL® simulation of FBARs. They consist of a 10 μm thick AlN film and they have 500 nm of Al on top and on bottom (blue curve). In order to show the frequency tunability allowed by mass loading and trimming, keeping the thickness of the bottom electrode constant, 300 nm have been selectively (red curve) removed, increasing the resonant frequency and (yellow curve) added, decreasing it.

The difficulty in tuning the resonant frequency has been overcome by another resonator topology: the Contour Mode Resonator (CMR). CMRs rely on the S_0 Lamb-Wave mode, which exploits the vertical field (as FBARs) but have the displacement in the lateral direction. Their simplest geometry is the same as the one of the FBAR, and is shown in Fig. 2.4a-b. The resonant frequency is given by:

$$f_{res} = \frac{1}{2W} \cdot \sqrt{\frac{C_{11}}{\rho}} \quad (2.2)$$

where W is the width of the piezoelectric plate and C_{11} is the stiffness coefficient involved. As mentioned in [18], in order to scale the device to higher frequency, there is just the need to reduce the width. The problem here is the lowering of the static capacitance C_0 , which tends to become too small and does not allow the 50Ω -matching required to transfer the maximum power of the generator to the device and minimize the signal reflection from the load. The solution to this was found in the mechanical coupling of a number N of CMRs whose width has been reduced enough to make them work at the desired frequency (Fig. 2.4c). Doing so, an higher-order mode is excited at the same frequency, and the C_0 is

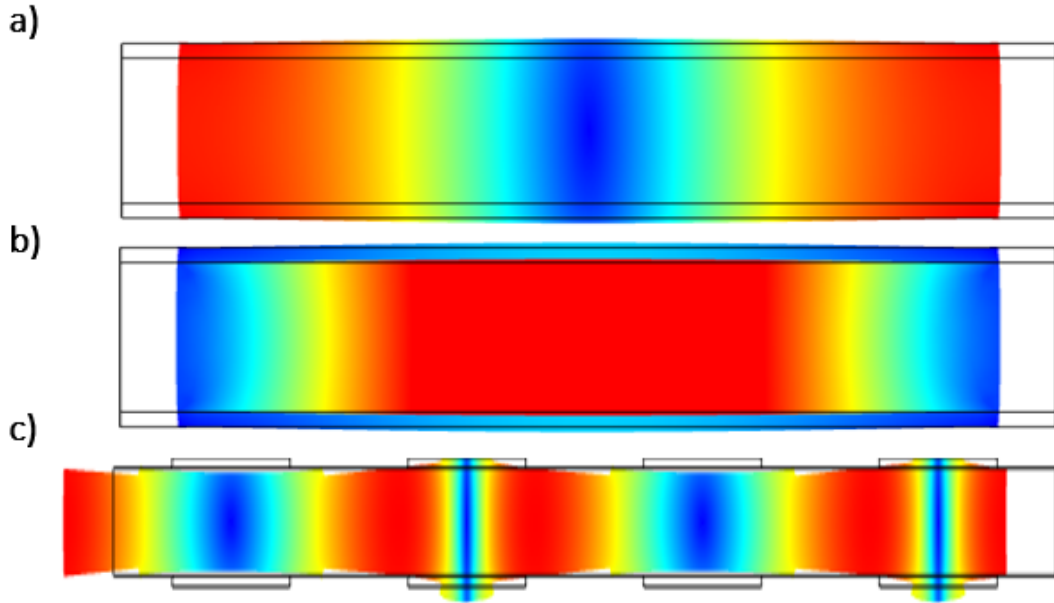


Figure 2.4: COMSOL® simulation of CMRs. In a) and b) the geometry is the same of FBARs, but the mode shape is different, having displacement in the lateral direction. a) shows the displacement, while b) the stress distribution. On the contrary, c) shows the structure presented in [18], in which a number N of CMRs is mechanically coupled in order to set the desired static capacitance C_0 .

the sum of all the C_0 of the resonators. Despite the very convenient tunability of the resonant frequency, which can be lithographically set (Eq. 2.2), CMRs lack in k_t^2 . In particular, they rely on the e_{31} piezoelectric coefficient, whose value for AlN is -0.58 C/m^2 , with a modulus that is about one third of the one of e_{33} . This lower coefficient sets a physical limit to CMRs, which cannot attain the same electromechanical (EM) coupling of FBARs.

In order to combine the two strength points of the aforementioned resonators, a new class was introduced in 2016, the Cross-Sectional Lamé'-mode Resonator (CLMR) [12].

2.2 Cross-sectional Lamé' Mode Resonator

The Cross-sectional Lamé' Mode Resonator takes advantage of both the e_{31} and e_{33} coefficients to transduce resonant vibration. In particular, under certain assumptions, the S_0 and S_1 modes couple, generating a two-dimensional mode of vibration, along both the thickness and the width. The mode shape and the stress distribution of a CLMR at resonance can be seen in Fig. 2.5a-b. It can be observed that, as in the case of an FBAR, along the thickness there are two maxima and a minimum of displacement while, as in a CMR, there is no displacement under the electrode while the maximum is in the uncovered region. As a CMR, a higher

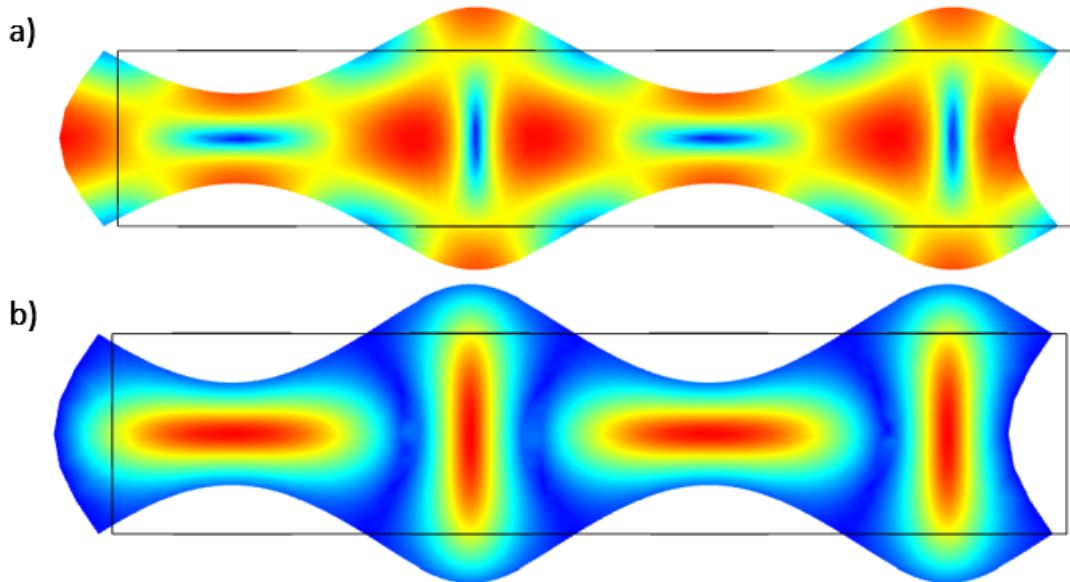


Figure 2.5: COMSOL® simulation CLMRs showing a) the displacement and b) the stress field.

order CLMR utilizes Interdigitated transducers (IDT) to excite the mode and set the desired C_0 .

Let's now define the physics behind a Cross-Sectional Lamé' Mode (CLM) of the first order. In [12], the fundamental equations are derived starting from the ones of the motion in a solid, using the theory of Lamb Waves in an AlN plate. The particularity of this mode is that it is two-dimensional and therefore shows same peak-to-peak displacements along the thickness ($\widetilde{\mu}_z$) and the width ($\widetilde{\mu}_x$) direction. Given β_z and β_x the wave-vectors relative to the motion along the z and x direction:

$$\begin{bmatrix} \widetilde{\mu}_x \\ \widetilde{\mu}_z \end{bmatrix} = \begin{bmatrix} \cos(\beta_x x) \sin(\beta_z z) \\ -\sin(\beta_x x) \cos(\beta_z z) \end{bmatrix} \quad (2.3)$$

The two equations of motion describing the displacement distribution in an AlN plate are:

$$C_{11} \frac{d^2 \mu_x}{dx^2} + C_{55} \frac{d^2 \mu_x}{dz^2} + 2C_{15} \frac{d^2 \mu_x}{dx dz} + (C_{55} + C_{13}) \frac{d^2 \mu_z}{dx dz} = (2\pi f_{res})^2 \rho \mu_x \quad (2.4)$$

$$C_{15} \frac{d^2 \mu_x}{dx^2} + C_{55} \frac{d^2 \mu_z}{dz^2} + C_{33} \frac{d^2 \mu_z}{dz^2} + (C_{55} + C_{13}) \frac{d^2 \mu_x}{dx dz} = (2\pi f_{res})^2 \rho \mu_z \quad (2.5)$$

where the C_{ij} are the stiffness coefficients, and ρ the mass density. If one substitutes to μ_x and μ_z the $\widetilde{\mu}_x$ and $\widetilde{\mu}_z$ of Eq. (2.3), Eqs. (2.4-2.5) are simplified to:

$$C_{11} \beta_x^2 - (C_{55} + C_{13}) \beta_x \beta_z + C_{55} \beta_z^2 = (2\pi f_{res})^2 \rho \quad (2.6)$$

$$C_{33} \beta_z^2 - (C_{55} + C_{13}) \beta_x \beta_z + C_{55} \beta_x^2 = (2\pi f_{res})^2 \rho \quad (2.7)$$

This system of equations gives four possible sets of β_x and β_z , but only one has physical sense, i.e. the one having both the wave-vectors with positive values. In particular, their expression is:

$$\widetilde{\beta}_x = \sqrt{\frac{B\rho(2\pi f_{res})^2}{C_{11}C_{33} - C_{55}^2 + \sqrt{AB}}} \quad (2.8)$$

$$\widetilde{\beta}_z = \widetilde{\beta}_x \sqrt{\frac{C_{11} - C_{55}}{C_{33} - C_{55}}} \quad (2.9)$$

where $A = (C_{11} - C_{55})(C_{13} + C_{55})^2$ and $B = (C_{33} - C_{55})$. Concerning the boundary conditions, all the sides of the CLMR can be considered as stress-free. This means that the wave-vectors have to satisfy the following equations:

$$\widetilde{\beta}_x = \frac{n \times \pi}{W} \quad (2.10)$$

$$\widetilde{\beta}_z = \frac{m \times \pi}{h} \quad (2.11)$$

In the equations above, n and m set the mode number regarding the x and z directions, respectively. The resonant frequency can be found by substituting Eq. (2.10) into Eq. (2.8):

$$f_{res} = \frac{1}{\lambda_x} \sqrt{\frac{C_{11}C_{33} - C_{55}^2 - (C_{31} + C_{55})\sqrt{(C_{11} - C_{55})(C_{33} - C_{55})}}{(C_{33} - C_{55})\rho}} \quad (2.12)$$

where $\lambda_x = 2\pi/\beta_x$. This equation states that the resonant frequency can be tuned by changing the horizontal acoustic wavelength. Finally, by replacing Eqs. (2.10-2.11) into Eq. (2.9), the ratio of λ_x and h that allows a CLM to generate into the piezoelectric plate is obtained:

$$\frac{\lambda_x}{h} = 2\sqrt{\frac{C_{11} - C_{55}}{C_{33} - C_{55}}} \quad (2.13)$$

This condition assures that the phase velocity of the longitudinal and transverse waves are the same. This equation must be strictly satisfied if one wants to obtain a non-degenerate CLM. What distinguishes a degenerate from a non-degenerate CLM is the value of electromechanical coupling (k_t^2) which can be attained. In the second case it will be higher. The k_t^2 is defined as:

$$k_t^2 = \frac{\pi^2}{8} \frac{f_p^2 - f_s^2}{f_s^2} = \frac{\pi^2}{8} \frac{C_m}{C_0} \quad (2.14)$$

where f_s and f_p are the series and parallel resonant frequencies, respectively, and C_m and C_0 are the motional and static capacitance of the resonator, respectively. Thus, the k_t^2 is a measure of how much energy is transduced from the electrical to the mechanical domain, or vice versa. Doing a theoretical analysis, it makes sense to introduce the piezoelectric coupling constant K^2 , whose value gives the maximum k_t^2 attainable for a specific vibration mode. Since a CLMR is characterized by the coupling of modes along two different directions, the overall K^2 will depend on the coupling of both of them, i.e. it will have two components originated by the motion along the thickness (K_z^2) and the width (K_x^2), respectively. Those components can

be calculated with the aid of the Christoffel's equations [12], which lead to the coefficients $K_{Chr[x]}^2$ and $K_{Chr[z]}^2$. In particular, the resulting coupling constant will have the form:

$$K_{CLM}^2 = \frac{2}{\pi}(K_{Chr[x]}^2 + K_{Chr[z]}^2) = 7.1\% \quad (2.15)$$

where:

$$K_{Chr[x]}^2 = \frac{e_{31}^2}{\varepsilon C_{lat}} \quad (2.16)$$

$$K_{Chr[z]}^2 = \frac{e_{33}^2}{\varepsilon C_{thic}} \quad (2.17)$$

where C_{lat} and C_{thic} are the equivalent stiffness constants of the two vibrational modes constituting a CLM, and have the expression:

$$C_{lat} = \frac{C_{11}C_{33} - C_{55}^2 - (C_{13} + C_{55})\sqrt{(C_{11} - C_{55})(C_{33} - C_{55})}}{C_{33} - C_{55}} = 320 \text{ GPa} \quad (2.18)$$

$$C_{thic} = C_{lat} \frac{C_{33} - C_{55}}{C_{11} - C_{55}} = 300 \text{ GPa} \quad (2.19)$$

The values shown are intended for AlN. As previously mentioned, in order to obtain the desired value of static capacitance, higher order modes are exploited through the use of IDTs. In [12], two CLMR configurations are described: the double-IDT or Thickness Field Excited (TFE) and the single-IDT or Lateral Field Excited (LFE) CLMR (Fig. 2.6a-b). The first is the one that allows to attain the highest EM coupling coefficient values, since it can count on an electric field both in the lateral and thickness direction. The drawback is the fabrication complexity: this device requires at least four lithographic masks. The second one trades-off k_t^2 in favour of a simpler fabrication, which consists of two masks. The reason for the smaller coupling lies in the presence of only the lateral component of the electric field. In [19], other common Lamb-Wave resonator topologies are shown. From it, I included in the topologies under study one more, which I called Bottom Electrode (BE) CLMR (Fig. 2.6c). This structure has been used for CMRs [20] but not for CLMRs. It consists of a LFE CLMR with a floating BE, and shows higher k_t^2 values compared to the LFE one. The reason is found in the BE, which provides a double-way path for the electric field in the thickness direction. The fabrication complexity is higher compared to the LFE, but lower than the one of the TFE, consisting of three lithographic masks. Nevertheless, avoiding a mask would not justify the degradation of EM coupling that can be observed. The advantage of this

topology relies on the fact that, being the BE continuous under the resonator plate, the piezoelectric thin film will grow on top of it with a better quality, meaning that there will be no degradation of the piezoelectric coefficients. The same thing does not happen for the patterned bottom electrode of the TFE CLMR.

2.3 Transducer design

In [19], great focus is given to the metallic IDTs, i.e. the transducer. Their design has a great impact on the final performances of the resonator. There are multiple degrees of freedom in the design of an IDT: the material choice, the thickness, the pitch and the metallization ratio. The choice of the material impacts the resonant frequency, the EM coupling and the quality factor (Q). In the present work, Aluminum (Al), Platinum (Pt), Molybdenum (Mo) and Tungsten (W) have been taken into consideration and studied. Different metals have different densities, therefore a different impact on the resonator performances. In particular, high density metals (e.g. Pt, W) shift the resonant frequency due to an enhanced mass loading. What physically happens is that, being the metal heavy, it strains the piezoelectric film generating charges inside it, which shift the resonant frequency to lower values. Concerning the impact on the k_t^2 , it was shown in [19] that metallic

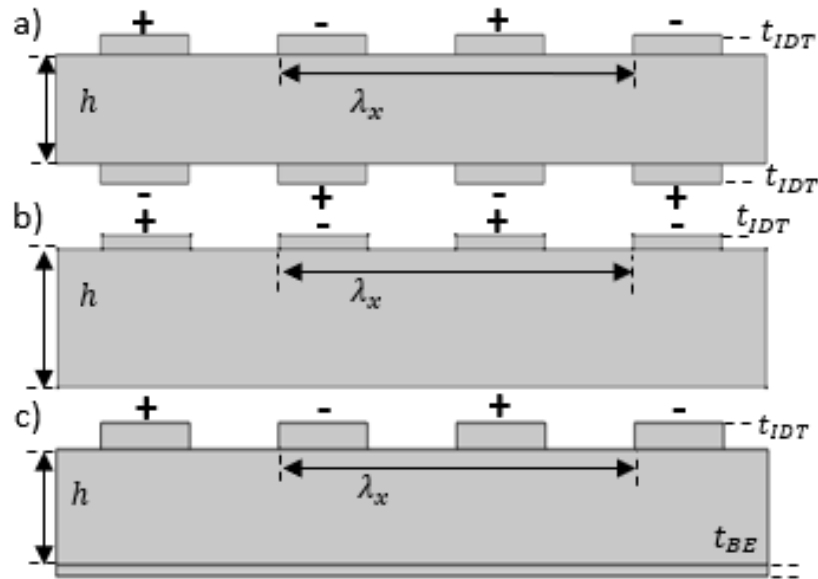


Figure 2.6: Investigated CLMR topologies: a) TFE b) LFE and c) BE CLMR. For each configuration, the terminal scheme is shown, together with the geometrical dimensions.

electrodes strengthen the resonant mode, i.e. they increase the EM coupling. In particular, the increase is proportional to the difference in acoustic impedance between the piezoelectric film and the metal, where the acoustic impedance is defined as the opposition of a certain material to the acoustic flow passing through it, and is quantified by the expression:

$$Z = \sqrt{\rho \times E} \quad (2.20)$$

	Al	Pt	Mo	W
Density, ρ [kg/m ³]	2700	21450	10200	19350
Young's Modulus, E [GPa]	70	168	312	411
Acoustic impedance, Z [MPa·s/m ³]	13.7	60	56.4	89.2
Resistivity, ρ_r [nΩ · m]	28.2	112	53.4	56

Table 2.1: Density, Young's Modulus, Acoustic Impedance and Resistivity of the studied metals.

where E is the Young's modulus of the metal or the equivalent stiffness coefficient of the piezoelectric film in the motion direction. The densities (ρ), Young's moduli (E) and acoustic impedances (Z) of the metals taken into consideration are listed in Table 2.1. From it, the higher k_t^2 values are expected with W as electrode material. Nevertheless, the electrode metal has an impact also on the Q through the electrical loading. This is a loss mechanism due to the finite resistivity of the material, for which part of the energy is dissipated in the electrode through Joule effect. Also the values of resistivity are shown in Table 2.1 for the considered materials.

Concerning the thickness, it impacts the resonant frequency through mass loading, i.e. a thicker metal will weight more on the piezoelectric film, and the EM coupling. In [19] it is shown how a thicker metal will increase the k_t^2 due to a stiffening effect of the piezo-layer. On the other hand, it can be shown that thicker metals tend to shift the stress field from the resonator body into the electrodes which, being piezoelectric-dead cannot transduce it [21]. This effect is shown in Fig. 2.7, in which the Von Mises Stress can be seen to progressively shift the distribution inside the electrodes of a TFE CLMR as their thickness increases. Therefore, there exist an optimal thickness which provides a trade-off between the aforementioned effects and maximizes the k_t^2 .

The pitch has a strong impact on the resonant frequency, the static capacitance and the EM coupling. In a CLMR, the pitch (p) is defined as half the horizontal acoustic wavelength, therefore changing it changes the λ_x and shifts the resonant frequency according to Eq. (2.12). Moreover, the smaller the pitch, the higher the static capacitance per unit cell of the CLMR. During my work, I developed a

simple model to have an estimation of the static capacitance of different topologies of CLMR, and it is shown in Appendix A. Anyway, it can be intuitively observed that, since the metal electrodes behave like the plates of a capacitor, the closer they are to each other, the higher is the resulting value of the capacitance between them. Concerning the impact on the EM coupling, it has been previously shown that the relation between the piezoelectric thickness h and the acoustic wavelength λ_x in order to have a non-degenerate CLM must strictly obey Eq. (2.13). Nevertheless, that equation is defined for simple piezoelectric layer, and does not take into account the presence and the mass loading of the metallic electrodes. In particular, they tend to shift the optimal ratio to lower values of h/λ_x , and the effect is more marked in the TFE CLMR case due to the presence of two IDTs.

Finally, the metallization ratio (α) is defined as the ratio between the metallized region of a pitch and the pitch itself. It impacts the resonant frequency, the static capacitance, the quality factor and the EM coupling. The first is shifted to slightly lower or higher values due to a change in the effective acoustic velocity of the propagating wave made by the metal. The variation of the second is due to an increase or decrease of the distance between the electrodes if α decreases or

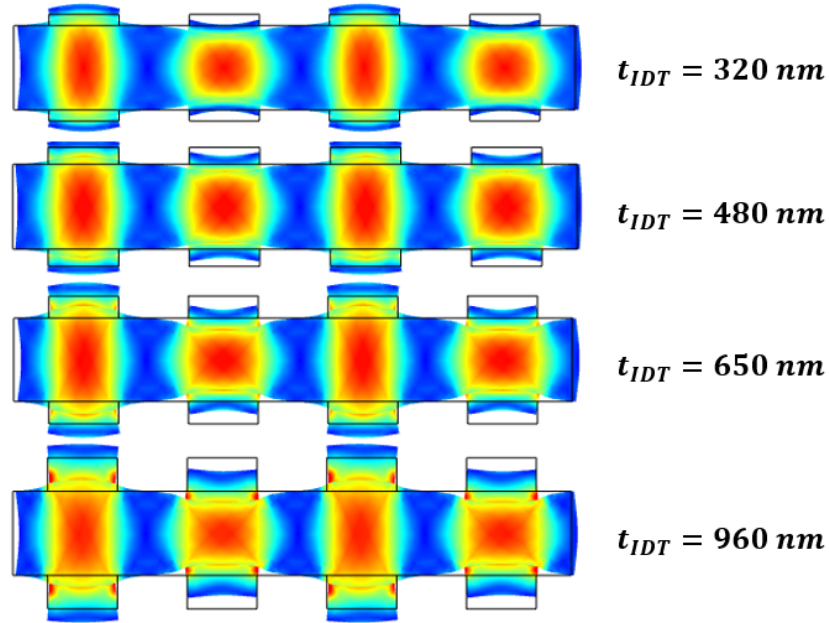


Figure 2.7: Von Mises Stress distribution inside a TFE CLMR with W electrodes as its thickness increases. It is clearly visible that the points with higher values tend to shift inside the metal, thus reducing the overall EM coupling. The figure has been obtained using Finite Element Analysis with COMSOL®.

increases, respectively. The Q is impacted by electrical loading in the sense that narrower electrodes will provide a higher resistance than wider ones.

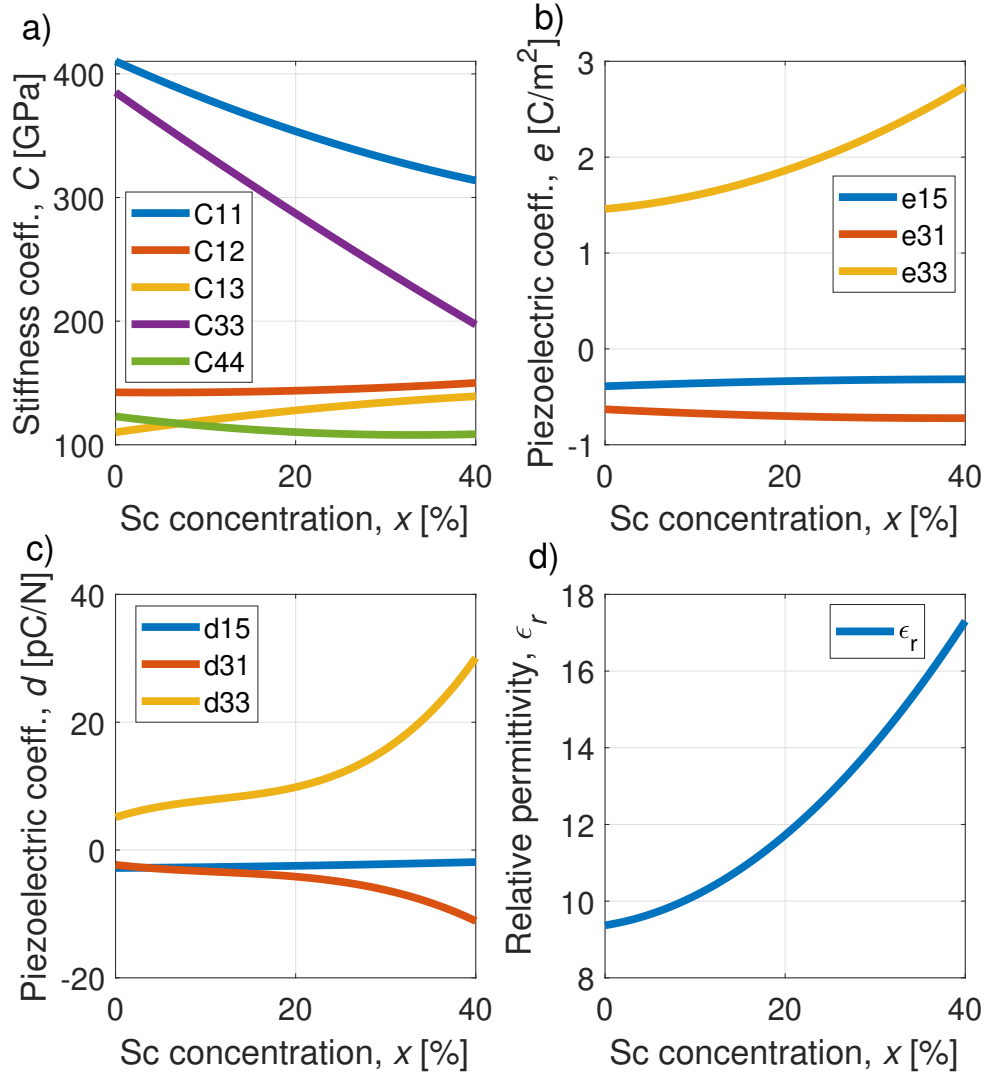


Figure 2.8: Scaling of mechanical (C), piezoelectric (d, e) and dielectric (ϵ_r) properties of ScAlN with dopant concentration ranging from 0 to 0.4. The plots are based on the ab-initio equations derived in [22].

2.4 Scandium doping of CLMRs

One of the main goals of this section on CLMRs, is the study of the impact of Sc-doping of the AlN film. Sc-doping has proven to be effective in increasing the k_t^2 of FBARs and CMRs [20]. Even if CLMRs made of ScAlN have already been reported in literature [20][21], a systematic study of the change in performances for different topologies and different electrode materials with the Sc-doping level is not present. As previously shown, the doping of AlN has impact on its mechanical, dielectric and piezoelectric behaviour. In [22], ab-initio equations for the stiffness and piezoelectric coefficient and for the dielectric permittivity are derived from the density functional theory and Berry-phase theory. Fig. 2.8a-d shows how the aforementioned quantities vary with Sc percentage going from 0 to 40%, while Table 2.2 lists the differences between the material constants of AlN and of ScAlN at 0%. As it can be observed, they are really close. Higher doping values are not taken into account since when doping is too high, ScAlN ceases to be piezoelectric and becomes a non-polar rock salt.

	C_{11} [GPa]	C_{12} [GPa]	C_{13} [GPa]	C_{33} [GPa]	C_{44} [GPa]
AlN	410	149	99	389	125
0% ScAlN	410.2	142.4	110.1	385	122.9
	C_{66} [GPa]	e_{31} [C/m ²]	e_{33} [C/m ²]	e_{15} [C/m ²]	ϵ_r
AlN	130.5	-0.58	1.55	-0.48	9
0% ScAlN	133.9	-0.63	1.46	-0.39	9.37

Table 2.2: Comparison between the material constants of AlN and of ScAlN at 0% doping.

The graphs of Fig. 2.8 show the softening effect due to doping (a), the increase of the modulus of the piezoelectric coefficients (b-c) and the increase in dielectric constant (d). The combination of these effects results in an increased EM coupling. The change in the stiffness C coefficients reflects in a change in the equivalent stiffness constants of the CLM, described in Eqs. (2.18-2.19). Their behaviour with respect to Sc-doping is shown in Fig. 2.9a. As it can be observed, both undergo an effective softening. These constants, together with the piezoelectric coefficients e_{31} and e_{33} , appear in the equation of the K^2 , thus modifying it. Its variation is shown in Fig. 2.9b. As it can be observed, it reaches the astonishing value of 40%. To make CLMRs even more interesting to study, in [23] it was demonstrated how those resonators are able to attain higher values of EM coupling with respect to FBARs at 40% Sc. The reason can be found not in the presence of the e_{31} piezoelectric coefficient, but on the higher softening of the vertical equivalent stiffness constant

C_{thic} , which gets impacted more than the C_{33} of FBARs.

Concerning the resonant frequency of devices in ScAlN in general, it is shifted to lower values due to the softening effect. Fig. 2.10a depicts the percentile reduction of f_{res} with the Sc-doping concentration with respect to the frequency of a CLMR in pure AlN, obtained by varying the Sc percentage in Eq. (2.12). The same procedure has been used on Eq. (2.13), obtaining the optimal h/λ_x for the different doping levels. As it can be observed in Fig. 2.10b, this optimum shifts from about 0.5 of pure AlN to 0.33 of 40% doped ScAlN. As it will be observed in the next paragraph, this effect is almost negligible compared to the one induced by the mass-loading of the metal electrodes.

2.5 Simulation of CLMRs

2.5.1 2D simulations

A study of the impact of different metal electrode materials, dimensions and Sc concentration has been carried out during the present work for the three topologies of TFE, LFE and BE CLMR. The study has been carried on through Finite Element

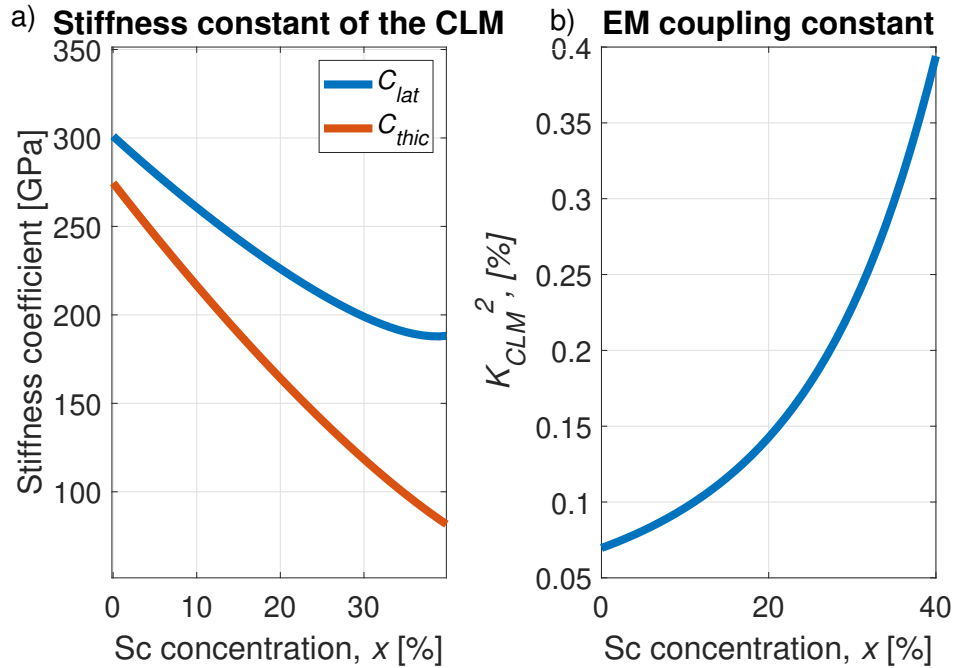


Figure 2.9: a) Variation of the equivalent stiffness constants for the CLM (C_{lat} , C_{thic}) with the Sc concentration, b) variation of the piezoelectric coupling constant of the CLM (K_{CLM}^2) with Sc-doping.

Analysis (FEA) by the use of COMSOL® 2D models. The employed physics was Piezoelectricity, and the study was a Frequency Domain one. The structures under study are shown in Fig. 2.6a-c. An infinite number of IDT fingers has been simulated by applying Periodic Boundary Conditions (PBC) at the resonators edges both in the Electrostatics and Solid Mechanics modules. In this way, edge effects are not taken into account. Fig. 2.6a-c also show the electrical boundary conditions applied to generate the Terminal (+) and Ground (-). To take into account the changes in the material properties of AlN due to the adding of Sc atoms, a new custom material (ScAlN) has been introduced. The values of the elements of the stiffness, piezoelectric and dielectric matrices are based on the ab-initio equation found in [22]. In this way, by simply changing a single variable, namely the doping level x , values from 0 to 0.4 of Sc percentage were simulated.

Concerning the geometry of the resonators, in order to make them scalable in frequency, every parameter has been written as function of the horizontal acoustic wavelength λ_x . This includes the thicknesses piezoelectric layer (h_{ScAlN}), of the IDTs (t_{IDT} , t_{top} , t_{bot}) and of the bottom electrode (t_{BE}). As a demonstration of the scalability, Fig. 2.11a-b shows the admittance (Y_{11}) as function of the frequency

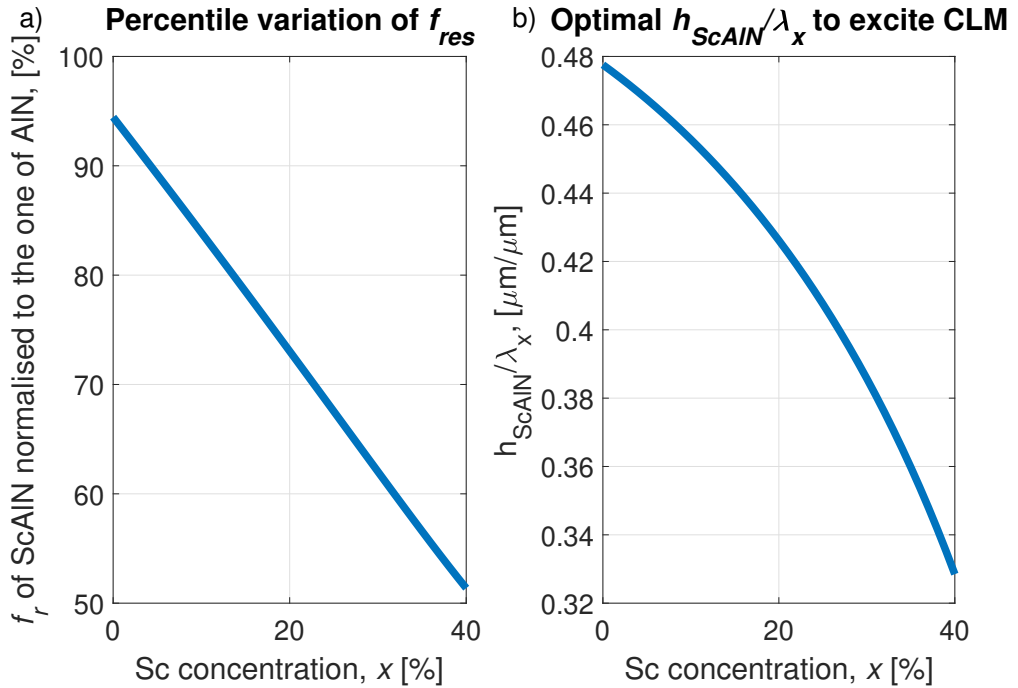


Figure 2.10: a) Resonant frequency of CLMRs in ScAlN normalized to the one of pure AlN, b) variation of the ratio of h_{ScAlN}/λ_x to excite a non-degenerate CLM with the Sc-doping level.

f for a TFE CLMR with (a) $\lambda_x = 8\mu m$ and (b) with $\lambda_x = 2\mu m$. As it can be observed, in the second case, being the wavelength one quarter of the first case, the resonant frequency is four times higher, according to Eq. 2.12. The k_t^2 is the same for the two devices.

The first study consisted in finding the h_{ScAlN}/λ_x ratio that allows to obtain the highest k_t^2 for the different electrode material and the different topologies of CLMRs at 0% Sc. Recalling that, on pure AlN without the IDTs, the optimal ratio should be almost 0.5, when the electrodes are introduced, their mass loading shifts the optimum to lower levels. A similar analysis was found for Lamb-Wave resonators in [19]. A λ_x of $8\mu m$ was considered, and the thickness of the piezoelectric layer swept from $0.08\lambda_x$ to $0.5\lambda_x$ in the case of the TFE CLMR, and from $0.2\lambda_x$ to $0.6\lambda_x$ in the other cases. The EM coupling was then extracted from the obtained Y_{11} vs. f curves using the formula of Eq. (2.14). Fig. 2.12a-c show the curves of k_t^2 vs. h_{ScAlN}/λ_x for TFE, LFE and BE CLMRs, respectively, for W, Pt, Al and Mo as electrode materials. A thickness $t_{IDT} = 0.04\lambda_x$ and $t_{BE} = 0.02\lambda_x$ was considered as benchmark. As it can be observed, the optimal values are far from the 0.5 of the film without electrodes. Moreover, there exist a correlation between the density of

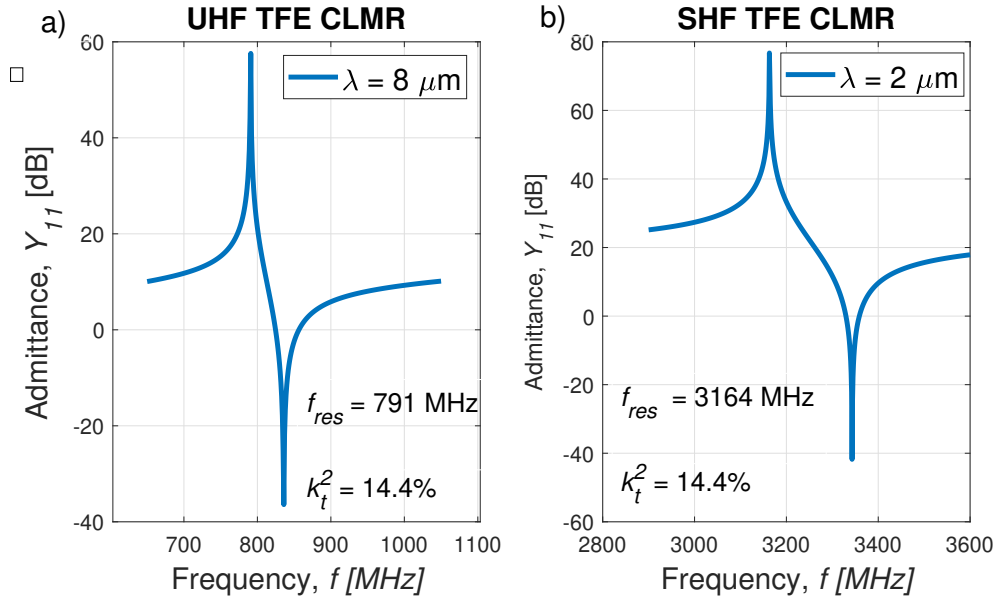


Figure 2.11: Comparison of the admittance Y_{11} vs. frequency f for two ScAlN TFE CLMR with W electrodes and 20% Sc concentration. The resonator horizontal acoustic wavelength λ_x is a) $8\mu m$ and b) $2\mu m$, which inserts the resonant frequencies in the Ultra High Frequency (UHF) and Super High Frequency (SHF) ranges, respectively. As it can be observed from the f_{res} in the insets, its value in b) is exactly four times the one in a). The k_t^2 is precisely the same.

the metal and the shift of the optimal ratio. In particular, the denser the metal, the greater the shift. Additionally, also the specific topology has an impact, e.g. the ratio that maximizes the EM coupling is lower in the case of the TFE CLMR with respect to the LFE one. The reason is the presence of the double IDT that introduces more mass loading than a single one. The best metal proves to be W, and it was the expected result since among them is the one which has a higher mismatch in acoustic impedance with ScAlN. Finally, the curves in Fig. 2.12a-c also show the capability of CLMRs of tuning the resonant frequency: different h_{ScAlN}/λ_x ratios mean different f_{res} , and from the graphs it is clear that there exist a window of values which allows to attain high EM coupling. Therefore, on a wafer, simply by changing the wavelength, the frequency is shifted without major degradation of k_t^2 .

Up to now, a random thickness of the electrodes has been considered. In order to optimize the devices performances, the best thicknesses must be found. Therefore, using the same method of the previous study, the k_t^2 vs. h_{ScAlN}/λ_x curves have been extracted for the aforementioned materials for t_{IDT}/λ_x ranging from 0.02 to 0.12. For the case of the BE CLMR, once the best t_{IDT} was found, t_{BE} was swept from $0.01\lambda_x$ to $0.06\lambda_x$. The results are shown in Fig. 2.13a-b for the TFE and LFE CLMR, respectively, and in Fig.2.13c-d for the BE one. The electrode material is W and has been chosen as a benchmark. The curves for the other

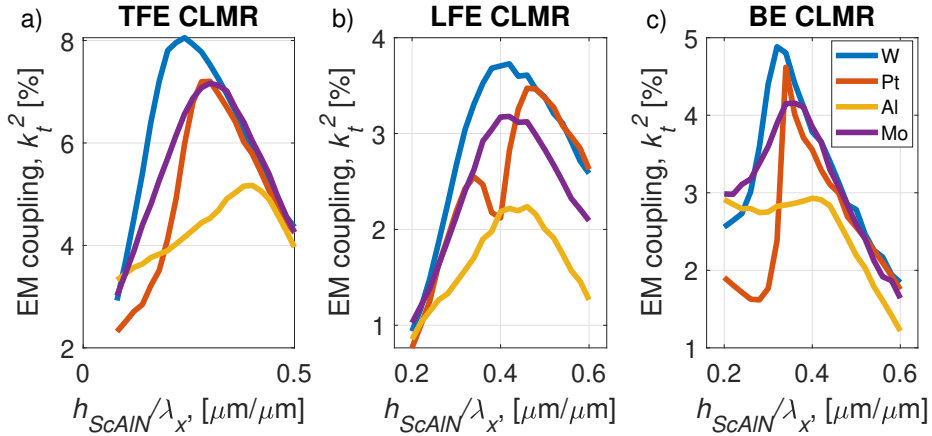


Figure 2.12: k_t^2 vs. h_{ScAlN}/λ_x curves for the structures of TFE (a), LFE (b) and BE CLMR (c). The wavelength is $8\mu\text{m}$, the IDT thickness t_{IDT} is set to be $0.04\lambda_x$ and the one of the BE is $0.02\lambda_x$. The doping level is 0%. The presence of a single maximum means that only a specific ratio creates a non-degenerate CLM. In b) the Pt case has two peaks, but it is just the effect of a spurious mode close to the resonance induced by the electrodes that reduces the EM coupling for some ratios. As it can be observed, the value of the optimal ratio is different from 0.5.

materials are similar. What can be observed is that, according to what stated in Section 2.3, increasing the metal thickness stiffens the piezoelectric increasing the EM coupling up to a maximum, from which it decreases due to the shifting of the stress field from the plate into the metal. In Fig. 2.14-c the curves of EM coupling vs. h_{ScAlN}/λ_x taken for the devices with the optimized geometry are shown for the TFE, LFE and BE CLMR topology, respectively. The values of t_{IDT} and t_{BE} for the best case of each material and topology are listed in Table 2.3.

	TFE CLMR	LFE CLMR	BE CLMR	
	$t_{IDT} [\lambda_x]$	$t_{IDT} [\lambda_x]$	$t_{IDT} [\lambda_x]$	$t_{BE} [\lambda_x]$
Al	0.08	0.1	0.1	0.02
Pt	0.04	0.04	0.04	0.01
Mo	0.06	0.1	0.1	0.02
W	0.04	0.08	0.06	0.02

Table 2.3: Values of IDT and BE thickness for the various electrode materials that allow to obtain the k_t^2 vs. h_{ScAlN}/λ_x curves with the highest EM coupling coefficients. For the LFE and BE case, when using Pt as electrode material, the metallization ratio α has been changed to 0.35 and 0.3, respectively, in order to shift a spurious mode due to the electrodes out of the frequency range of interest. This is the reason why the curves for the LFE CLMR with Pt electrodes of Figs. 2.12 and 2.14 are different.

The metallization ratio α has an effect on the wave propagation. In particular, it changes the waves phase velocity due to a different alternation of metallized and non-metallized regions. Moreover, an effect similar to the one of the IDT thickness can be observed: increasing the metallization ratio increases the k_t^2 due to a better reflection of the waves by the electrodes which more efficiently confine the displacement field inside the piezoelectric plate [19]. Nevertheless, higher α values tend to shift the stress field from the plate in the electrode, thus reducing the EM coupling. In order to find the best metallization ratio, α has been swept from 0.2 to 0.8 for the various materials, and the results are shown in Fig. 2.15. The TFE CLMR structure has been chosen as a showcase. The IDT and piezoelectric film thickness for each material is the optimal one obtained from the previous analysis. As it can be observed, there exist a single optimal value, i.e. $\alpha = 0.5$. This result is different from the one of [19], in which the authors found 0.55 as optimum. The reason for the mismatch may be found in the slightly different material constants (C_{ij} , d_{ij} and ε_r) used in the analysis.

Using the optimized geometries, ScAlN CLMRs were simulated at different concentrations up to 40% in order to study the impact of doping. Fig. 2.16a-c

shows the k_t^2 vs. h_{ScAlN}/λ_x curves for TFE, LFE and BE CLMRs with W electrodes for different Sc percentages, namely 0, 20 and 40%. The k_t^2 is notably increased with increasing doping level showing a non-linear trend. The optimal h_{ScAlN}/λ_x ratio at high Sc percentage is shifted to slightly lower values with respect to lower

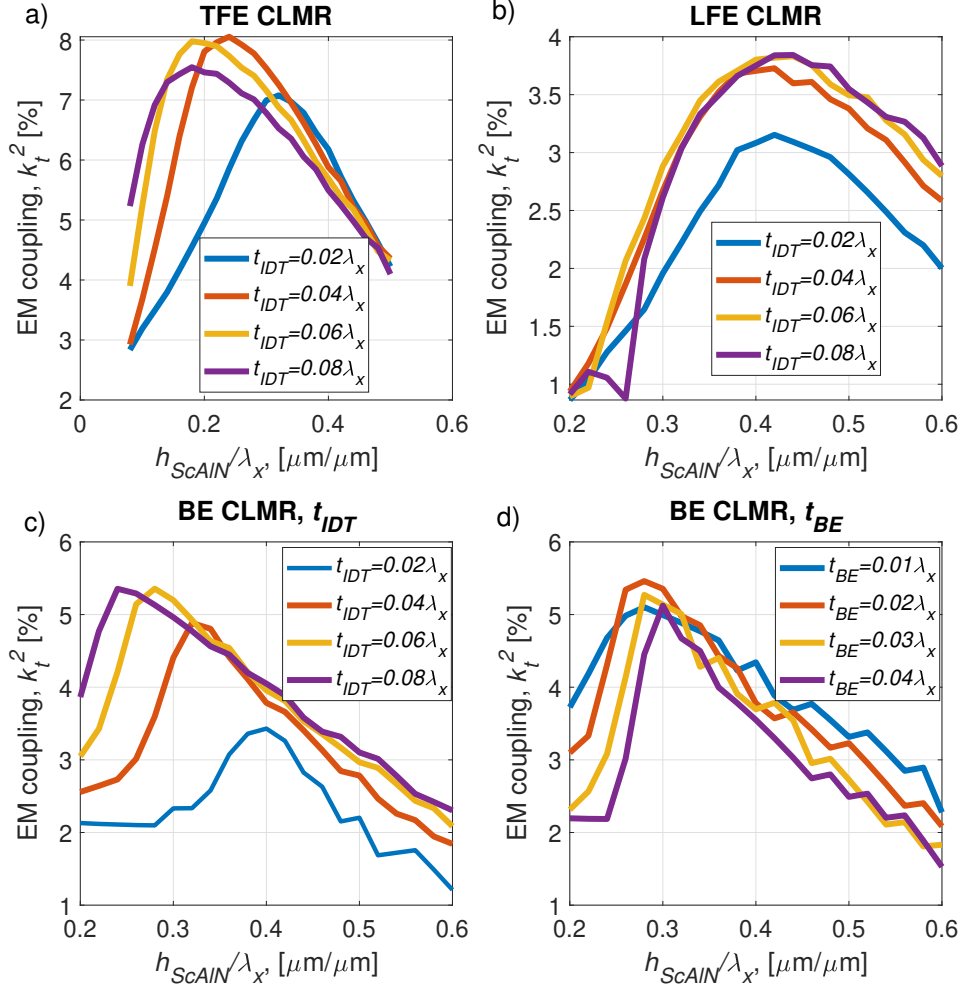


Figure 2.13: k_t^2 vs. h_{ScAlN}/λ_x curves for the structures of TFE (a), LFE (b) and BE CLMR (c-d) for different IDT and BE thicknesses with W electrodes. The curves show the optimization step followed in the study of the best IDT and BE thickness for the various topologies. Figures a)-c) show the optimization of the IDTs, while in d), once found the best thickness of the electrodes for the BE CLMR, the BE has been swept to find the optimal value.

doping. This agrees to what stated in Section 2.4. Nevertheless, it has to be pointed out that the reduction is very small compared to the effect of the metal. In the case of Al, which is lighter, the effect is more marked. To complete the

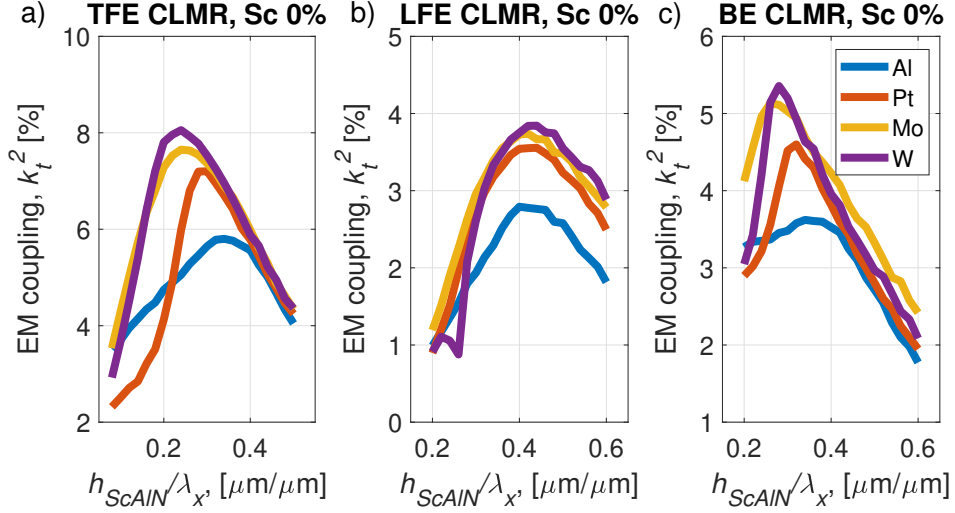


Figure 2.14: k_t^2 vs. h_{ScAlN}/λ_x curves for the structures of TFE (a), LFE (b) and BE CLMR (c) obtained using the optimized geometries. The values of t_{IDT} and of t_{BE} as function of λ_x are listed in Table 2.3.

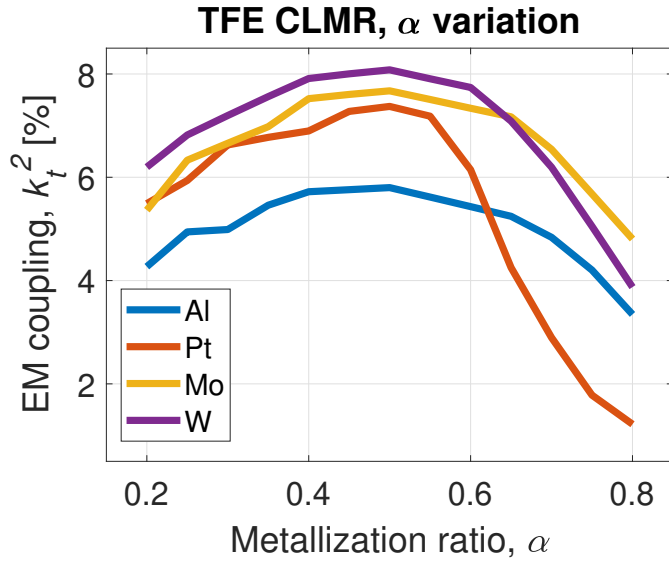


Figure 2.15: k_t^2 vs. α curves for the TFE structure which has been chosen as a showcase.

analysis, the curves of k_t^2 vs. h_{ScAlN}/λ_x for a Sc concentration of 40% are shown in Fig. 2.17a-c for the various electrode materials and topologies. The geometrical parameters are the optimal ones obtained in the analysis for 0% Sc concentration. In order to be able to better compare the results, in Table 2.4 the maximum k_t^2 for the best cases of 0% and 40% are listed. Recalling that commercial FBAR can rely on a k_t^2 of 7-8%, the obtained results have the potentiality of opening a lot of new application in the field of RF MEMS.

max k_t^2 [%]	TFE CLMR		LFE CLMR		BE CLMR	
	0% Sc	40% Sc	0% Sc	40% Sc	0% Sc	40% Sc
Al	5.8	30.2	2.8	12.2	3.6	20.8
Pt	7.2	35.4	3.6	14.8	4.6	23.5
Mo	7.6	36.1	3.7	15	5.1	25.8
W	8.1	36.2	3.8	14.5	5.4	26.2

Table 2.4: Comparison of the best EM coupling coefficients for the TFE, LFE and BE CLMRs for 0% and 40% Sc doping.

From the graphs in Fig. 2.14 and 2.17, it is clear that W is the electrode material

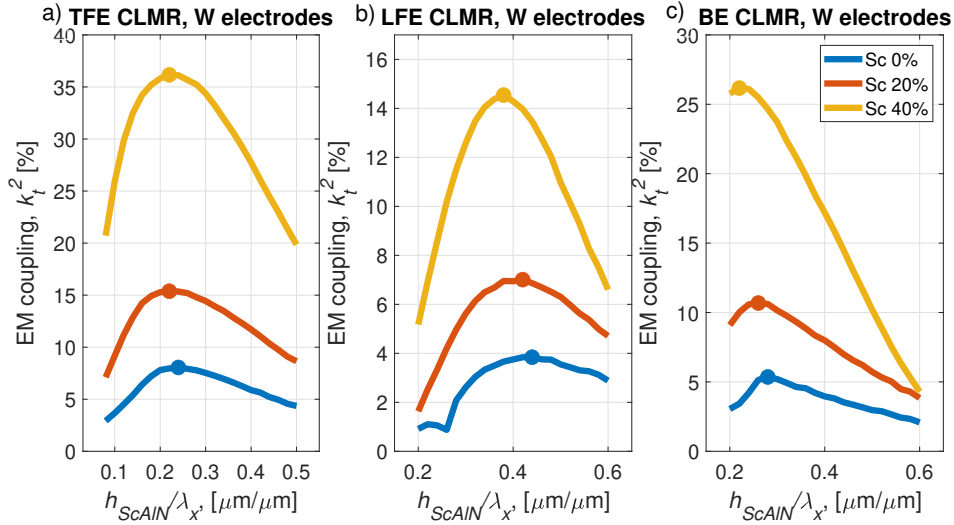


Figure 2.16: k_t^2 vs. h_{ScAlN}/λ_x curves for the structures of TFE (a), LFE (b) and BE CLMR (c) for different Sc concentrations, namely 0, 20 and 40%. The electrode material is W. The curves clearly show the k_t^2 boost introduced by the Sc-doping. The increase in EM coupling is non-linear with the dopant concentration. The maximum of each curve is highlighted.

which allows to attain the highest EM coupling coefficients. Nevertheless, the lattice of the sputtered W and its poor surface roughness prevent the growth of high quality, highly oriented (Sc)AlN crystallites. This results in a piezoelectric film with lower net d_{31} and d_{33} coefficients. For these reasons, AlN films are grown preferentially on Mo, Pt and Gold (Au) [24]. Moreover, W high resistivity creates higher degradation of the quality factor with respect to other metal choices due to electrical loading. Therefore, it is not the most desired choice for the top electrode, either. In order to impact as less as possible the quality factor, Al can be used. In cases like this, the best choice may be a combination of different metals for the top and bottom IDTs (or top IDT and BE). In the following, a method to optimize the thicknesses of the electrodes in the case of the usage of a multi-metal is established. Using the 2D COMSOL® model, a showcase for the TFE CLMR is given, but can be easily extended to the BE CLMR case. The top metal is Al, and the bottom one is Mo. In order to find the best thicknesses, three h_{ScAlN}/λ_x ratio are chosen, namely 0.2, 0.3 and 0.4. For each of them, the bottom electrode has been swept from $0.02\lambda_x$ to $0.14\lambda_x$, with $0.02\lambda_x$ step. For each t_{bot} , the top IDT thickness t_{top} has been swept from $0.02\lambda_x$ to $0.2\lambda_x$. Fig. 2.18a-c show the contour plots resulting from the aforementioned simulations, where the color shows the k_t^2 levels, for ScAlN at 0% doping. As it can be observed, there is the presence of one absolute maximum of EM coupling for each h_{ScAlN}/λ_x ratio. In order to make sure that the maxima are the same for highly doped AlN, the same plots

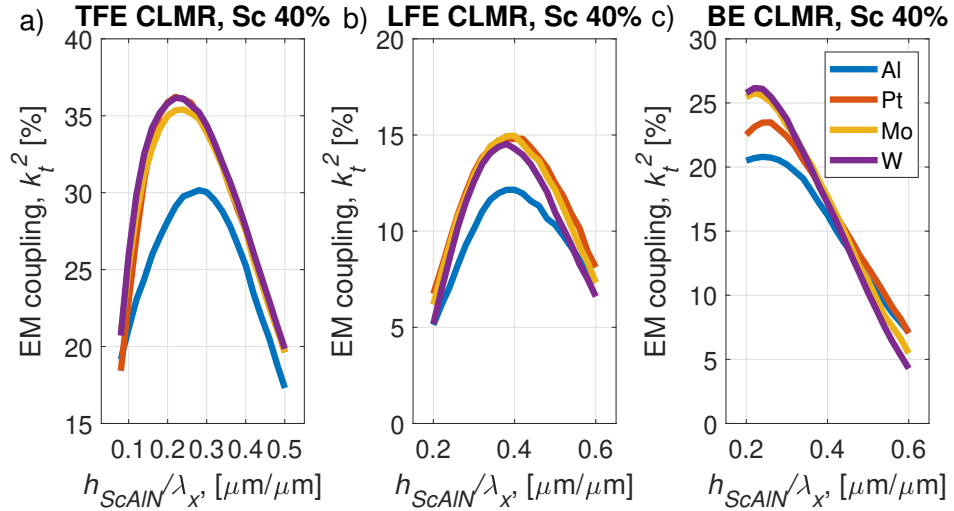


Figure 2.17: k_t^2 vs. h_{ScAlN}/λ_x curves for the structures of TFE (a), LFE (b) and BE CLMR (c) obtained using the optimized geometries. The doping level is 40%. The values of t_{IDT} and of t_{BE} as function of λ_x are the same as of the 0% case and are listed in Table 2.3.

have been prepared for 40% Sc concentration, and are shown in Fig. 2.18d-f. It is straightforward to notice that the maxima of k_t^2 have a broader window of t_{top} and t_{bot} , and the optima of the 0% case are included in the ones of 40%. After choosing as optimal points the ones with higher EM coupling for the case with 0% doping, two functions, for t_{top} and t_{bot} , respectively, have been quadratically fitted for h_{ScAlN}/λ_x ratios ranging from 0.08 to 0.5. The fittings are shown in Fig 2.19a-b. Fig. 2.20 shows the comparison of two curves of k_t^2 vs. h_{ScAlN}/λ_x

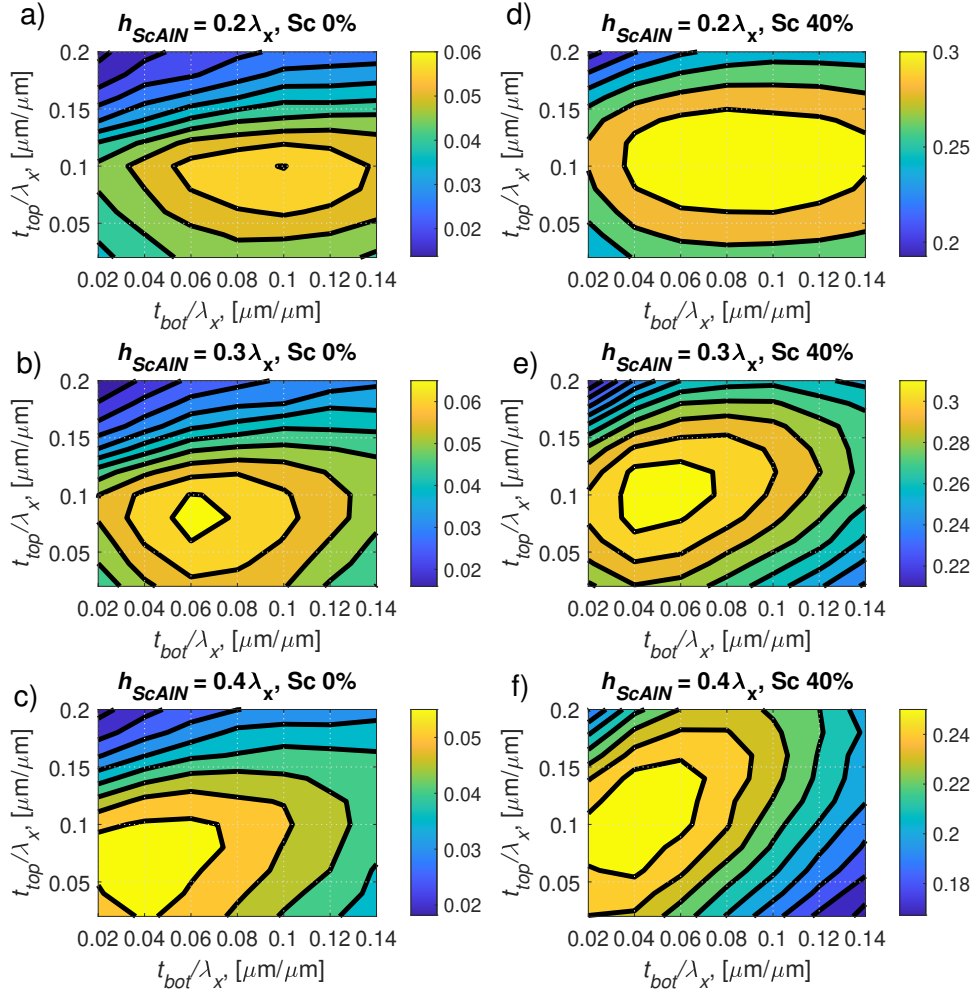


Figure 2.18: Contour plots of k_t^2 vs. t_{top} and t_{bot} for h_{ScAlN}/λ_x equal to 0.2, 0.3 and 0.4, for a)-c) 0% Sc and d)-f) 40% Sc, showing the optimal geometrical dimensions.

for $t_{top} = t_{bot} = 0.02\lambda_x$ and for the thicknesses following the fitting functions of Fig. 2.19a-b. The improvement in EM coupling is clearly visible. In particular, it increases from 4.5 to 6.5 in the best case scenario.

2.5.2 3D simulations

With the 2-dimensional approach, the most important geometrical parameters have been optimized, and their impact on the EM coupling and the resonant frequency studied. Nevertheless, a 2D model cannot capture the real nature of things, which are 3-dimensional. An example is the value of the static capacitance C_0 , which is dependent on the aperture length, and so on the third dimension. Moreover, there are a lot of geometrical parameters involved in the design of a resonator which need to be optimized. Therefore, a more complete 3D model has been developed for the three topologies, and is shown in Fig. 2.21 for the LFE case, taken as example. Anyway, the other models are analogous, and the optimization procedure to be followed is the same. As it can be observed, the model does not only include the resonator, but also part of the substrate on which it is fabricated. In particular, as can be observed in Fig. 2.21, it is divided in two regions. The inner region is simply the substrate surrounding the investigated device, while the outer one consists of a Perfectly Matched Layer (PML). The PML is an artificial domain such that any

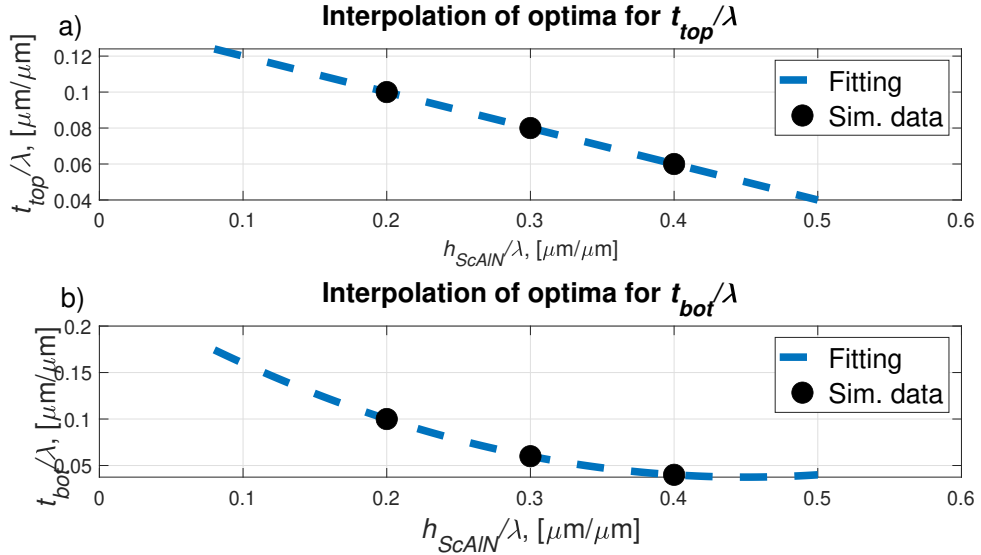


Figure 2.19: Optimal t_{top} (a) and t_{bot} (b) values to maximize the k_t^2 . The black dots are the points taken from Fig. 2.18a-c, while the dashed line represents the quadratically fitted function.

wave impinging on it from a non-PML domain is absorbed and not reflected. In this way, all the energy that leaks from the resonator through the anchors is lost in the PML and no reflection is expected. A CLMR consists a suspended piezoelectric plate able to vibrate and its clamping points are the anchors. The PML represents an improvement of a model made by simply applying a fixed constrain on the extremes of the anchors. As in the 2D case, in order to suppress edge effects, PBC have been applied to both the Electrostatics and Solid Mechanics modules.

The 3D model has been used in order to find the best values and the impact of the following quantities:

1. Anchor length L_{anc} .
2. Anchor width W_{anc} .
3. Bus length L_{bus} , i.e. the length of the bus of the IDTs, which routes the electrical signal to the various electrodes.
4. Gap length L_{gap} , which is the distance between the bus and the active region. The active region is where the electrodes are interdigitated.
5. IDT length L_{IDT} . The sum of L_{gap} and L_{IDT} corresponds to the electrode length L_e .

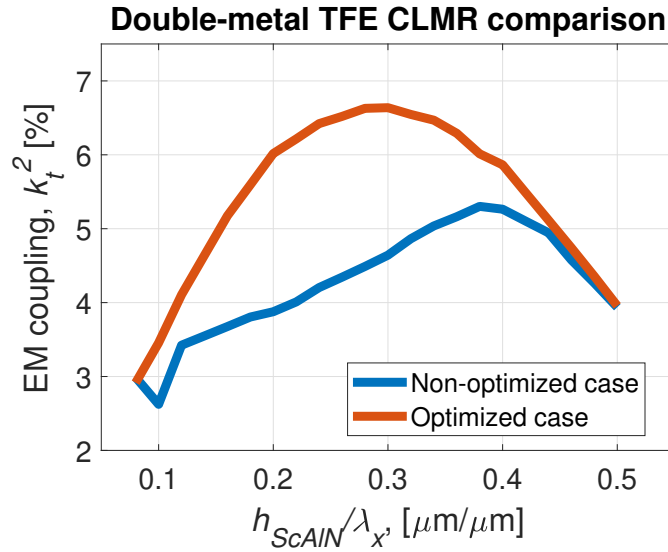


Figure 2.20: Comparison of two k_t^2 vs. h_{ScAlN}/λ_x' curves for two TFE CLMR with Al on top and Mo on bottom. The non-optimized case has $t_{top} = t_{bot} = 0.02\lambda_x$, while the optimized one has them following the fitting functions of Fig. 2.19a-b. The EM coupling increase is clearly visible.

In order to study the relationship between k_t^2 , Q , f_{res} and the geometrical parameters, first of all the latter have been written as function of λ_x . Secondly, they have been varied to see the impact on the aforementioned quantities. A λ_x of $8 \mu\text{m}$ has been chosen. Since the 3D analysis is done in order to optimize the resonators of the experimental plan, its doping conditions and electrode material, i.e. ScAlN at 30% and Al, respectively, have been used. They refer to the experimental plan on a $0.5 \mu\text{m}$ thick ScAlN wafer described in Sect. 2.7. This does not impact the generality of the study, and the same dimensions obtained for this case can be (and have also been) applied to other CLMR topologies, other electrode materials and Sc-doping levels.

The first thing to make sure was the agreement of the 2D and 3D models. Fig. 2.23 shows the comparison between the resonance curve for two simulated CLMRs, one in two and the other in three dimensions.

Concerning the IDT length, it has been swept from 2 to $12 \lambda_x$ and its relation to k_t^2 and Q have been studied. The quality factor is inversely proportional to the motional resistance R_m . That quantity has been extracted from the resonance curves as the reciprocal of the real part of Y_{11} at the resonant frequency, i.e. the frequency at which the motional capacitance and inductance cancel out each other's

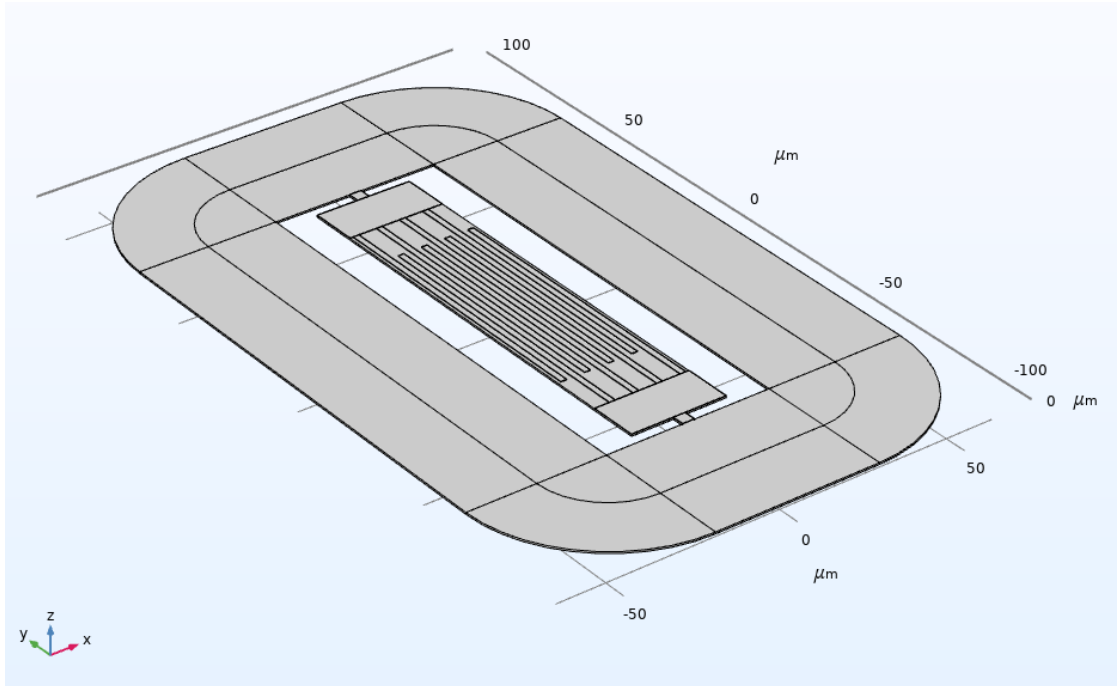


Figure 2.21: 3D COMSOL® model of a LFE CLMR, including the substrate and the PML.

effect on the admittance. Fig. 2.24a shows the k_t^2 and the R_m as function of the IDT length. As can be observed, longer the IDT, lower the resistance. The EM coupling coefficient has an oscillatory behaviour, probably due to the shifting of spurious

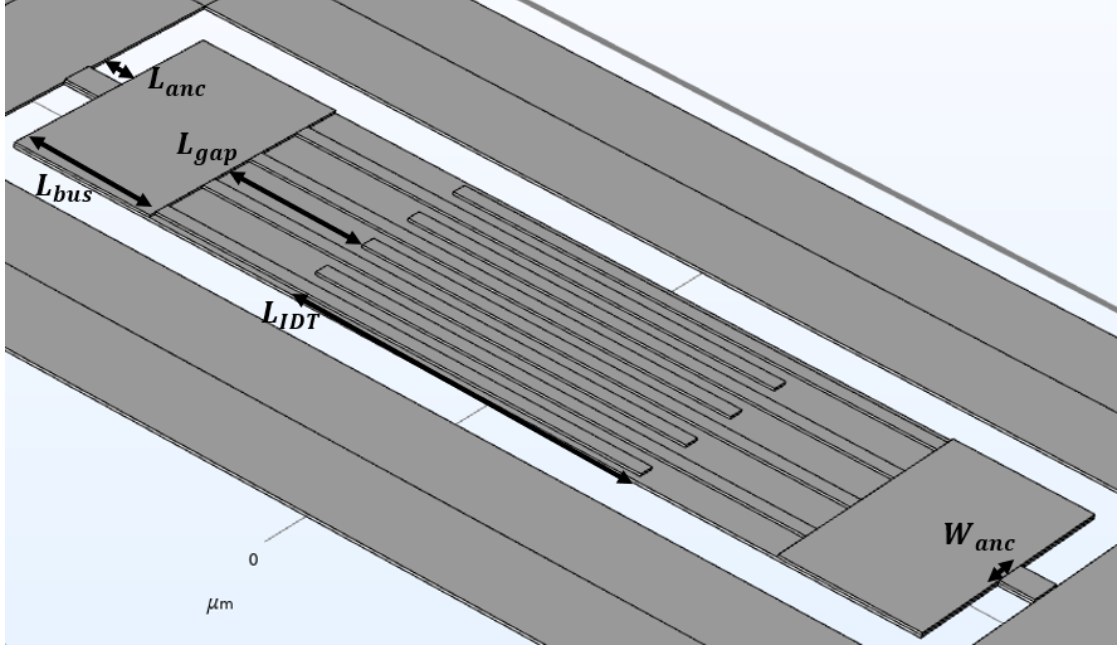


Figure 2.22: Closer look at the 3D model of the LFE CLMR. The relevant dimensions are shown.

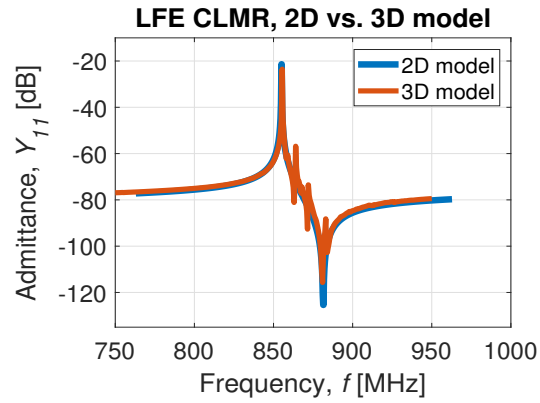


Figure 2.23: Comparison of the resonant curve for the CLM for the 2D and 3D model. In order to better compare the responses, the C_0 of the first has been reduced to match the latter, and the frequency has been slightly increased. As it can be observed, the k_t^2 is the same.

modes inside the resonance, but shows an increasing trend with the IDT length. Nevertheless, the simulation does not take into account the electrical loading, which increases with the IDT longitudinal dimension.

In opposition to the active interdigitated part of the resonator, the gap and the bus together constitute the inactive region, i.e. the region not directly put in motion by the applied electric field. In [25], it is shown that the quality factor can be maximized by having the inactive region length equal to an odd multiple of $\lambda_x/4$. In this way, that portion of the resonator behaves like a $\lambda/4$ transformer, and changes the stress-free boundaries at the edges of the plate to fixed boundaries at the limits of the active region. The result is a minimization of the energy lost through the anchors, and therefore, a maximization of the Q . Nevertheless, there is still the need to understand the impact of a wider or narrower odd multiple of $\lambda_x/4$ inactive region. What has been observed is that, smaller the region, smaller is the impact of spurious resonances between the f_s and f_p of the CLM. This fact can be observed in Fig. 2.24b. In the case of $L_{inactive} = L_{gap} + L_{bus} = \lambda_x/4$, the k_t^2 , i.e. the distance in frequency between f_s and f_p seems lower. That is an apparent effect. In fact, in the other cases, the anti-resonance of the CLM is pushed to higher values due to the presence of the spurious modes, but the real EM coupling

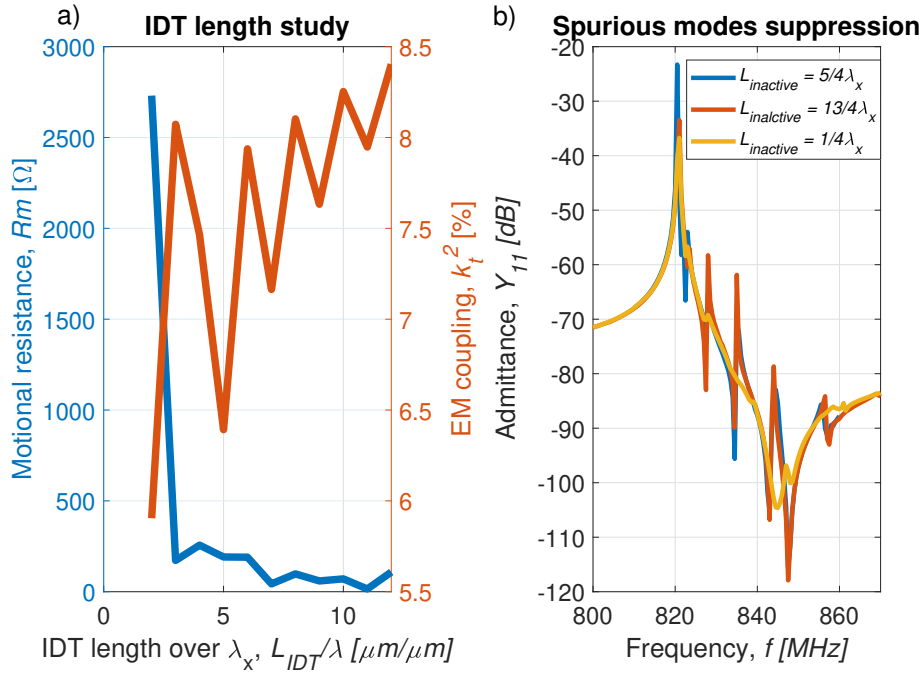


Figure 2.24: a) Behaviour of the motional resistance R_m (left) and of the k_t^2 (right) vs. the IDT length and b) showcase of the suppression of the spurious modes between f_s and f_p of the CLM due to the reduction of the inactive region length.

coefficient is not higher.

Concerning the anchors, in [26] an equation relating the quality factor to their geometrical dimensions is derived:

$$Q_{anc} = \frac{2\pi(1 - \nu^2)^2 L}{\nu^2 [W_{anc} + \frac{\lambda_x}{2\pi} \sin(\frac{2\pi W_{anc}}{\lambda_x})]} \quad (2.21)$$

where ν is the Poisson's ratio of (Sc)AlN in the plane of the film and L is the resonator length. The first thing to notice is that the anchor length does not appear in the equation, therefore it does not impact the Q . Secondly, it can be straightforwardly noticed that the wider the anchors, the lower the Q . Therefore, the fully-anchored resonator configuration, i.e. when $W_{anc} = W_{res}$, proves to be worse than the one with one or multiple thinner anchors. Moreover, a reduction of the k_t^2 was observed in the first case. Concerning the anchor length, it has impact on the resonant frequency, making the suspended plate more or less compliant according to the actual value.

In the next sections, two experimental plans are described in details, one for AlN as piezoelectric material (Sect. 2.6), and one using ScAlN (Sect. 2.7).

2.6 AlN experimental plan

As previously introduced, the first experimental design has been done on AlN. Unlike the design of the ScAlN plan, which was made on a wafer onto which the piezoelectric film had already been deposited, in this case the deposition has been done in-house, taking advantage of the EVATEC-clusterline tool for sputtering. Therefore, there has been the possibility of including a bottom electrode. The goal of this tape-out is to experimentally verify the curves of h/λ_x for the three structures of CLMR described in the previous sections. There is particular interest in the BE CLMR, which has never been experimentally demonstrated. Considering the quality of the electrode materials that could be sputtered in-house, Pt has been chosen as the one for both top and bottom electrodes. Their thicknesses have been set to 150 nm, while the one of the piezoelectric film has been designed to be 1 μm .

Due to the constraints on the film height and on the minimum feature size of the stepper used for the lithography (i.e. 500 nm), not the whole k_t^2 vs. h/λ_x curves of the simulations can be reproduced, but only a portion of them. Nevertheless, that is enough to experimentally validate the simulations. In particular, the verifications are aimed to observe:

1. TFE CLMRs, with the h/λ_x curve varying from 0.1 to 0.38
2. LFE CLMRs, with h going from $0.2\lambda_x$ to $0.38\lambda_x$

3. BE CLMRs, with the same variations of the LFE ones.

The targeted curves of k_t^2 vs. h/λ_x are shown in Fig. 2.25 for the three cases.

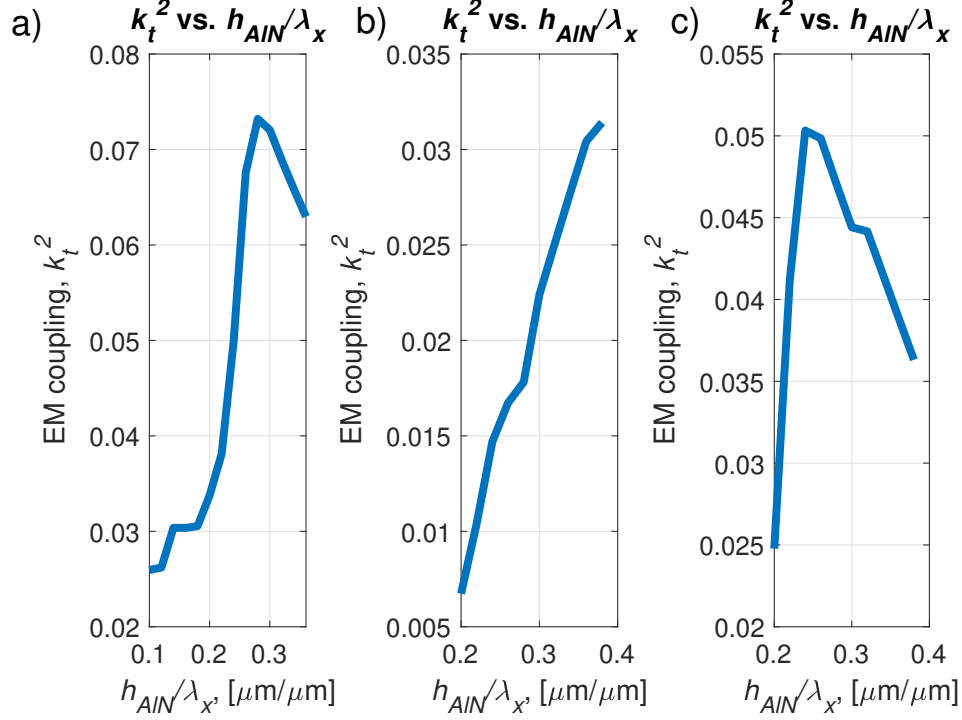


Figure 2.25: Expected curves of k_t^2 vs. h/λ_x for the CLMRs in AlN. In particular, in a) the TFE, in b) the LFE and in c) the BE CLMRs are shown.

Contrarily to the ScAlN tape-out, in which Al is employed as top electrode and allows for more freedom in the design due to its very low resistivity, in this case the high values of Pt considerably constrain it. In particular, to have good values of quality factors, the electrical loading effect has to be mitigated by the design. A detailed analysis of the calculation of the electrical loading in CLMRs is given in Appendix B. This is the reason for the high thickness of the electrodes: the higher the electrodes, the lower the resistance of the fingers per unit length. In order to have high Qs, the motional resistance has to be much higher compared to the parasitic one introduced by the electrodes resistivity. This is why the 50- Ω matching of the other tape-out cannot be performed: the motional resistance is directly proportional to the impedance matching, therefore it has to be increased. This also means that the static capacitance will be considerably reduced compared to the case of ScAlN. Given the parasitic capacitance induced by the VNA in the measurement phase (i.e. around 30 fF), the C_0 has to be as low as possible but still at least three times greater than that. This has led to the choice of 750- Ω

matching for the TFE and LFE CLMRs and 1 k Ω for the BE ones. The matching has been done exploiting the model described in Appendix A.

In addition, some ladder filters have been designed. In particular, five TFE CLMR filters and three BE ones. Those filters are of the first order, and were done in order to have preliminary results on filters done with this technology, to be refined and improved in future iterations. The S_{21} scattering parameter of the filters as function of the frequency is shown in Fig. 2.26a for the TFE topology, and in Fig. 2.26b for the BE one.

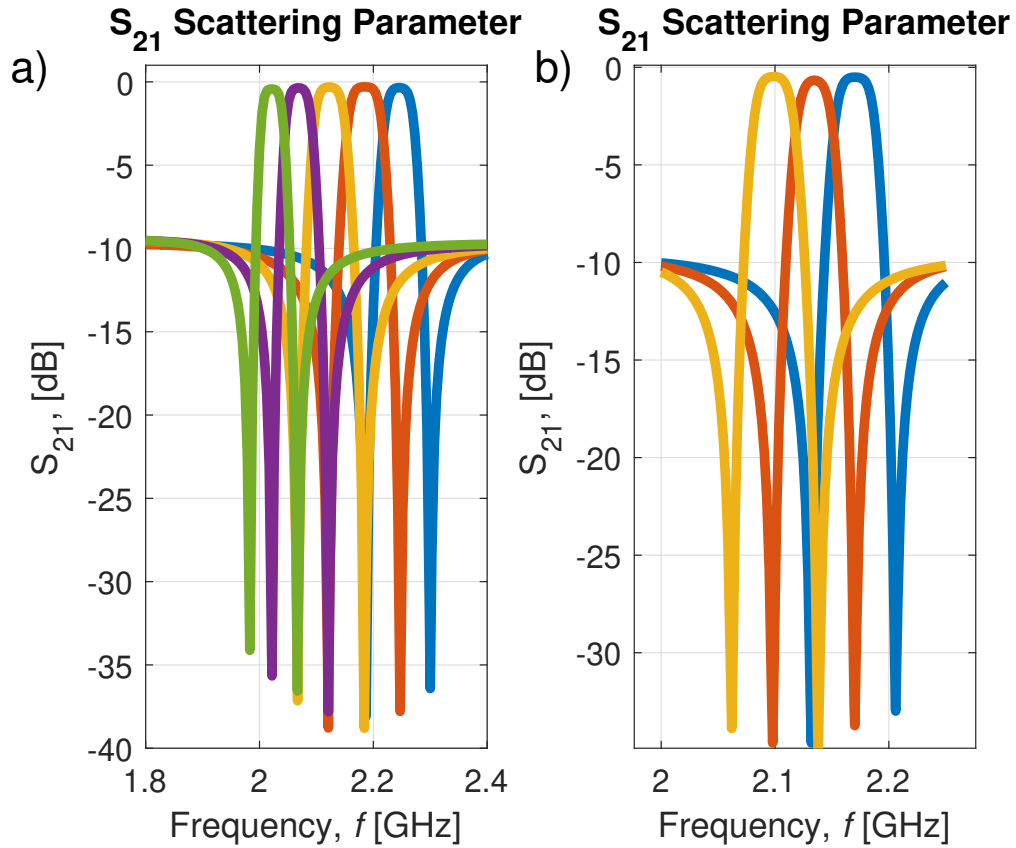


Figure 2.26: S_{21} scattering parameter vs. frequency for the filters made of a) TFE CLMRs and b) BE CLMRs.

In order to produce the lithographic masks for this tape-out, the library gdspsy of Python has been used. With it, codes defining the specific geometries have been created. After that, the layout has been saved as a GDSII file, i.e. the Geometric Design System file. The layout editor used to finalize the masks was Klayout. In a GDSII file, there are several layers identifying the different masks used for the fabrication. In this specific case, five masks have been introduced:

1. BOTTOM, i.e. the mask for the Pt bottom electrode, which is patterned in the case of TFE CLMRs and not patterned in the case of BE ones.
2. TOP, i.e. the mask used to make the top electrodes in Pt, together with the pads.
3. ETCH, which is the mask used to define the release pit of the suspended resonators.
4. VIAs, that is the mask used to make the vias to electrically connect the bottom electrode to the top in order to apply an electrical signal to it.
5. GOLD, i.e. the mask devoted to the deposition of gold on the pads, in order to reduce the electrical resistance of the platinum.

The five layers employed to fabricate a TFE CLMR are shown in Fig. 2.27, while the final resonator is depicted in Fig. 2.28. The cases of LFE and BE CLMR are similar. As it can be observed, there is the presence of three pads per port: the two external pads are the grounds, while the middle one is the signal. This configuration is called ground-signal-ground (GSG).

Finally, also the geometry of a first order TFE CLMR ladder filter is shown in Fig. 2.29.

2.7 ScAlN experimental plan

2.7.1 Resonator design

In order to experimentally verify some of the curves obtained in the previous sections and to show the potentialities of Sc-doping and CLMRs, also a tape-out plan in ScAlN has been prepared. The available wafer consisted in a 500 nm thick 30% Sc-doped AlN on high resistivity Silicon (Si). Therefore, only LFE structures could be fabricated. Being the film thickness very small, Super High Frequency (SHF) resonators are expected to be fabricated. All the resonators have been simulated through 2D FEM, and geometrical parameters such as the bus or anchor length, have been optimized using the 3D models. The chosen electrode material is Al. The device variations are done in order to verify:

1. The k_t^2 vs. h_{ScAlN}/λ_x curve, with the ratio ranging from 0.2 to 0.6, and so a λ_x ranging from $0.833\mu m$ to $2.5\mu m$. As it can be observed, a procedure opposed to the one of the simulation step was followed: instead of fixing the acoustic wavelength and varying the piezoelectric thickness, the first was fixed by the wafer and the latter used as a degree of freedom. Doing so, the resonant frequency is expected to change a lot throughout the whole range of variation.

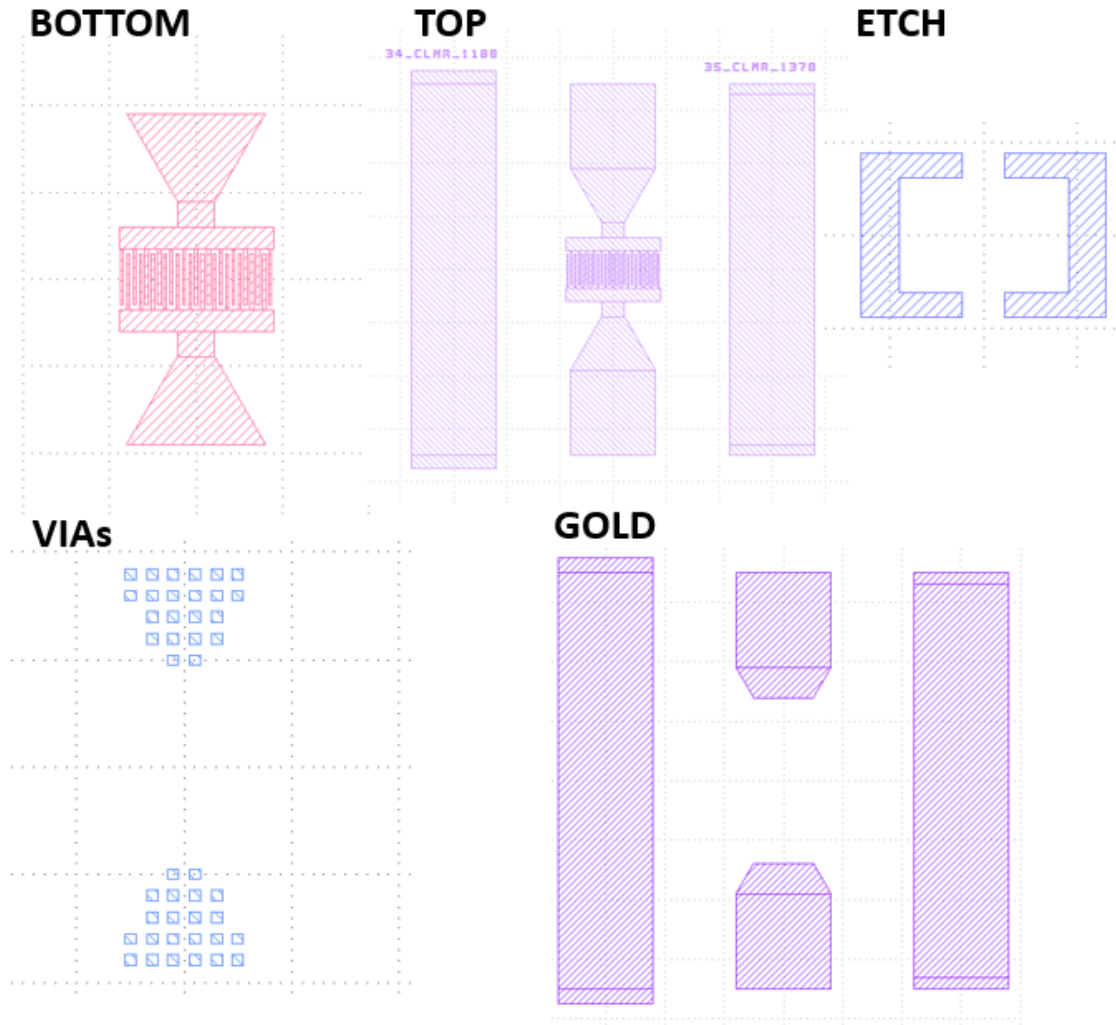


Figure 2.27: Showcase of the layers of which a TFE CLMR is composed. Each layer leads to the fabrication of a different lithographic mask.

In Fig. 2.30a, the expected k_t^2 vs. h_{ScAlN}/λ_x and f_{res} vs. h_{ScAlN}/λ_x curves are shown.

2. The k_t^2 vs. α curve, with the metallization ratio ranging from 0.35 to 0.65. The reason for the smaller variation with respect to the one in the theoretical analysis (going from 0.2 to 0.8) relies in the minimum feature size that can be fabricated through the available e-beam lithography tool, which is 200 nm. Being in this specific case 0.42 the h_{ScAlN}/λ_x ratio that theoretically allows to obtain the highest EM coupling, it gives a wavelength of 1.2 μm . Therefore, the pitch p will be equal to 0.6 μm . With an α of 0.35, the electrode width

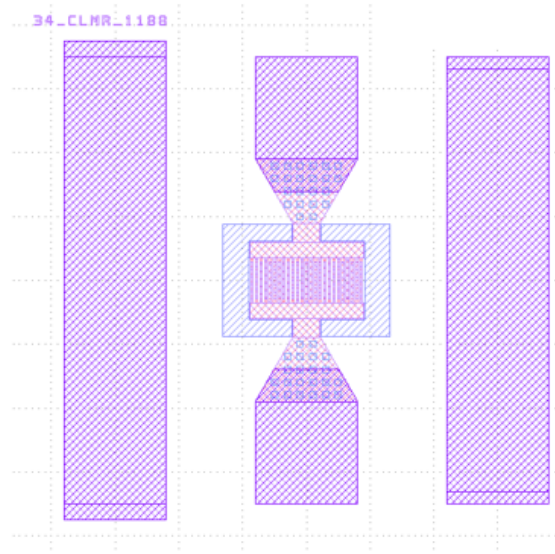


Figure 2.28: Example of a TFE CLMR as it appears on Klayout.

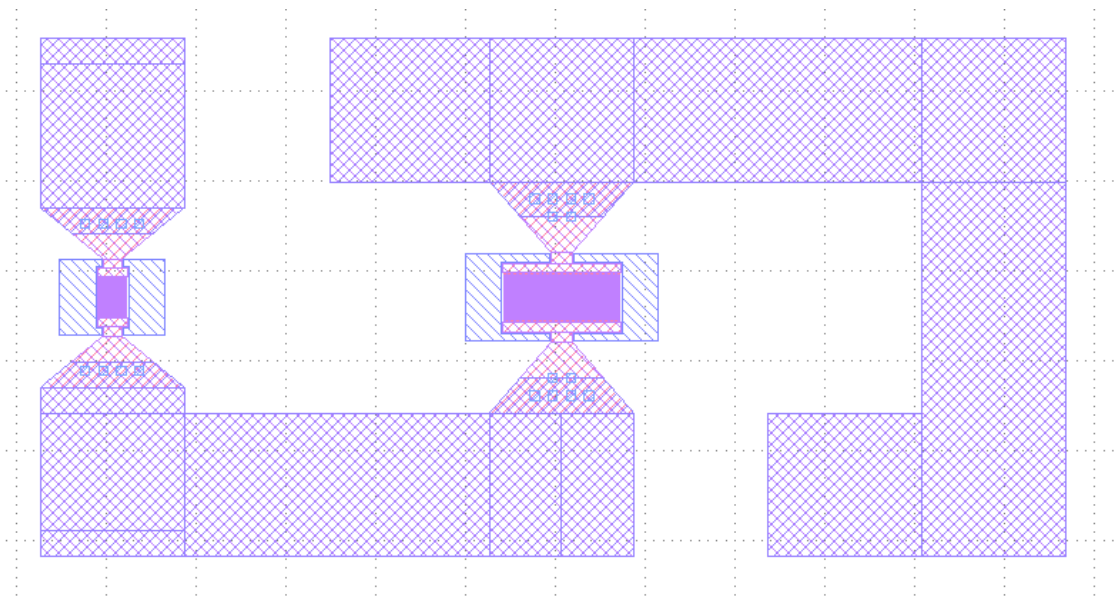


Figure 2.29: Example of a first order TFE CLMR filter as it appears on Klayout.

will be 210 nm, and that is the physical limit that can be reached. Vice versa, when α is equal to 0.65, it is the unmetallized region to be 210 nm wide. The curve that is aimed to be reproduced is shown in Fig. 2.30b.

3. The best N_p/L_e ratio, where N_p is the number of electrode pairs and L_e is the

electrode length. All the resonators in the tape-out have to be $50\text{-}\Omega$ matched in order to minimize the power reflection of the signal coming to the devices. This means that the static capacitance C_0 must be such that $C_0 = 1/(f_{res} 50\Omega)$. A more detailed analysis on the steps made to efficiently match the resonators can be found in Appendix A. Anyway, given a certain C_0 to be matched, the number of pairs and the electrodes length can be engineered to obtain the correct values. Nevertheless, different couples of N_p and L_e satisfy the constrain. In Fig. 2.24a it is shown the relationship between the motional resistance and the electrodes length. From it, higher Q are expected for longer electrodes. Nonetheless, longer electrodes provide higher electrical loading, and so a Q degradation. The variation has the goal to find the best trade-off between these two opposite effects, and so to answer to the question if it better to have longer but thinner or shorter but wider resonators.

Concerning the metal thickness, it is one for the whole set of resonators, therefore an optimal value has to be found, i.e. a value for which the k_t^2 is maximized (or is as high as possible) for a broad range of λ_x . The choice of Al lies in the fact that it has low resistivity, it is easily sputtered and the resulting thin films have good

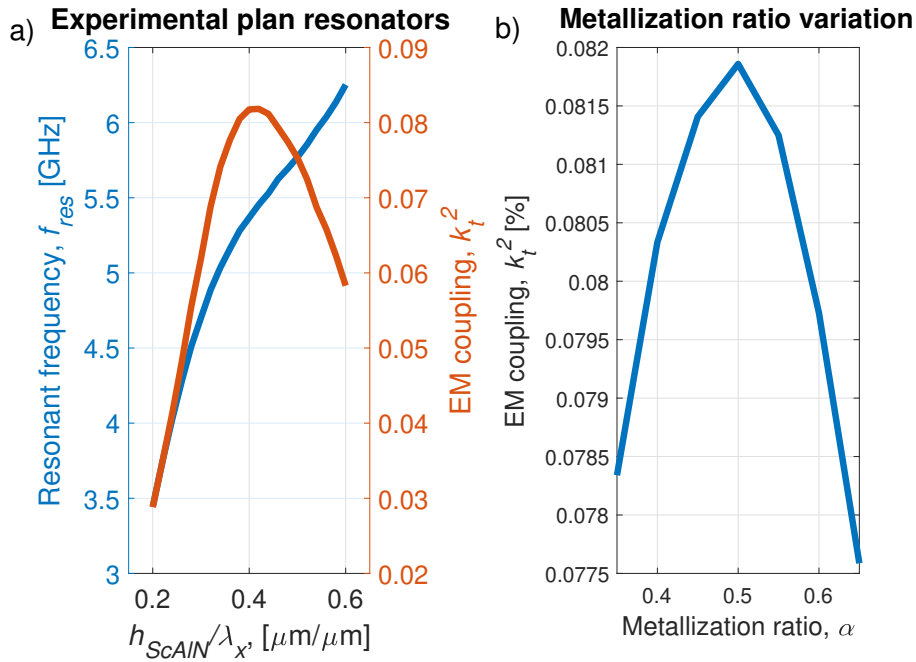


Figure 2.30: a) curves of f_{res} and k_t^2 vs. h_{ScAlN}/λ_x expected to reproduce with the resonators included in the tape-out, b) curve of metallization ratio α vs. h_{ScAlN}/λ_x expected from the tape-out.

quality. Using a procedure analogous to the one employed in the metal optimization step, different thicknesses are simulated for several h_{ScAlN}/λ_x ratios. The final value that gives the best results is $t_{IDT} = 0.3 \cdot h_{ScAlN} = 150$ nm.

2.7.2 Filter design

	1-s	1-p	2-s	2-p	3-s	3-p
k_t^2 [%]	7.5	7.2	8.1	7.5	8.2	8.1
λ_x [μm]	1.42	1.5	1.31	1.42	1.2	1.32
f_s [GHz]	5.12	4.99	5.28	5.12	5.44	5.27
	4-s	4-p	5-s	5-p	6-s	6-p
k_t^2 [%]	8	8.2	7.5	8	6.9	7.5
λ_x [μm]	1.09	1.21	1	1.1	0.93	1
f_s [GHz]	5.61	5.43	5.78	5.59	5.94	5.77

Table 2.5: List of k_t^2 , λ_x and f_s of each of the resonators of the bank of filters. S stands for series and p for parallel, i.e. the series and parallel resonator of the filter in Fig. 2.31.

The tape-out is also including a bank of ladder filters of the first order (Fig. 2.31). The main goal is, in this case, to fabricate a set of filters on the same substrate able to cover a wide band. As already mentioned, commercial state-of-the-art resonators (FBARs) lack in easy frequency tunability, therefore banks of filters must contain devices coming from different wafers. By combining the lithographic tunability of CLMRs and the outstanding k_t^2 boost given by Sc-doping, a band of 1 GHz from

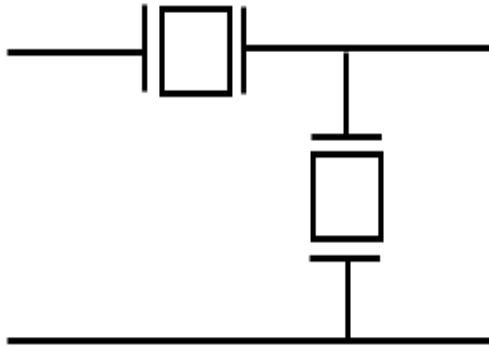


Figure 2.31: Schematic of a first order ladder filter made with resonators.

5 to 6 GHz can be covered by six first order ladder filters, each of them made by two LFE CLMR, all made on the same substrate. The resonators were simulated through 2D FEM with COMSOL®, while the filter performances were assessed both with ADS and MatLab. Fig. 2.32 shows the S_{21} scattering parameters of the above mentioned devices as function of the frequency. As it can be observed, an overall band of 1 GHz is covered. The resonators k_t^2 , f_{res} and λ_x are listed in Table 2.5. Concerning the out-of-band rejection ($S_{21out-band}$), as shown in the first chapter, it is function of the ratio of the static capacitances of the parallel (C_{02}) and series branch (C_{01}), respectively, and of the number of stages N . In this case, $N = 1$ since the device yield is low, and therefore adding more resonators increases the chance of malfunctioning of the filter. In order to have a decent rejection, C_{02} was designed to be four times C_{01} . This gives a theoretical $S_{21out-band}$ of -14 dB.

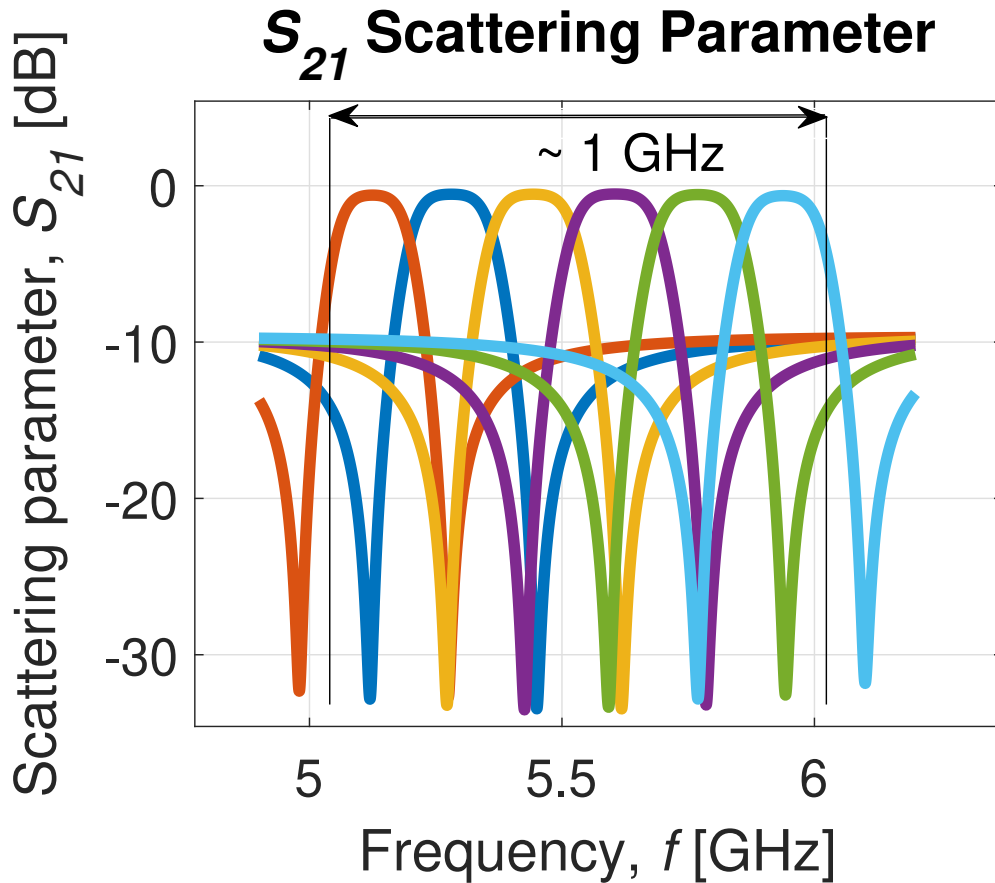


Figure 2.32: a) curves of f_{res} and k_t^2 vs. h_{ScAlN}/λ_x expected to reproduce with the resonators included in the tape-out, b) curve of metallization ratio α vs. h_{ScAlN}/λ_x expected from the tape-out.

From ADS, the obtained value is around -10 dB. The equivalent capacitance of the filter, i.e. $C_{eq} = \sqrt{C_{01} \cdot C_{02}}$ is 50- Ω matched. During the design step, a quality factor of 500 has been assumed for all the resonators. Although this assumption is sensible, it is not necessarily true. Nevertheless, the quality factor impacts the IL (which for $Q = 500$ is around -0.5 dB), not the FBW, so in the worst case in which the quality factor is lower than expected, the 1 GHz bandwidth will not be degraded.

Filters made with AlN CLMRs are already present in literature [27]. In particular, they show problems concerning ripples in the passband, reducing the fractional bandwidth. In [28], third order ladder filters are fabricated with AlN CLMRs, employing thick Pt electrodes and taking advantage of IDT apodization in order to suppress the spurious modes in the pass band. My goal is not to optimize the design of the filters, nor to replicate the already obtained results. In the present tape-out, CLMR ladder filters are made for the first time in ScAlN. Moreover, what is finally aimed is to show that extremely wide band bank of filters can be made on the same chip, with a really reduced fabrication complexity (two-masks process). The overall performances in terms of absence of spurious responses or losses are not a key-point in the analysis, which poses itself as a proof of concept.

As in the case of the previous tape-out, the design has been done using gdspy and Klayout. In this case, three lithographic masks will be used:

1. TOP, i.e. the mask used to make the pads.
2. EBEAM, i.e. the mask to make the fingers of the resonators, which require a resolution which is higher with respect to the one achievable with the stepper of the previous tapeout.
3. ETCH, which is the mask employed to define the release pit of the resonators.

Chapter 3

ScAlN ferroelectricity and FEM model of ferroelectrics

3.1 Ferroelectric ScAlN

It has been seen in Chapter 2 that Sc-doping of AlN thin films leads to a great improvement of piezoelectric MEMS resonator characteristics, greatly enhancing their electromechanical coupling. This chapter, on the other hand, will focus on another ScAlN interesting feature: its **ferroelectricity**. This peculiarity has been very recently demonstrated [15].

AlN and other III-V nitrides, such as InN and GaN, possess a wurzite-type structure with spontaneous polarization along their *c*-axis. This fact is responsible for their piezoelectricity and means that, inside the material, there exist two anti-parallel polarization directions, i.e. the N-polar and the metal-polar. Thus, the III-V nitrides also exhibit pyroelectricity, but not ferroelectricity, since their polarization direction cannot be switched with electric fields that are lower than their dielectric breakdown limit, i.e. the point at which they cease being insulators and conduct electricity. Nevertheless, the doping with Sc of pure AlN films lowers the electric field necessary to the polarization switching, leading the material to exhibiting ferroelectric properties. The reason can be found in the continuous distortion of the wurzite-type crystal structure of AlN towards a layered-hexagonal structure (the one of ScN) with increasing Sc-doping level [15]. Moreover, this particular feature is expected to be possibly extended to other III-V materials. Fitchner *et al.* were the first to experimentally demonstrate ScAlN ferroelectric hysteresis curves. They are reported in Fig. 3.1 for different Sc concentrations, together with the P vs. E curve for lead-zirconate-titanate (PZT 52/48), a very commonly employed ferroelectric material. What can be firstly observed, is the almost ideal square-like hysteresis, which results in a great piezoelectric linearity

for fields lower than the coercive ones. Additionally, in Fig. 3.1 it can be seen that the hysteresis curves are shown for ScAlN with Sc contents greater or equal than 27%. The reason, as already mentioned, is the progressive reduction of the coercive fields of the material films with increasing Sc-doping level, which leads the nitride to exhibit ferroelectric properties only for a Sc percentage greater than 22%. Before that, the coercive fields (E_c) are still higher than the dielectric breakdown limit. When the material becomes ferroelectric, it keeps having high E_c and remnant polarization (P_r) compared to other commonly utilized ferroelectric materials, such as PZT. What can also be observed, is that both E_c and P_r values decrease with increasing Sc-percentile content, the former in a linear manner, the latter in a non-linear one. In addition, it was demonstrated in [15] that by adjusting the mechanical stress of the film, the coercive field can be linearly tuned, giving a further degree of freedom in controlling its material properties.

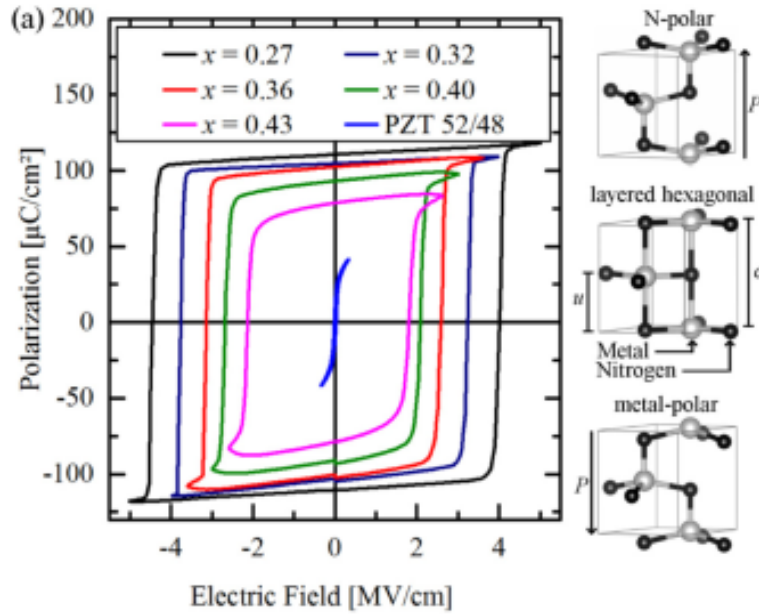


Figure 3.1: $Sc_xAl_{1-x}N$ hysteresis curves for Sc contents of 0.27, 0.3, 0.32, 0.36, 0.4 and 0.43. The curve of PZT 52/48 is also shown for comparison. On the right, the atomic structure of the nitride is shown for the unpolarized and polarized material. The figure is from [15].

3.2 Ferroelectric reconfigurable resonators

As introduced in Section 1.1, MEMS resonators constitute the building blocks of the commercial RF filters used in the RF front-end of everyday life products, such as smartphones, tablets and personal computers. Inside these devices, a great number of band-pass filters are required to cover the whole dedicated frequency band, and switches are used to select the filter of interest. In particular, in today's cell phones, their number is around the 40 units, with the expectation that this number will exceed 100 soon [29]. This fact poses great challenges concerning the area occupied, the cost and the power consumption associated to these growing RF front-ends.

An interesting strategy to overcome this problem may be the employment of filters which mix the switching capability to their filtering functions. In this way, the combination of a filter and a switchplexer would be replaced by a more compact unit. In Fig. 3.2a, a simplified block diagram of a current commercial RF front-end is shown. In Fig. 3.2b, on the other hand, an example of a front-end which exploits reconfigurable filters is shown. It is clearly visible that in the second case, the amount of electronics is considerably reduced.

The basic building blocks of the aforementioned switchable filters are switchable MEMS resonators, with the capability of being turned on and off by an externally applied DC bias. In particular, there are two ways of fabricating switchable resonators [29]:

1. Using the capacitive transduction mechanism
2. Exploiting ferroelectricity and its intrinsic two-state switchable nature

The formers allow to obtain high values of quality factor but come with very large motional resistances. This fact poses problems when it comes to integrate them in 50- Ω -matched RF front-ends. Ferroelectric resonators, on the other hand, exhibit high k_t^2 and quality factors and are the preferred choice in such RF filters.

In [29], intrinsically switchable filters are demonstrated for the case of Barium Strontium Titanate (BST). In Fig. 3.3a, an example of the frequency response of a resonator in the on and off states is given, whereas in Fig. 3.3b, the S_{21} parameter of a switchable filter in the same cases is shown. For what can be observed, the switching process provides the desired reconfigurability of the devices.

Although the incredibly promising feature of the above mentioned resonators and filters, the performance of BST are very poor compared to the ones of AlN, and especially to the ones of ScAlN. Moreover, its fabrication technology is far less mature than the one of (Sc)AlN. Therefore, building reconfigurable ScAlN MEMS resonators could revolutionize the RF front-ends of commercial products.

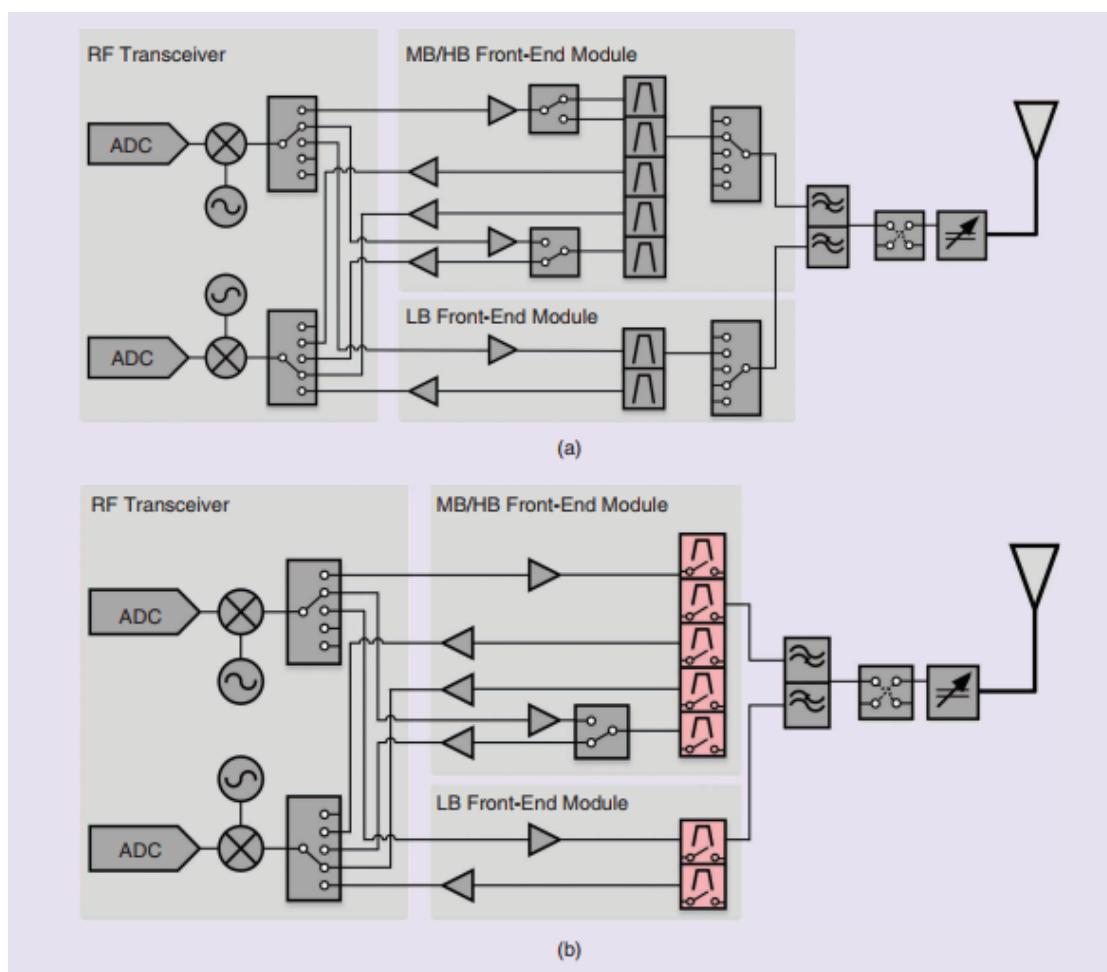


Figure 3.2: Simplified building block schematic of the RF front-end of a commercial wireless device (a) and of an ideal device in which all the filters have been replaced by reconfigurable ones (b). The picture is from [29]

3.3 Experimental demonstration of ScAlN thin film ferroelectricity

ScAlN ferroelectricity has been demonstrated experimentally in [15]. Nevertheless, in order to study its mechanical, dielectric, piezoelectric and ferroelectric characteristics, measurements on several samples at different Sc concentrations and different film thicknesses have to be performed. All the films have been deposited using the tool from the swiss company Evatec named EVATEC-clusterline. This sputtering tool, whose structure is depicted in Fig. 3.4, is heavily employed in MEMS resonator companies (e.g. Broadcom) and allows to automatically deposit

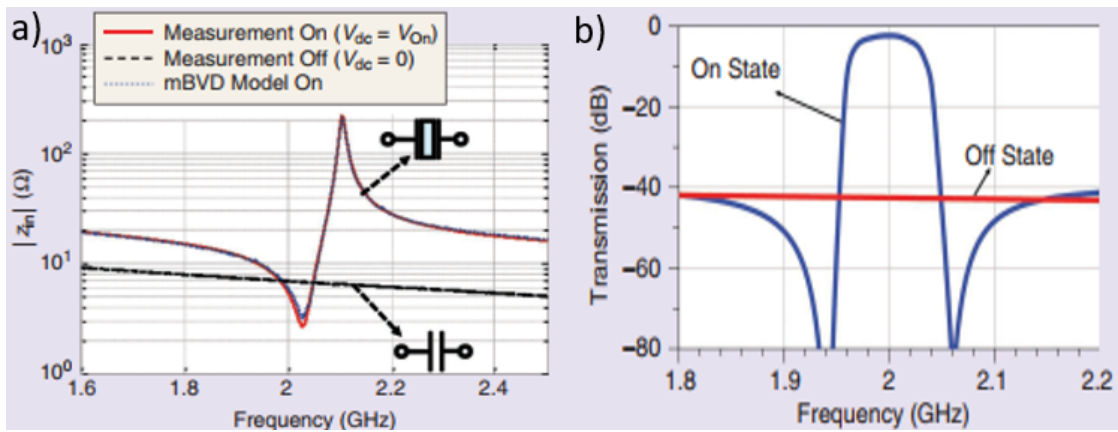


Figure 3.3: a) Impedance curve of a ferroelectric resonator in the on stage (in red) and in the off stage (in black). The modified BVD (m-BVD) fitting is also present, b) S_{21} parameter of a switchable filter in the on (in blue) and off (in red) state. The figures are from [29].

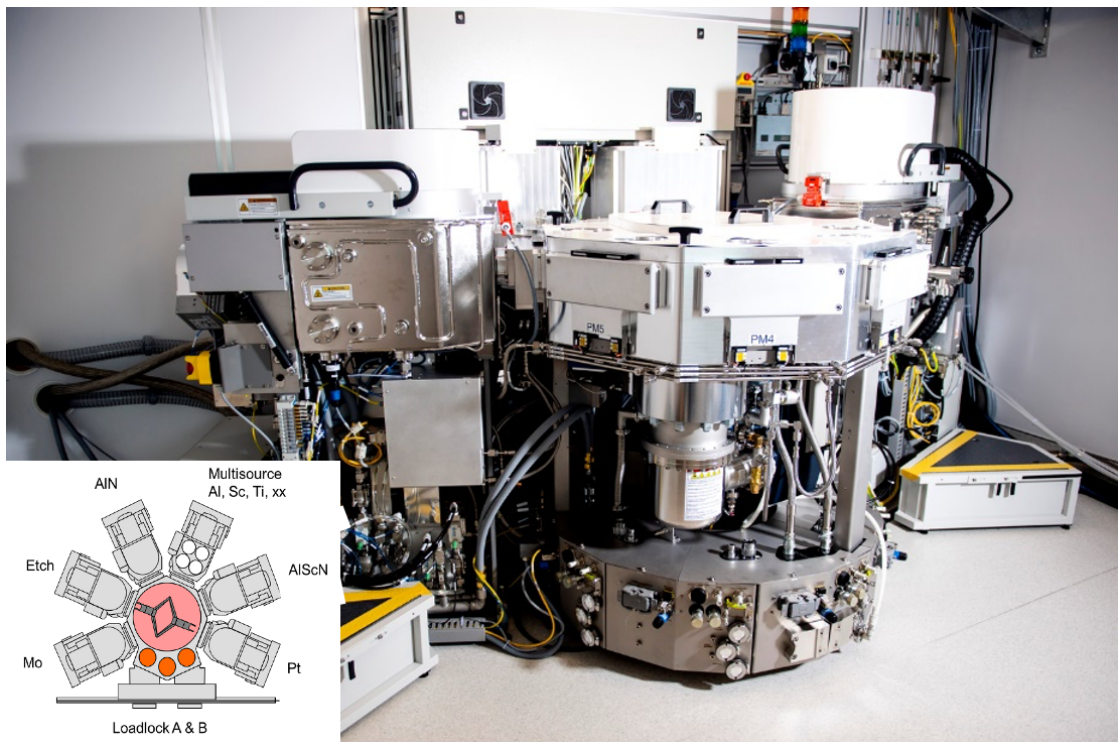


Figure 3.4: Picture of the Evatec-Clusterline industrial sputtering tool. A schematic of the tool is depicted in the inset.

on multiple wafers: it has two deposition chambers, the former with 24 8" wafer holders and the latter with 13 8" holders, onto which some carriers have been placed in order to deposit also on 4" wafers. This tool allows to sputter both metals and ceramic materials, even in a sequence and without breaking the vacuum. Concerning the alloy deposition, i.e. the one of ScAlN, there is the possibility of sputtering from a ScAl alloy target or to exploit reactive sputtering using two targets, one of Sc and the other one of Al. In the in-house cleanroom, a recipe to deposit high quality ScAlN thin films has been developed, allowing for extremely high control of the films characteristics such as the Sc-doping level, crystallinity, stress, thickness and surface roughness. All these specs can be tuned according to deposition parameters such as the deposition time and temperature, the sputtering power, the frequency or the composition of the carrier gas. In particular, commonly employed carriers are nitrogen (N_2) and argon (Ar), and it has been seen that increasing the N/Ar ratio reduces the deposition rate and improves the films crystallinity. This last parameter can be assessed using the Full Width Half Maximum (FWHM) curve, also named rocking curve. A film is considered high quality when its rocking curve is below 2° , and when the carrier gas is constituted only of nitrogen, its value is minimized. Moreover, it has been observed that, the more the nitrogen is present with respect to argon, the more the anomalous grain formation on the films surface is suppressed. This phenomenon can be clearly observed in Fig. 3.5, depicting Atomic Force Microscope (AFM) images of the films surface for different nitrogen/argon ratios. Another way to reduce the rocking curve of the films is to deposit ScAlN onto a metallic seed layer. In particular, it has been seen that the rocking curve of the sputtered piezoelectric film follows the one of the below-deposited metal. Good results have been obtained with Pt, especially for thick ($>300\text{nm}$) films of the metal. In Fig. 3.6, Transmission Electron Microscope (TEM) images of the materials stack onto the silicon wafer are shown, with also a zoom-in into the interfaces between the bottom Pt and ScAlN and the one with the top. It is interesting to notice (and it is very clear from the TEM image) that at the top interface there is a thin oxide layer of about 5-6 nm. This oxide has been identified as one of the possible causes of the asymmetry in the leakage current of the capacitor described in the following. This oxide is a native one, and is made of Al, Sc and oxygen. The reason for its appearance on the top is that the top electrodes were patterned using the lift-off process, and therefore the top surface of the ferroelectric film has been exposed to air. In order to suppress the native oxide formation, the alternative could be to deposit the top electrode inside the Evatec-clusterline tool without breaking the vacuum, and pattern it via wet or dry etch.

In order to characterize the material, test structures have been developed in the form of vertical and lateral field (TFE and LFE, respectively) capacitors. As in Chapter 2, the lithographic masks employed for the structures patterning have been

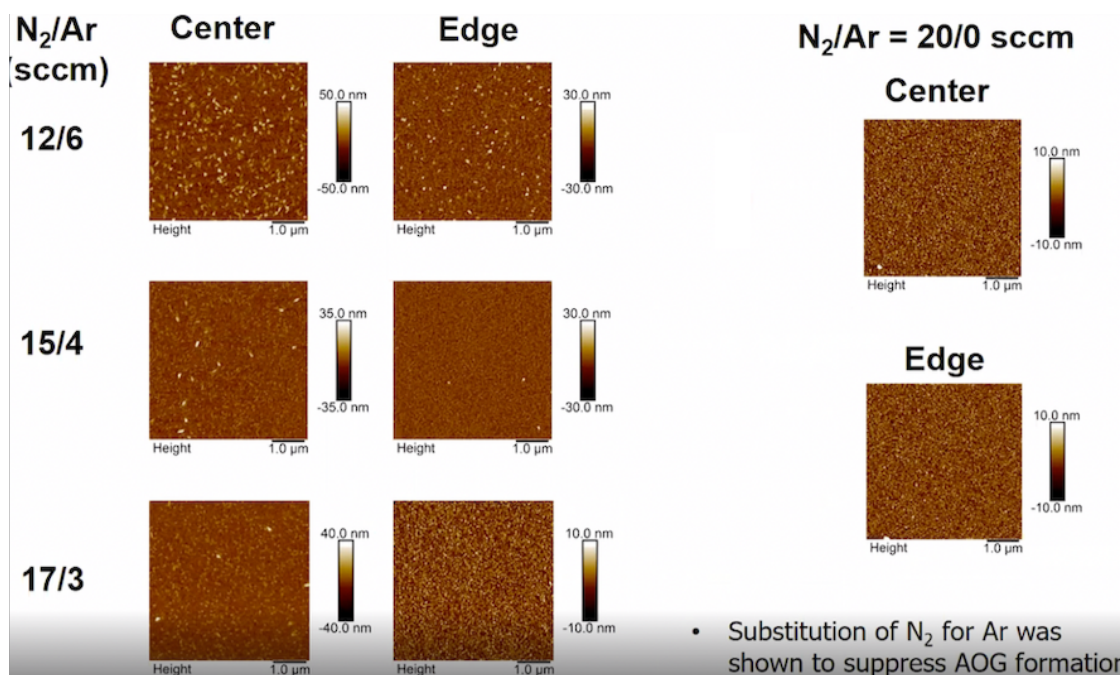


Figure 3.5: Atomic Force Microscope (AFM) images of the surface of ScAlN thin films for different nitrogen/argon ratio, both at the center and at the edge of the wafer. It can be observed that increasing the ratio, the presence of anomalous grains is considerably reduced. The best case is shown on the left, when the carrier gas is constituted only by nitrogen. This picture was taken from an IFCS presentation.

developed using the Python library GDSPy and finalized exploiting the software Klayout. To make the structures, only two masks were required, namely the **TOP**, to make the top electrode of the capacitors and the **VIAs**, used to make the electrical connections to the Pt bottom electrode, which has been left covering the whole wafer. The GDSII file of the designed chip is shown in Fig. 3.7, while in Fig. 3.8 there is a picture of the final chips patterned on the film. As it can be observed, different copies of the same geometry have been placed onto the wafer. The top metal has been chosen to be Pt or Al, and the structures have been made using the lift-off process. The vias have been opened with chemical etching by employing hot phosphoric acid. In the images, test structures for the metal resistivity and the etching resolution can also be seen.

The tests have been performed using the Aixacct AixDBLI, a tool designed for piezoelectric and ferroelectric characterization of thin films, and which is described in the following Section.

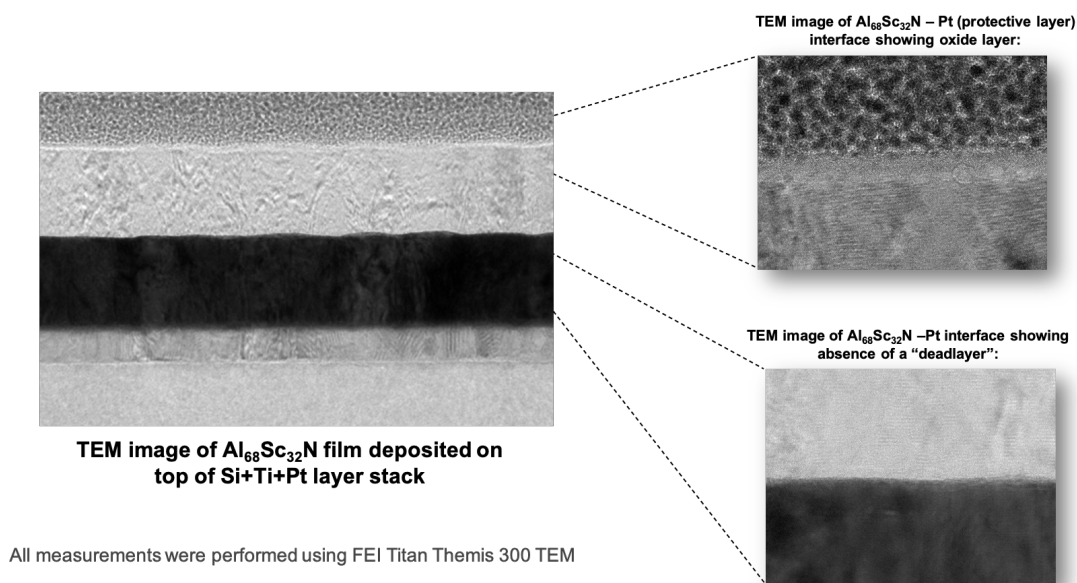


Figure 3.6: Transmission Electron Microscope (TEM) image of the material stack onto the silicon wafer showing, from bottom to top, the titanium adhesion layer, the Pt bottom electrode, the ScAlN film and then a protective layer used in the TEM imaging process. The insets show the ferroelectric film at the top and bottom interfaces. On the top one, a 5-6 nm thick native oxide is clearly visible.

3.3.1 AixDBLI tool description

The AixDBLI tool is meant for electric, piezoelectric and ferroelectric characterization of thin films. The acronym DBLI stands for Double-Beam Laser Interferometer, which is what is employed to make the piezoelectric characterization and the piezoelectric coefficients extraction. The tool is shown in Fig. 3.9, into which two modules can be seen. The one on the right consists in the computer onto which the AixPplorer and AixDBLI softwares are installed and which provides the Graphic User Interface (GUI) to do the measurements. Moreover, there are a high-voltage amplifier, capable of delivering up to 400 V of input voltage and 100 mA of current, and the system to suppress vibration. On the left, there is the DBLI module, including optical setup and the chuck onto which wafers or single chips can be placed and characterized. The pads on the chip are probed with tungsten sharp tips. The optical component scheme is shown in Fig. 3.10.

Let's now describe how it works. The beam is firstly generated employing a He-Ne laser and passes through a diaphragm and a shutter before being reflected into the main optical path by the mirrors M1 and M2. Then, it is polarized by the $\lambda/2$ plate P1 and approaches the first polarizing beam splitter (PBS1),

which divides it into the measurement and the reference beam. A PBS reflects the incoming light with Y-polarization and transmits the one with X-polarization, where X and Y are the directions of the cartesian axis. The measurement beam is the one that is transmitted, and has the longest path compared to the reference one, therefore is subjected to more losses. This beam passes through the $\lambda/4$ plate P2, is reflected by the mirror M3 and focused on the top surface of the wafer by the lens L1. Then is reflected and comes back, passing again through the P2 plate and having therefore the polarization changed from the X-direction to the Y one. In this way, it is reflected by PBS1 and by PBS2, reaching the $\lambda/4$ plate P3, the mirror M4 and the lens L2, which focuses it on the bottom surface of the wafer. In

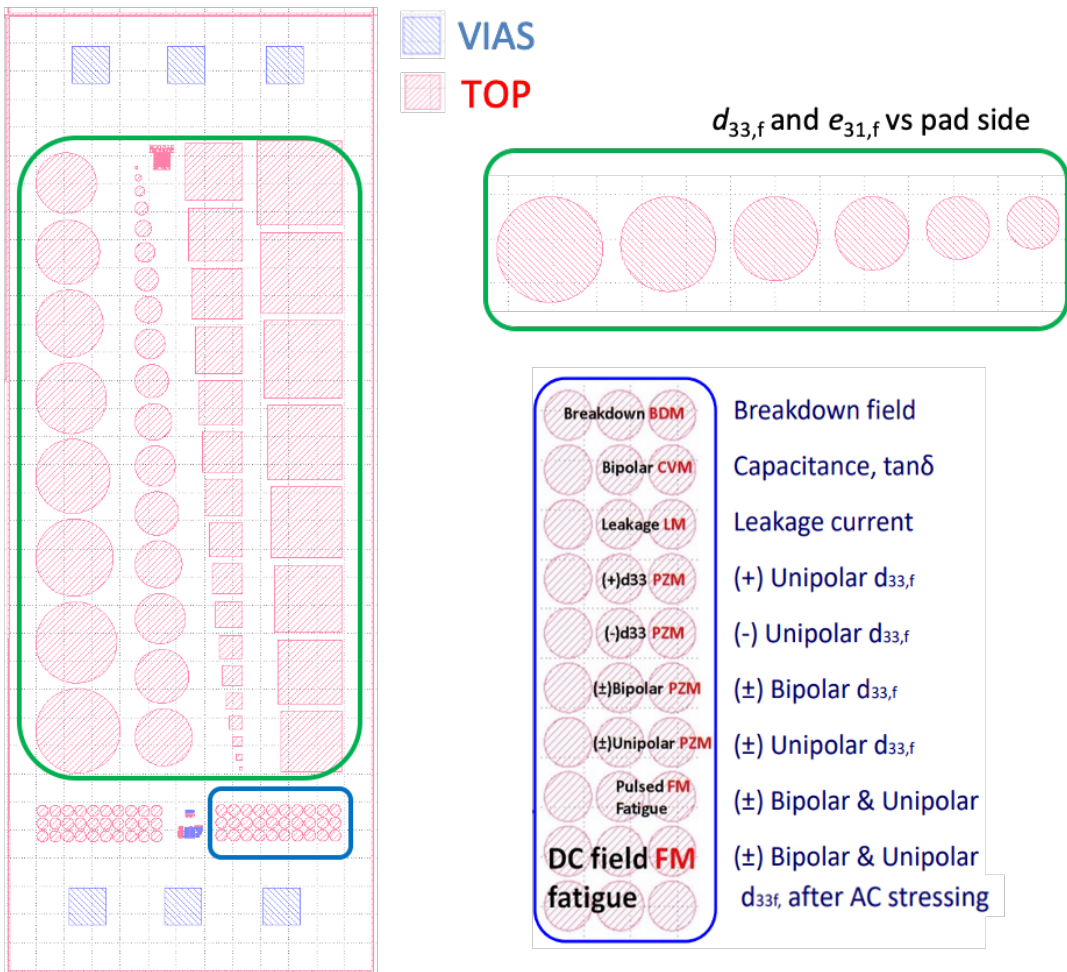


Figure 3.7: Picture of the lithographic mask to define the ferroelectric capacitors on the ScAlN film, as it appears on the GDSII file. On the mask, the different pads are highlighted with the parameters that can be extracted by measuring them.

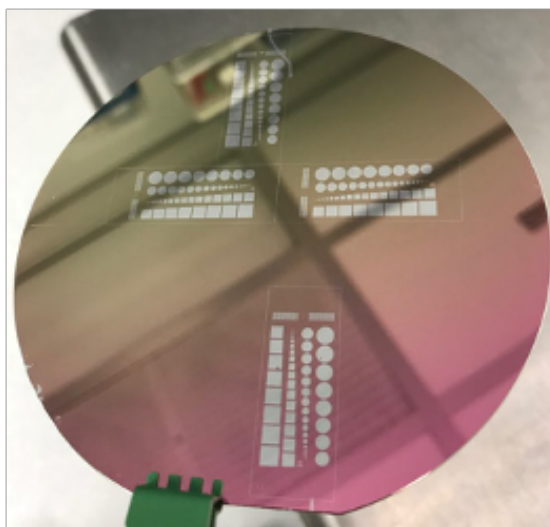


Figure 3.8: Picture of a the wafer with 250 nm of 30% ScAlN onto which four chips have been patterned.

order to be able to employ the DBLI, the wafer has thus to be double-polished. After the reflection on the bottom surface, the beam is polarized again passing through P3 and now is transmitted through PBS2, reaching the beam splitter (BS) BS3. There, half of the light is transmitted and half reflected and sent to the photodetector. Concerning the reference beam, it is reflected upward by PBS1, passes through the $\lambda/4$ plate P4, is reflected by the piezo mirror M7 and passes again through P4, changing the polarization from the Y to the X direction. In this way, the beam is transmitted through PBS1 and PBS2, is reflected by the mirrors M5 and M6 and goes to BS3, which splits it. The transmitted part is sent upward to the photodetector, where it interferes with the measurement beam. The strain of the measured sample is directly quantified by the variations in the center of the interference pattern.

Concerning the kinds of possible measurements that can be performed by the tool, there are all the types to fully characterize a ferroelectric thin film. In the following, the ones that have mainly been used in the current thesis work are briefly described.

1. **DHM:** the Dynamic Hysteresis Measurement allows to obtain the Polarization vs. Voltage curve, also named hysteresis curve in ferroelectric materials. The curve, together with the input signal sent to the pads is shown in Fig. 3.11. Concerning the input signal, it consists of different triangular wave pulses, even though different input signal can be configured to be applied. The first pulse (in blue) is the pre-polarizing one, with the aim of giving a specific



Figure 3.9: Picture of the AixDBLI tool. On the right, the case, amplifier and system to suppress vibrations. The DBLI is on the left, together with the chuck, onto which wafers or single chips are placed to be tested.

polarization to the ferroelectric capacitor. No output is recorded at this point. Then, the first measurement pulse is generated. As it can be observed, after the pre-polarizing pulse, the polarization state is the negative one, therefore it is switched by the measurement signal, which gives the green curve on the right as output. Then, a second pre-polarizing pulse is generated, in order to counter-switch the capacitor. The second measurement wave consists of the opposite of the first one, switching the capacitor firstly in the negative polarization. The output is the light blue curve. As it can be observed, both the red and the light blue curves are not continuous, having a gap between the beginning and the end. The red curve combines the two, giving a closed loop as final output. The important values like the maximum polarization, the remnant ones and the coercive voltages are shown in the figure.

2. **PZM:** the PieZo Measurement takes advantage of the DBLI system to record

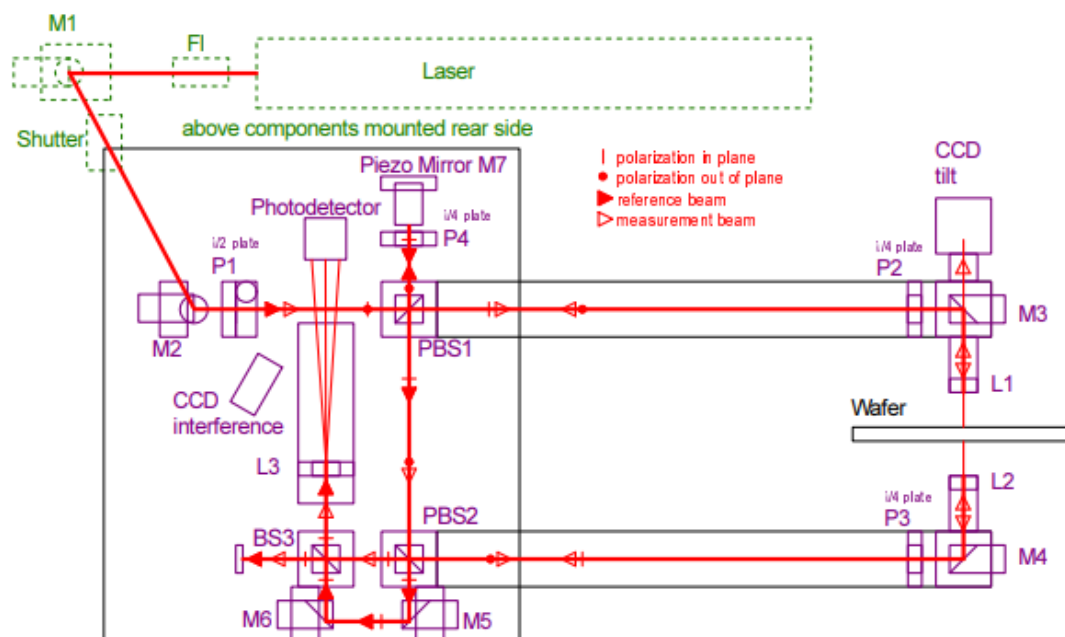


Figure 3.10: Schematic of the optical setup of the AixDBLI characterization tool.

the Strain vs. Voltage curve, also named butterfly curve. As introduced in the previous Section, the displacement of the film is detected by the variations in the interference fringes on the photodetector. The resolution of the system is very high, allowing to measure displacements of the order of $10^{-2} - 10^{-3} \text{ \AA}$. At the same time, it provides the electrical P vs. V curve as in the case of the DHM. In order to measure the butterfly curve, the laser spot has to be placed into the middle of the pad, and the probe has to be put on its side, in order not to scatter the beams light. An example of the probing and laser placing on a small circle capacitor with $200 \mu\text{m}$ diameter is shown in Fig. 3.12.

3. **PM:** the Pulse Measurement is used to record the samples current in response to a certain number and pattern of excitation pulses. In this framework, the most famous and commonly used configuration is called PUND (Polarization Up-Polarization Down). This measurement type is mainly used for ferroelectric memories characterization. The PUND input signal and output curves are shown in Fig. 3.13. As it can be observed, in the input signal there is firstly a write pulse which polarizes the capacitor in the negative state, and which is not recorded. Then, after a relaxation time which is typically 1 second, the first rectangular (or triangular) pulse flips the polarization, bringing it from the relaxed negative remnant polarization to the maximum positive

one up to the remnant positive polarization. The second read pulse is sent after the relaxation time, which brings the remnant polarization to a lower value (relaxed remnant polarization). Being the polarization still positive, no switching occurs, and the only current that is measured is the leakage one of the capacitor. This method, in fact, is useful to characterize the losses of the ferroelectric capacitor. After another relaxation time, the same two pulses are applied but in the negative direction, in order to obtain the values for the negative side of the loop.

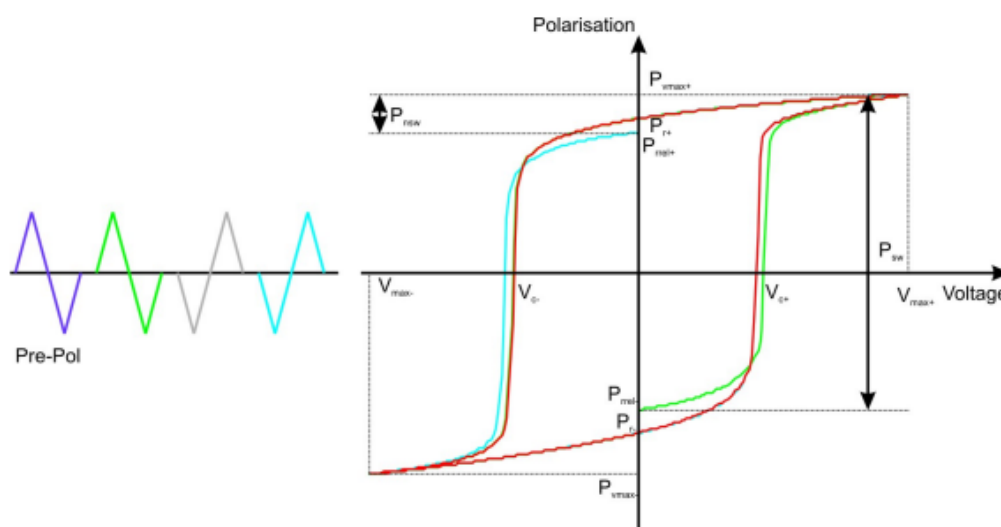


Figure 3.11: Showcase of a DHM measurement with, on the left, the input signal, and on the right the hysteresis curve. The picture is from the AixPplorer manual.

3.3.2 Measured samples and results

The AixDBLI tool has been used to perform measurements on a huge amount of samples, constituted by the chip shown in Fig. 3.7. Even though the pad layout was the same, different thicknesses have been taken into consideration, namely 500, 250, 100, 50 and 20 nm, and for each thickness, samples with different Sc contents have been measured, namely 28, 31 and 36%. In Fig. 3.14, different parameters, i.e. surface roughness, real thickness, rocking curve and stress are shown for the wafers for the nominal thicknesses taken into consideration, in order to have an idea on the impact of Sc-doping on them. What can be observed, is that the surface roughness is higher for thicker films, and the rocking curve is higher for thinner ones.

Before entering in the details of the results, it is interesting to point out that the field of thin film ferroelectric capacitors, especially the thinnest ones ($t < 50\text{nm}$)

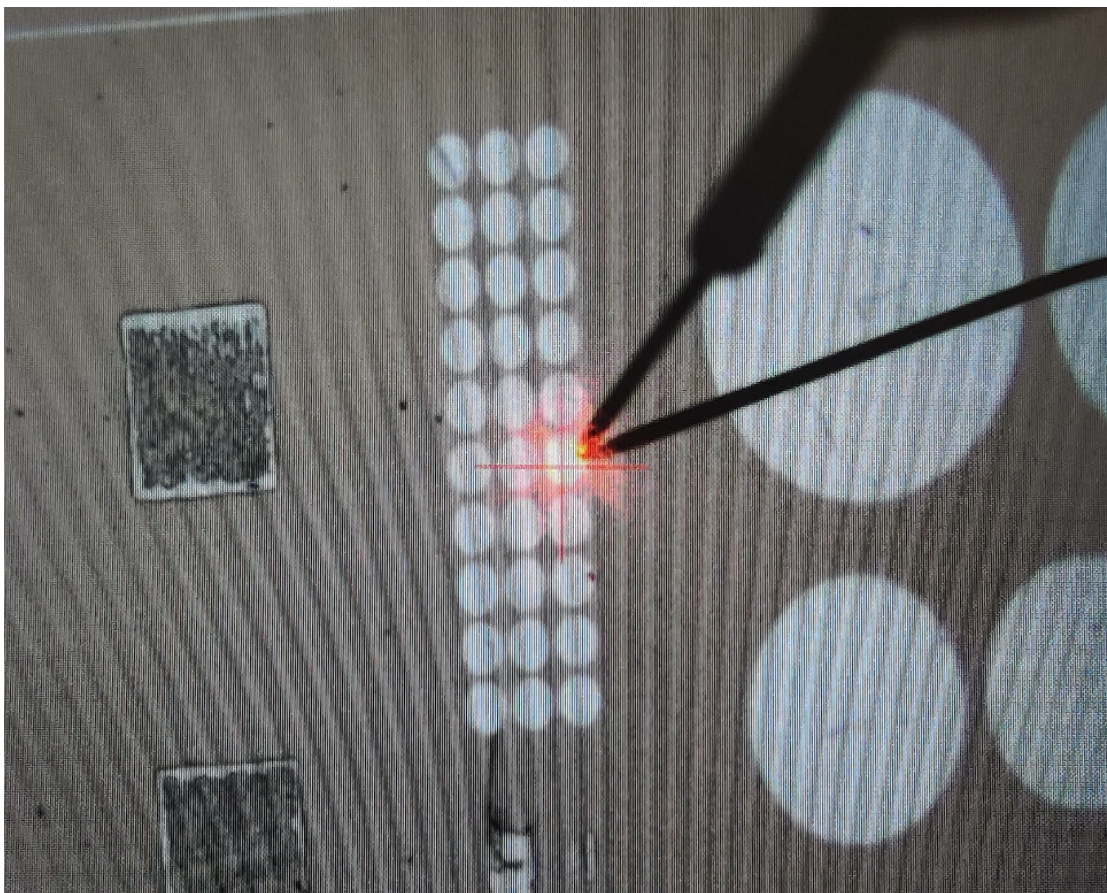


Figure 3.12: Showcase of the laser placing and probing of a small circle $100\ \mu\text{m}$ ferroelectric capacitor.

is very new and unexplored. Concerning the applications of such thin films, the main one is for memories, the so-called Fe-Ram. There is a lot of interest in this sense since, with respect to other ferroelectric materials, ScAlN is post-CMOS compatible and possesses high values of remnant polarization and coercive fields [15].

As a showcase, a PZM measurement of a square capacitor with $800\ \mu\text{m}$ side and $500\ \mu\text{m}$ thickness is depicted in Fig. 3.15, showing both the butterfly and the hysteresis curve.

The $500\ \text{nm}$ film is the one giving the best results for three main reasons: firstly, a thicker film has a higher rocking curve. This happens because, when depositing the piezoelectric material, the first 10 up to $50\ \text{nm}$ grow with crystallites which are not perfectly and vertically oriented, but show random orientation, which affects the final crystallinity of the film. For thicker ones, anyway, the fraction of the first

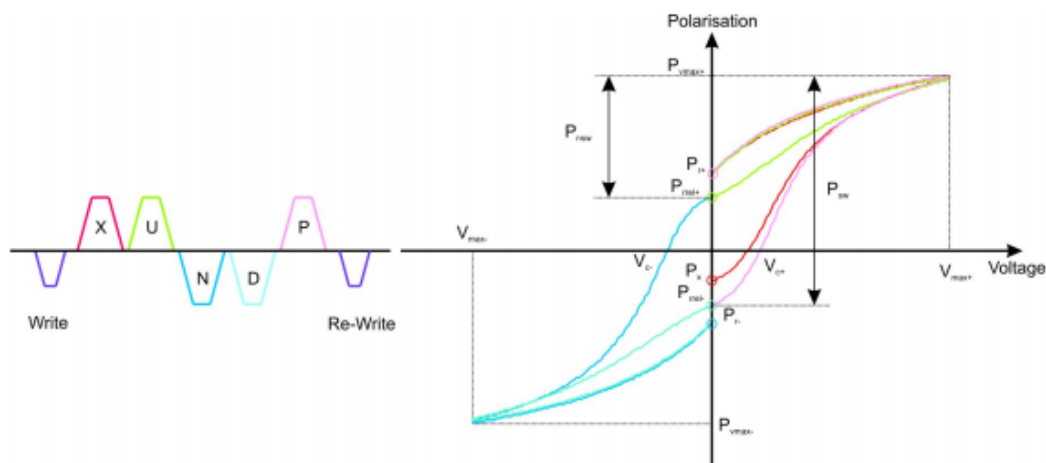


Figure 3.13: Showcase of a PM measurement with, on the left, the input signal, and on the right the output response. The picture is from the AixPplorer manual.

not-oriented atomic layers is reduced compared to the thinnest films. The second reason regards the aspect ratio of the thin-film capacitor. It has been seen and demonstrated that low aspect ratios (i.e. surface of the capacitor vs. its height) have a smoother surface, providing results closer to the ideal ones. Finally, the third reason regards the physics of thin film ferroelectric capacitors, for which thinner films see an increase of the leakage currents, which can even mask the switching one that is used to build the hysteresis curve. The concept of leakage is treated in Sect. 3.3.3. Therefore the results obtained for the 500 nm capacitors have been taken as reference for the ones gotten from the thinner capacitors.

Concerning the 250 nm capacitors, PUND measurements have been performed in order to obtain the values of remnant and relaxed remnant polarization. This has allowed to isolate the contribution to the hysteresis curve given from the switching of the capacitor from the one obtained due to leakage. The result of the PUND is shown in Fig. 3.16.

Concerning the other thicknesses, the results are similar, even though with more leakage. Nevertheless, for the 20 nm capacitors, a non-physical peculiarity has been observed: even if the capacitor is switched in the negative polarization, the negative relaxed remnant polarization is positive. This fact, which coincides with what has been obtained also from other research groups in the framework of the TUFEN research program, is still to be understood and explained. A possible explanation can be given considering the high asymmetry in the currents obtained from the measurements for the positive and negative side of the loop due to leakage, which can in-turn be caused by the presence of the native oxide on top of the film, as shown in Fig. 3.6. In the case of the negative voltages, the leakage is so high to

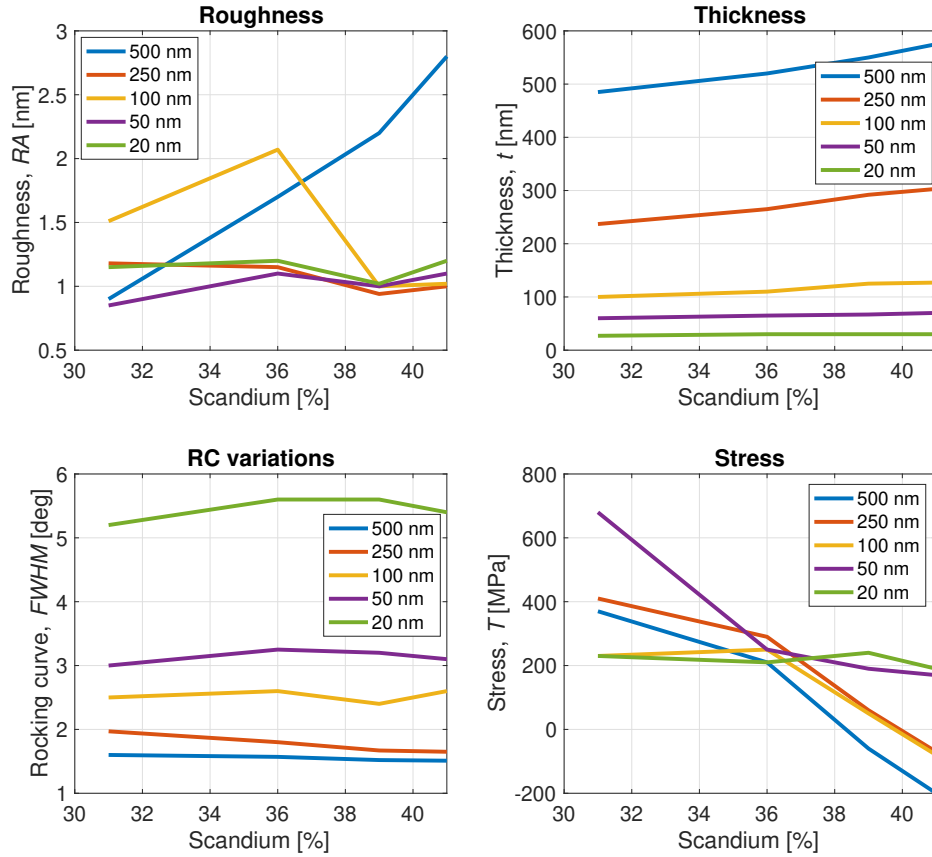


Figure 3.14: Evolution of different parameters with the Sc concentration for the thicknesses taken into account in the present work. The studied parameters are surface Roughness, film thickness, rocking curve and stress.

mask the switching peak. This does not happen in the positive part. Fig. 3.17 is the result of a PUND measurement on a 20 nm capacitor, and depicts the phenomenon.

Finally, using the PZM measurement mode, butterfly curves for different piezoelectric thicknesses have been taken. The results are shown for the 500, 250, 100 nm in Fig. 3.18. As it can be observed, the thinner the capacitor, the higher the noise in the measurement due to the increased surface roughness of the capacitor, due to its higher aspect-ratio. Moreover, due to the great asymmetry in the current, a great asymmetry in the butterfly curve can be observed as well.

From the displacement (and so the strain) vs. voltage characteristics, the d_{33} piezoelectric coefficient can be extracted. In order to do it, the applied voltage should be lower than the coercive one, in order to have a linear response of the

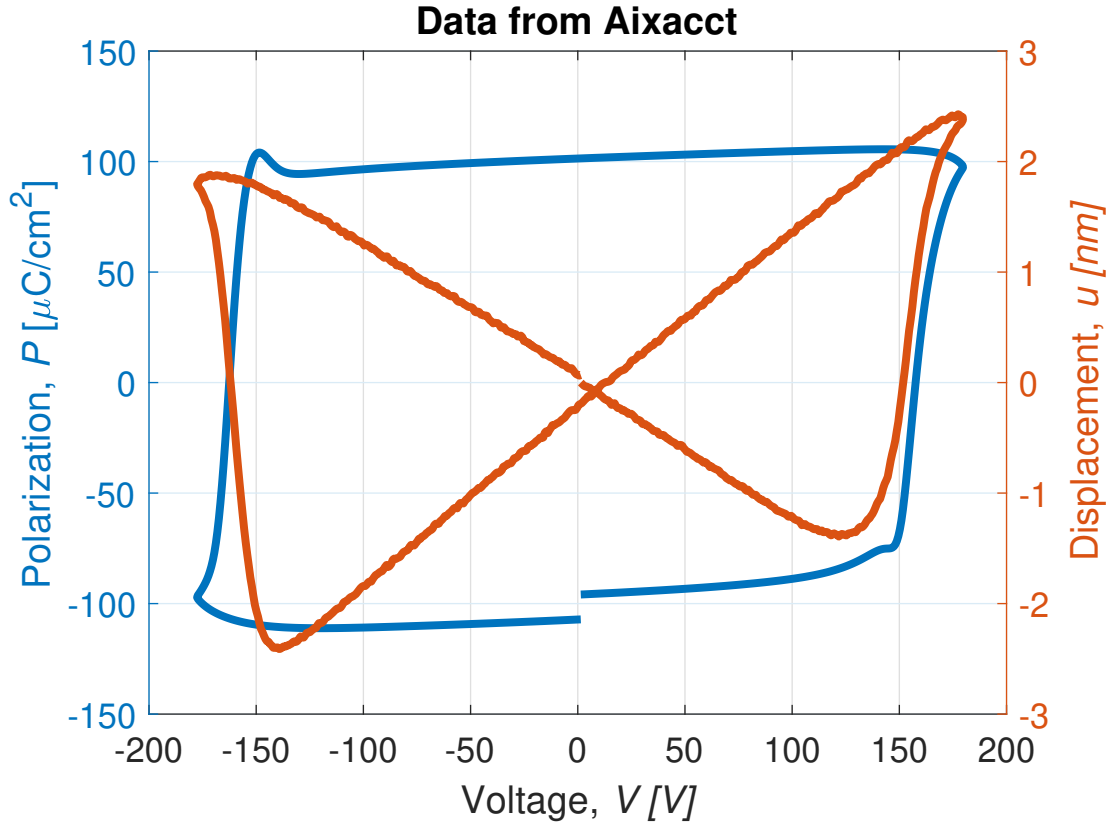


Figure 3.15: Showcase of the data collected with the Aixacct tool. In particular, the blue curve shows the hysteresis with respect to the applied voltage, while the red one shows the butterfly curve.

material and do not create offsets due to the non-linear regions of the butterfly curve. The d_{33} values have been then extracted for different thicknesses and Sc concentrations by using the linear regression method, and the values can be seen in Fig. 3.19. In that figure, the ab-initio values predicted by Caro *et al.* in [22] are also shown. What is interesting to notice is that, with higher thicknesses, and therefore better rocking curves, the piezoelectric coefficients value gets closer to the ab-initio value. This fact is not surprising, since it is known that the piezo coefficients depend on the crystallinity of the films.

3.3.3 Leakage current compensation

Thin film ferroelectric capacitors suffer from high leakage currents, which can mask the switching one, and create artifacts in the hysteresis curve. The leakage phenomenon becomes more severe when shrinking the film thickness, leading

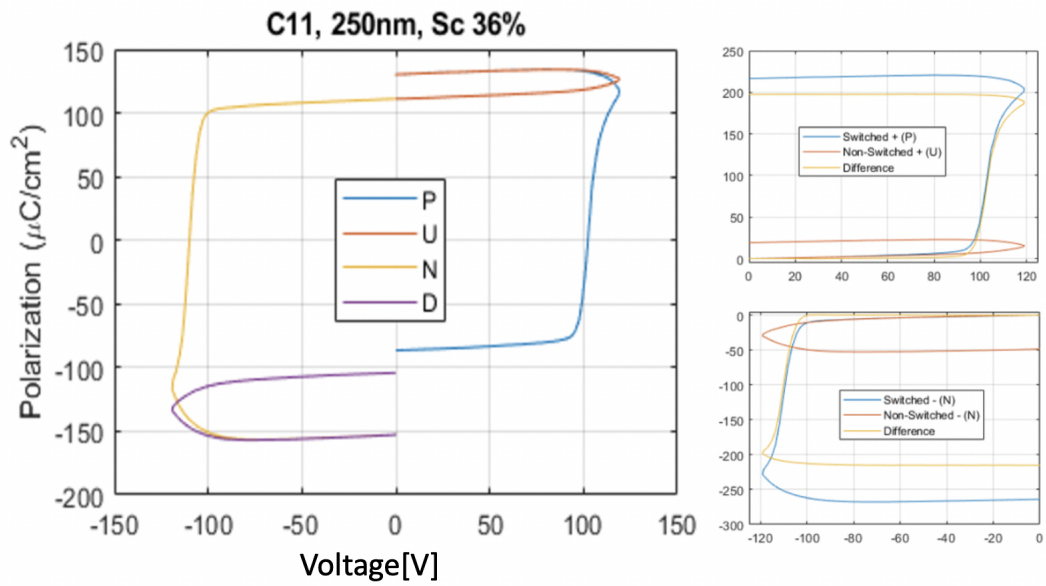


Figure 3.16: On the left, there is the result of the PUND measurement on the 250 nm thick capacitors. In the insets on the right, the curves have been post processed with MatLab to isolate the switching from the non-switching part of the hysteresis curve.

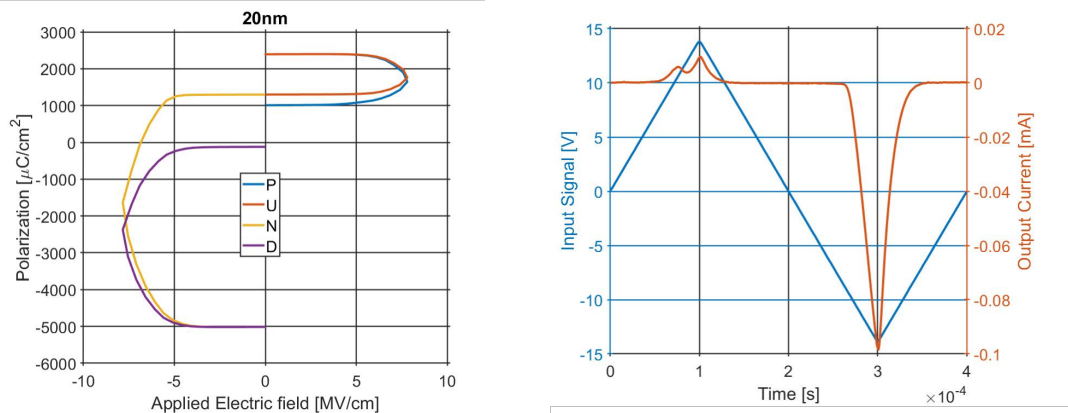


Figure 3.17: On the left, the result of a PUND measurement on a 20 nm thick ferroelectric capacitor. In the figure, it can be observed that there is a probably unphysical phenomenon for which the negative relaxed remnant polarization is positive. On the right, the high asymmetry in the current for the positive and negative voltages is shown.

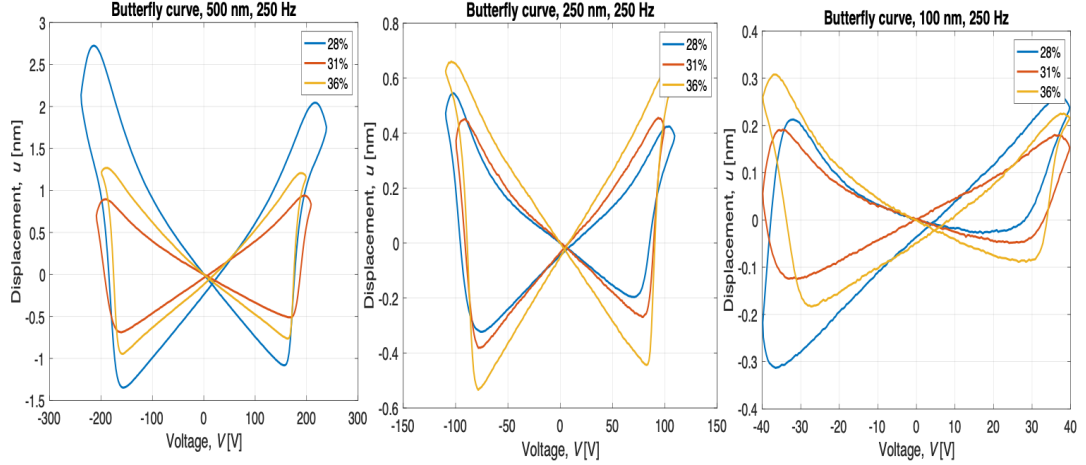


Figure 3.18: Butterfly curves for the 500, 250 and 100 nm-thick capacitors. For each thickness, three different Sc concentrations are taken into account, namely 28, 31 and 36%.

to situations in which the switching peak is not visible anymore. In order to compensate for the leakage, the Dynamic Leakage Current Compensation (DLCC) method has been developed [30]. The DLCC approach is based on the assumption that the leakage current (i_R) inside a ferroelectric capacitor is ohmic and does not depend on the frequency. On the contrary, the switching current (i_{SW}) and the current of the capacitor (i_c) have a frequency dependence. Therefore, the total current that is effectively measured is the sum of these three contributions:

$$i_{tot} = i_R + i_{SW} + i_c \quad (3.1)$$

where $i_{SW} = \omega i_{SW}^0$ and $i_c = \omega i_c^0$.

The standard DLCC method requires two measurements at two different frequencies to eliminate the ohmic current:

$$i_{comp} = \frac{\omega}{\omega_1 - \omega_2} [i(\omega_1) - i(\omega_2)] \quad (3.2)$$

Then, by integrating the current with respect to time, the polarization can be computed. Nevertheless, the assumption of the DLCC method, i.e. that the switching and the capacitor currents are linearly dependent on the frequency, means that the coercive fields should be independent on it, as explained in the addendum of [15]. It's not the case of ScAlN, for which not only the polarization values, but also the coercive voltages are dependent on the frequency of the excitation signal. To overcome this problem, in that addendum, an alternative DLCC method is explained. The key assumption, in this case, is to consider the switching current

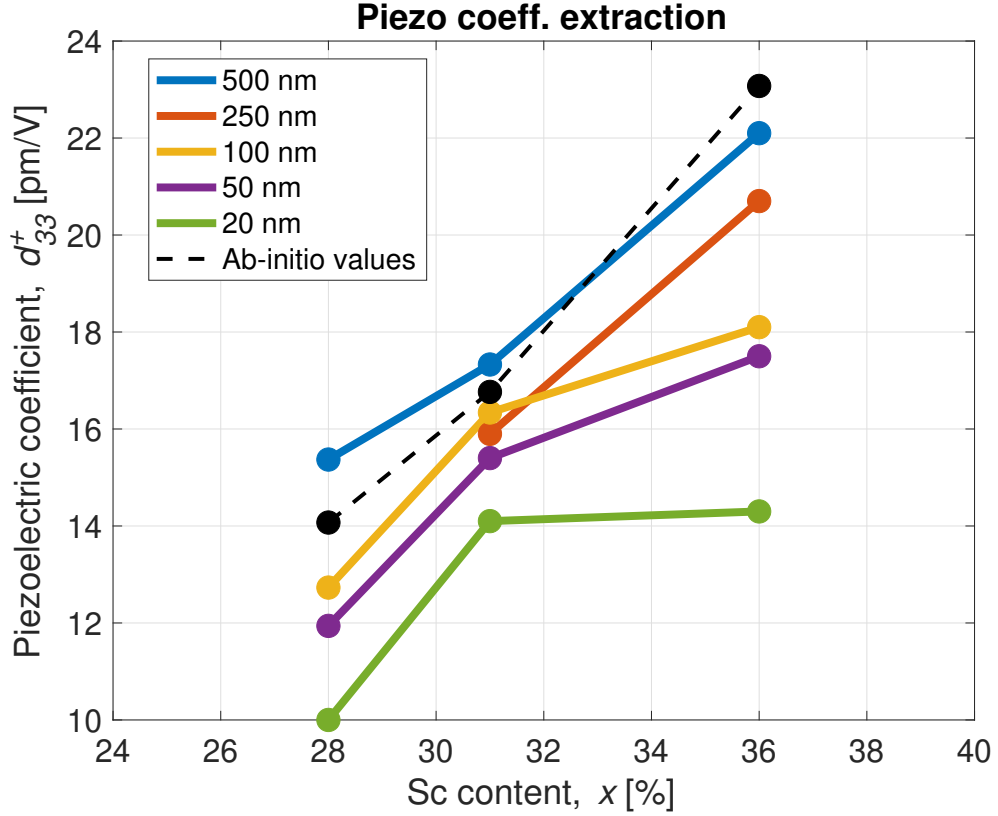


Figure 3.19: Evolution of the d_{33} piezoelectric coefficient with the Sc content for different thicknesses, compared to the ab-initio values from [22].

as null during repeated unipolar voltage sweeps. In this case, the effect of the frequency dependent coercive fields is excluded. The leakage current can then be calculated from the following formula:

$$i_R = \frac{i_2\omega_1 - i_1\omega_2}{\omega_1 - \omega_2} \quad (3.3)$$

Finally, that calculated i_R is subtracted to the measured current to find the compensated one. This calculation requires five different measurements: a bipolar sweep that computes the current to be compensated and then two unipolar voltage sweeps, one with positive and one with negative voltages for two different frequencies, for a total of four unipolar sweeps.

The measurements are then post-processed using Matlab, with which the unipolar measurements at the same frequency are concatenated to obtain the currents i_1 and i_2 of Eq. (3.3).

3.4 FEA of ferroelectric materials

There exist a lot of literature on ferroelectric materials. In particular, there are a lot of books and papers describing their applications, fabrication steps and their characterization. Nevertheless, all the papers are experimental, and there isn't almost anything regarding the possibility of simulating them. Moreover, COMSOL, the most famous and exploited commercial Finite Element Analysis (FEA) tool, does not have a ferroelectricity module. The goal of this section is therefore to set the basis for the development of a COMSOL model of ferroelectric materials, starting from the simplest ferroelectric capacitor up to the embedding into the simulation of a reconfigurable resonator.

The first and only tentative in the integration in COMSOL of a ferroelectric model is reported in [31]. In this paper, an empiric model [32] is employed and described in the following.

In the model, a ferroelectric which can switch between only two states (p^+ and p^-) is considered. Both the states are equilibrium configurations. If one considers a ferroelectric capacitor polarized e.g. in the negative state p^- , the application of a voltage to one of its terminals imposes a change in its polarization, which results in an increment of the positive polarization state Δp^+ :

$$\Delta p^+ = (1 - p^-) \cdot f^+ \cdot \Delta V \quad (3.4)$$

This equation states that the increment in positive polarization is proportional to the volume fraction of the material which has not switched yet ($1 - p^-$) times a switching probability, given by the product of the applied voltage ΔV and a function f^+ , with the form:

$$f^+ = \frac{1}{V_0} \cdot \frac{1}{1 + e^{\frac{-(V-V_c)}{V_0}}} \quad (3.5)$$

where V_c is the coercive voltage and V_0 the thermal one, with the expression:

$$V_0 = \frac{k \cdot T}{q} \quad (3.6)$$

where k is the Boltzmann constant, T the temperature and q the electron charge. Combining together the previous equations, one has:

$$p^+ = 1 - (1 - p_i^+) \cdot \frac{1 + e^{\frac{V_i - V_c}{V_0}}}{1 + e^{\frac{V - V_c}{V_0}}} \quad (3.7)$$

where V_i and p_i^+ are the initial voltage and positive polarization, respectively. The dielectric displacement vector D^+ can be written as:

$$D^+ = P_s(2p^+ - 1) \quad (3.8)$$

where P_s is the spontaneous polarization. The values of polarization and dielectric displacement for the case of negative voltages, namely p^- and D^- can be computed in a similar manner.

The paper proceeds by saying that they made a 3D model of a cylindrical ferroelectric capacitor using the physics *electric currents* and *piezoelectric device* to obtain the hysteresis and butterfly curve, respectively. Unfortunately, does not give many details more and remains obscure. Images of the curves are shown, and the authors say that they match the experiment. Unluckily, with the available information it is not possible to build a model, also because the COMSOL version has varied from 2010, the year of the publishing of the paper.

A further step in advance in the understanding of the model, together with an improvement of the math describing the curves comes from [33], in which a function employing hyperbolic tangents instead of exponential functions is described in order to model the hysteresis curve:

$$P^+(V) = P_s \tanh\left(\frac{V - V_c}{2\delta^+}\right) \quad (3.9)$$

where δ^+ has the form:

$$\delta^+ = V_c^+ \left[\log\left(\frac{1 + P_r^-/P_s}{1 - P_r^-/P_s}\right) \right]^{-1} \quad (3.10)$$

where P_r is the remnant polarization. This function can be more easily implemented in COMSOL.

Concerning the actual implementation, it has been carried out using the version 5.5. In particular, following the guidelines of [31], a simple 3D model of a cylindrical ferroelectric capacitor has been developed. To it, terminal and ground boundary conditions have been applied to the top and bottom faces, respectively. The physics is Piezoelectricity, and the study is a time dependent one. A fixed constrain boundary condition has been added in Solid mechanics to the bottom face of the cylinder. The geometry can be seen in Fig. 3.20a. In Fig. 3.20b, the signal applied to the terminal is plotted. As it can be observed, it is a sinusoidal signal, going from $t = 0$ to $t = T$, i.e. its period. As in Chapter 2, the custom ScAlN material has been developed using the ab-initio equations described in [22]. The Sc-doping value and the geometry have been chosen to match the ones of the experimental curve of Fig. 3.15, described in Sect. 3.3. Therefore, the Sc percentage has been set to 30%, the height of the cylinder to 500 nm and its diameter to 800 μm . Also the same voltage has been applied, i.e. a wave with amplitude 180 V.

In order to fit equation (3.9) into the model, a little trick was played: the time was added into the equation to weight the positive and negative polarization. In particular, ad hoc step-like functions have been introduced into the model:

$$Step(t, t_c) = \frac{1}{1 + e^{-\frac{t-t_c}{t_0}}} \quad (3.11)$$

where t_c is the time at which the maximum or minimum voltage is reached in the input signal (i.e. $t_{c1} = 1/4T$ and $t_{c2} = 3/4T$) and t_0 is a time very close to $t = 0$, i.e. when the voltage is almost null. In this way, the analytical equation given to COMSOL has the form:

$$P = P_s \cdot \tanh\left(\frac{E - E_c^-}{\delta}\right) \cdot (Step(t, t_{c1}) + Step(-t, -t_{c2})) + P_s \cdot \tanh\left(\frac{E - E_c^+}{\delta}\right) \cdot (1 - Step(t, t_{c1}) - Step(-t, -t_{c2})) \quad (3.12)$$

In order to make COMSOL recognize that this function represents the polarization, it has to be inserted in **Solid Mechanics** \rightarrow **Piezoelectric material** \rightarrow **Remanent electric displacement**. Doing this, when plotting the remnant dielectric displacement as function of the voltage, the result is shown in Fig. 3.21a. Fig. 3.21b shows the same curve but as function of the time.

This curve takes as assumption that the ferroelectric capacitor has been already polarized. In order to simulate a curve of P vs. V where the polarization starts from zero, a more complex function is required:

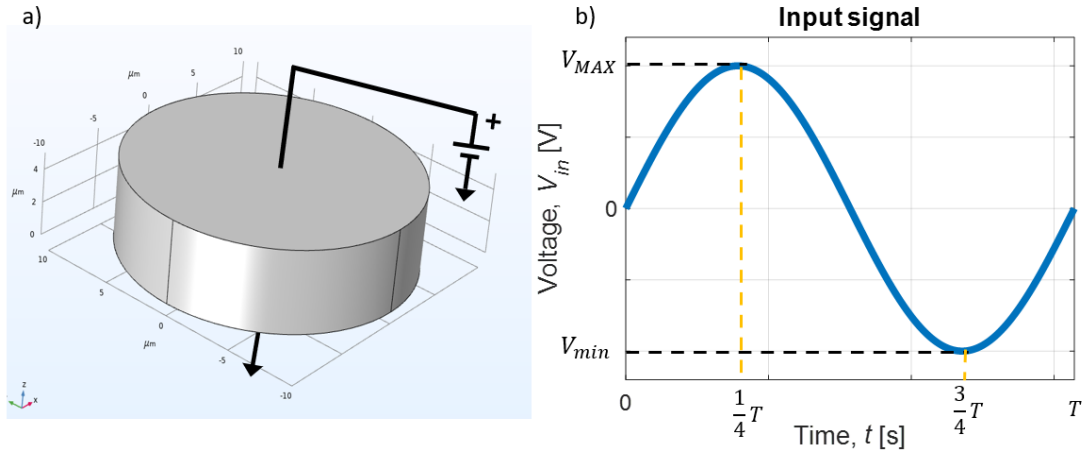


Figure 3.20: a) COMSOL 3D simulated geometry. The terminal and ground are shown. b) Input signal given to the terminal, with maximum and minimum value highlighted.

$$\begin{aligned}
 P = & P_s \cdot \tanh\left(\frac{E}{\delta}\right) \cdot \text{Step}(t, t_{c1}) + P_s \cdot \tanh\left(\frac{E - E_c^-}{\delta}\right) \cdot \text{Step}(-t, -t_{c2}) \cdot \text{Step}(t, T) + \\
 & + P_s \cdot \tanh\left(\frac{E - E_c^-}{\delta}\right) \cdot \text{Step}(t, T + t_{c1}) + P_s \cdot \tanh\left(\frac{E - E_c^-}{\delta}\right) \cdot \text{Step}(-t, -T - t_{c2}) (1 - \text{Step}(t, T)) + \\
 & + P_s \cdot \tanh\left(\frac{E - E_c^+}{\delta}\right) \cdot (1 - \text{Step}(t, t_{c1}) - \text{Step}(-t, -t_{c2})) + (1 - \text{Step}(t, T + t_{c1}) - \text{Step}(-t, -T - t_{c2}))
 \end{aligned} \quad (3.13)$$

It's plot is shown in Fig. 3.22.

In order to simulate also the butterfly curve, the employed formula is:

$$S = d_{33}E \quad (3.14)$$

where S is the strain.

The piezoelectric coefficient d_{33} can be then expressed by the formula [34]:

$$d_{33} = 2\varepsilon_{33}Q_{33}P \quad (3.15)$$

where Q_{33} is the electrostrictive coefficient. Unluckily, that coefficient for ScAlN is not present in literature. Nevertheless, [34] provides an alternative path, for which:

$$2\varepsilon_{33}Q_{33} = \frac{d_{33sat}}{P_S} \quad (3.16)$$

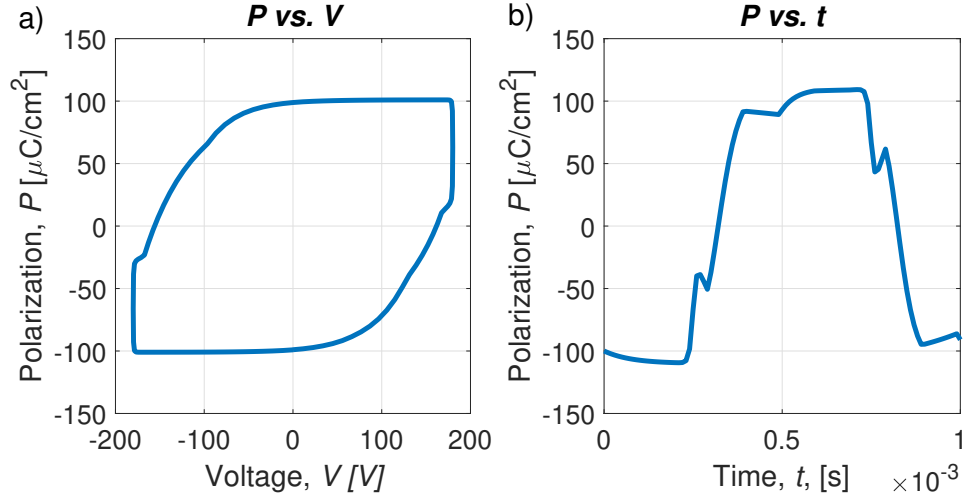


Figure 3.21: Hysteresis curve of P vs. V (a) and curve of P vs t (b) for the simulated structure of Fig. 3.20.

where d_{33sat} is the value of the piezoelectric coefficient d_{33} when the saturation polarization P_S is reached. This formula should be valid only for ferroelectric materials with a centrosymmetric paraelectric phase, like BST. Those materials do not show piezoelectricity unless a bias voltage is applied, distorting the symmetry of the phase. ScAlN, since exhibits piezoelectricity and has a wurtzite-type structure, is included in the non-centrosymmetric group. Nevertheless, as first approximation, the formula can be used to build the butterfly curve, until the electrostrictive coefficient is experimentally found. In this way, the strain can be expressed as:

$$S = \frac{d_{33sat}}{P_S} P(E) E \quad (3.17)$$

That function has to be inserted into **Solid Mechanics** \rightarrow **Piezoelectric Material** \rightarrow **Initial stress and strain** \rightarrow **Initial strain**, in the 33 component. In order to be able to compare the results of COMSOL with the experimental ones, the strain has been divided by the height of the cylinder to obtain the displacement

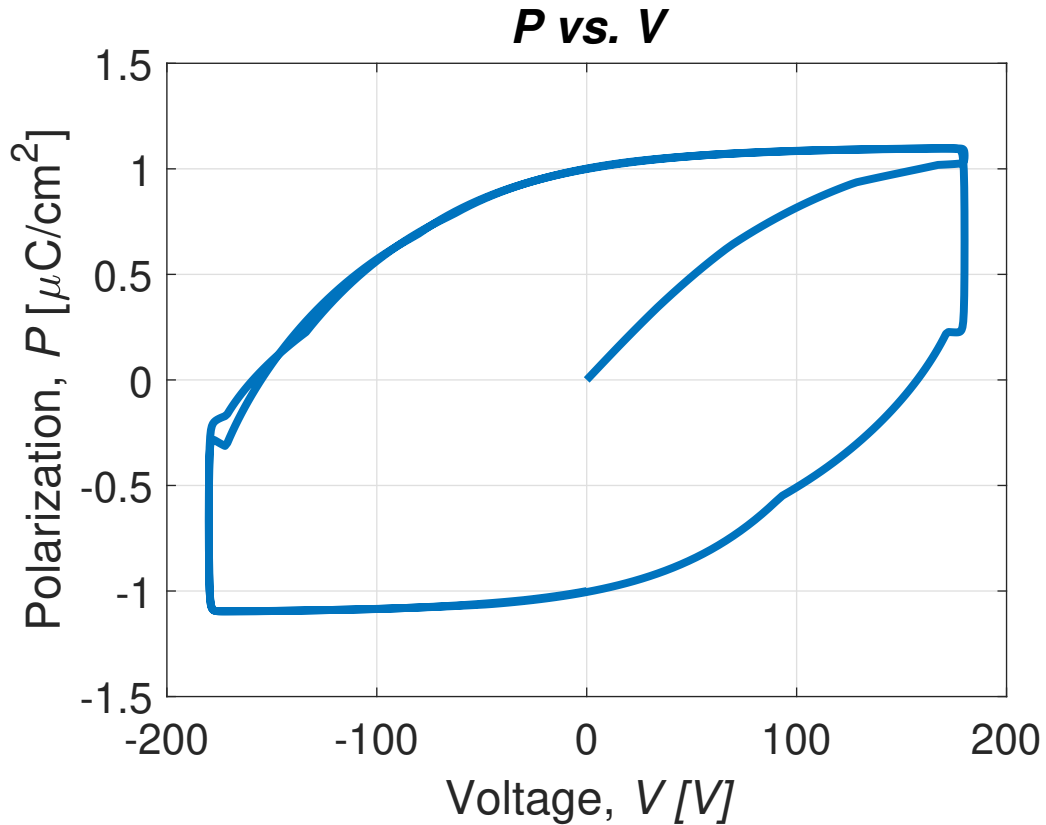


Figure 3.22: Hysteresis curve of P vs. V when the function described in Eq. (3.13) is employed, enabling the description of the polarization of an unpolarized sample.

u. The *u vs. V* and *u vs. t* curves obtained from COMSOL are shown in Fig. 3.23.

In order to see the matching of those results with the experimental ones of ScAlN, the curves are compared in Fig. 3.24a-b. As it can be observed, the results are, at least at a first approximation, matching. Nevertheless, the COMSOL hysteresis curve fails to match the wide range linearity of the experimental one. An improvement is needed.

Actually, an analytical model of the hysteresis curve capable of matching the experimental results is not trivial at all, since the ferroelectric capacitor characteristic depends not only on the current state, but also on the state's history. In [35], there is the explanation of several models used to reproduce the hysteresis curve, but none of them is able to fully capture the real, experimental curve of a ferroelectric capacitor. The reason is the failure in replicating the saturation and critical slope conditions of the curve. The new analytical model presented in [35], on the contrary, bases itself on the experimental curve, combining analytical expressions and fitting, using a certain number of points (in its most complete form, four), and it is able to recreate the hysteresis with a desirable level of agreement. Before entering in the details of the model, let's point out that, in order to obtain the mathematical expression with the correct values of the coefficients, as said before there is the need of the experimental curve. It seems paradoxical at this point

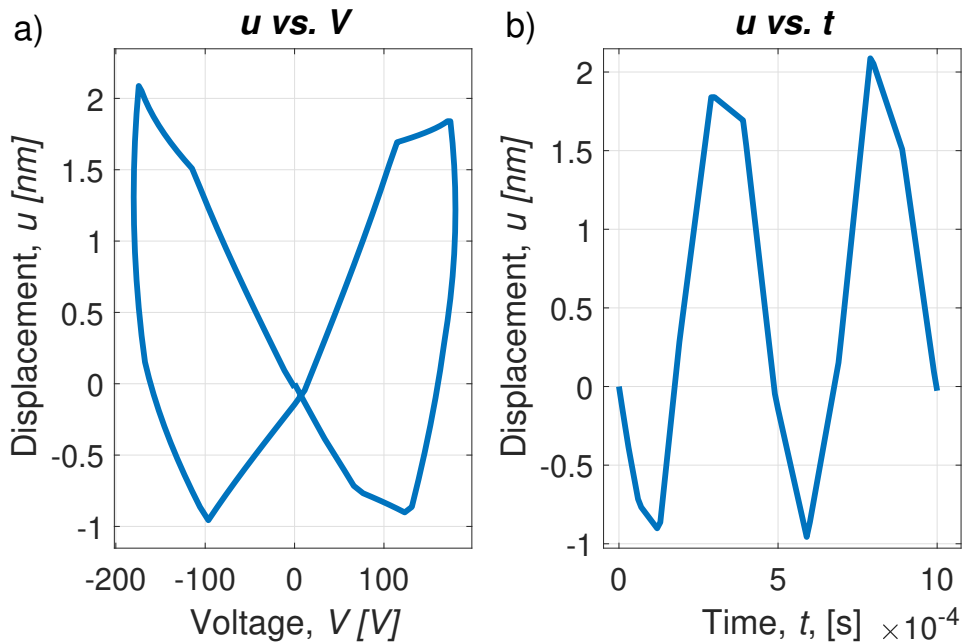


Figure 3.23: Butterfly curve of *u* v. *V* (a) and curve of *u* vs. *t* (b) for the simulated structure of Fig. 3.20.

that, in order to simulate a ferroelectric capacitor, it has firstly to be fabricated and measured. Actually, since the hysteresis curve is intrinsic of the material, with this descriptions also other structures can be simulated. Moreover, the fact of having mathematical expressions gives an higher degree of versatility and precision, since the experimental measurements are always affected by uncertainties and noise. Therefore, in the case of ScAlN, the curves for the dopant concentrations of interest can be gathered once, and from them the models can be built. The starting point of the model of [35], is another one developed by Wang et al. [36], and briefly described in the following.

This model treats a ferroelectric material as consisting of multiple grains. The reason is that a single-domain ferroelectric converts into a multi-domain one when the switching process takes place. Therefore, a simple single-domain model would fail to describe this class of materials, especially the polycrystalline ones. Also in this model, two possible states of polarization are considered (P^+ and P^-), and they are linked by the expression $P^+ = -P^-$. The total free energy of the ferroelectric material is given by the summation of the various contributions coming from the two polarization states, the paraelectric one and the domain walls:

$$F = F_0 + F^+ + F^- + F_{wall} \quad (3.18)$$

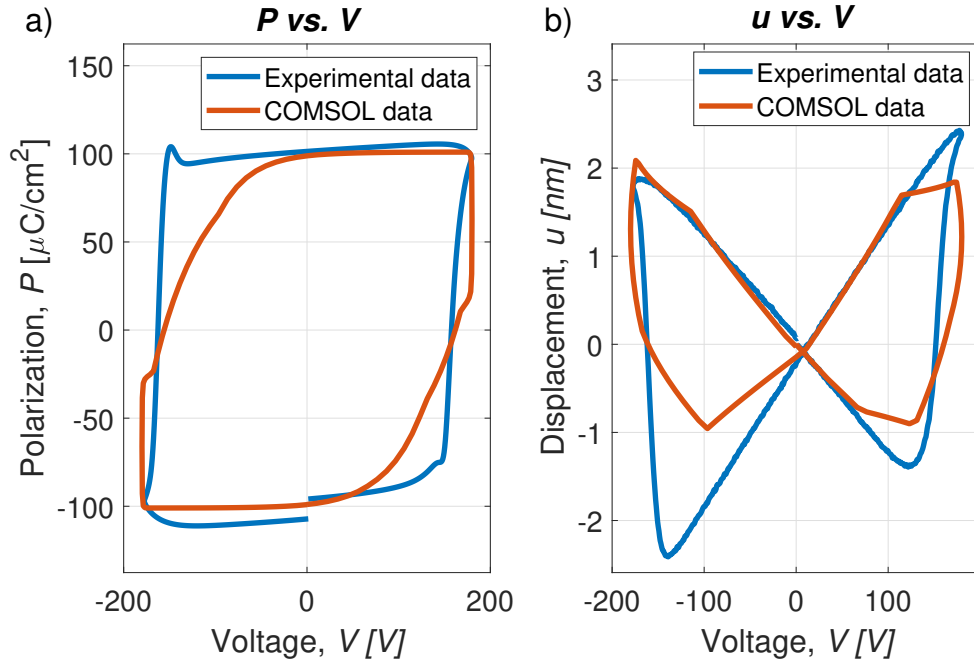


Figure 3.24: Comparison of the experimental curves of P vs. V (a) and u vs. V with the ones extracted with COMSOL.

This free energy, can be also expressed as function of the polarization P^+ :

$$F = F_0 - \frac{\alpha}{2}P^{+2} + \frac{\beta}{4}P^{+4} + (1 - \alpha^+)E P^+ \quad (3.19)$$

where α and β are Landau coefficients and F_0 is the free energy in the paraelectric state. The coefficient α^+ is the volume fraction of upward polarization, related to the one of downward polarization α^- from the expression $\alpha^+ = 1 - \alpha^-$. Since the completely switched state is an equilibrium state, the value of P^+ can be found deriving Eq. (3.19) and posing it equal to zero. In order then to find the average polarization P , the upward and downward polarization can be weighted by the α coefficients:

$$P = \alpha^+P^+ + \alpha^-P^- = (2\alpha^+ - 1)P^+ \quad (3.20)$$

The expression of α^+ is found by fitting the formula with experimental hysteresis, obtaining:

$$\alpha^+ = \frac{\arctan(\beta_1(E - E_c) + \beta_2(E - E_c)^3 + \pi/2)}{\pi} \quad (3.21)$$

where β_1 and β_2 are constants. This model shows a certain degree of accuracy in reproducing the hysteresis curve, but lacks in a good approximation of the curve close to E_c . The reason is the abrupt change of α^+ close to the coercive fields, for which it goes from 0 to 1 in a very sharp way. Moreover, the values of β_1 , β_2 and β cannot be computed analytically, and they must be found by a trial and error process.

The new model of [35] develops a way to obtain the β coefficients. Moreover, by using some points of the hysteresis curve, a fitting is performed in order to obtain a closer agreement with experimental results. As it will be shown in the following, there are three major steps in the development of the final model: 2, 3 and 4-points fitting. Let's start with the 2-points.

As shown in Eq. (3.20), the polarization is given by:

$$P = (2\alpha^+ - 1)P^+ \quad (3.22)$$

Let's then consider two points on the experimental hysteresis curve, namely the ones with $E = 0$ and $E = -E_c$. The values of the polarization at those points can be simply read on the curve. Anyway, their expression will be:

$$P_j = (2\alpha_j^+ - 1)P^+ \quad (3.23)$$

where $j = 1,2$. From it, the normalized polarization can be found:

$$r_j = \frac{P_j}{P^+} = 2\alpha_j^+ - 1 \quad (3.24)$$

By inverting this formula, also the values of α_j^+ can be found:

$$\alpha_j^+ = \frac{r_j + 1}{2} \quad (3.25)$$

The equation for α^+ of the model of Wang, can be generalized as:

$$X_j = \tan\left(\pi\alpha_j^+ - \frac{\pi}{2}\right) \quad (3.26)$$

where:

$$X_j = \beta_1(E_j - E_c) + \beta_2(E_j - E_c)^3 \quad (3.27)$$

Considering the two points taken on the curves, the values of X_1 and X_2 are:

$$X_1 = \beta_1(-E_c) + \beta_2(-E_c)^3 \quad (3.28)$$

$$X_2 = \beta_1(-2E_c) + \beta_2(-2E_c)^3 \quad (3.29)$$

From Eqs. (3.28) and (3.29), the values of the coefficients β_1 and β_2 can be found by employing the inverse matrix method:

$$\begin{bmatrix} \beta_1 \\ \beta_2 \end{bmatrix} = M^{-1} \begin{bmatrix} X_1 \\ X_2 \end{bmatrix} \quad (3.30)$$

where the matrix M has the form:

$$M = \begin{bmatrix} -E_c & -E_c^3 \\ -2E_c & -8E_c^3 \end{bmatrix} \quad (3.31)$$

In this way, the function $X(E)$ can be computed from:

$$X(E) = \beta_1(E - E_c) + \beta_2(E - E_c)^3 \quad (3.32)$$

This function can be given to:

$$\alpha^+(E) = \frac{\arctan[X(E)] + \pi/2}{\pi} \quad (3.33)$$

and the latter equation can in turn be given to Eq. 3.22 to build the curve. This method provides excellent agreement for the curve in the regions close to the selected points, but has still a non-correct matching for points far from them. The comparison of the curve obtained with the model and the experimental one is shown in Fig. 3.25.

In order to refine the model, a third point on the curve can be taken into account. In particular, this point has a value of field close to E_c , being selected at $E = E_c(1 \pm z)$. The specific value of z is chosen such as:

$$0 < E_c(1 \pm z) < E_{MAX} \quad (3.34)$$

where E_{MAX} is the maximum field applied. In this case, the function for X_j is modified to:

$$X_j = \beta_1(E_j - E_c) + \beta_2(E_j - E_c)^3 u(E_j - E_c) + \beta_3(E_j - E_c)^5 \quad (3.35)$$

where $u(x)$ is the unit step function with the discontinuity when $x = 0$. By applying the same reasoning shown for the case of two points, the hysteresis curve can be finally obtained. The result is matching much better the experimental results, just lacks agreement below the coercive field. That's why the 4-points model is introduced.

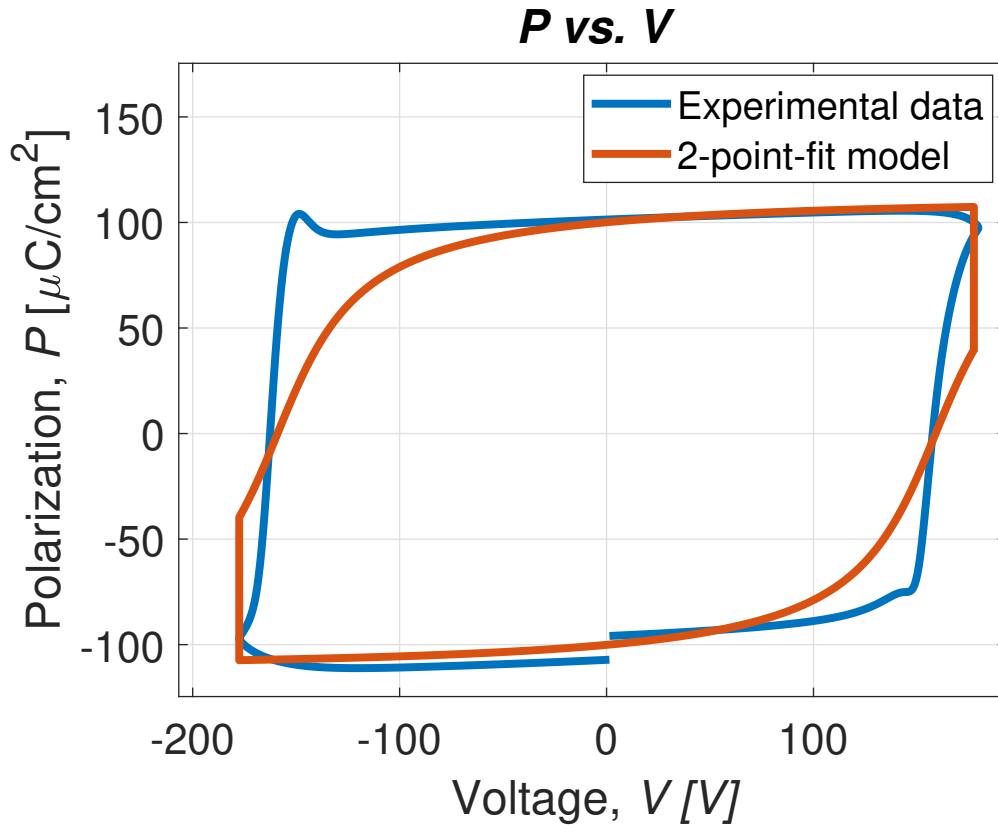


Figure 3.25: Comparison of the experimental curves of P vs. V with the model made by the 2-points-fit described in [35].

In this case, the four fitting points are the ones with $E = 0$, $E = -E_c$ and $E = (1 \pm z)E_c$, with z satisfying the relation of Eq. (3.34). The expression of X_j in this final case becomes:

$$X_j = \beta_1(E_j - E_c) + \beta_2(E_j - E_c)^2 u(E_j - E_c) + \beta_3(E_j - E_c)^2 u(E_c - E_j) + \beta_4(E_j - E_c)^3 \quad (3.36)$$

Following the same procedure of the previous two cases, the β constants can be found from:

$$\begin{bmatrix} \beta_1 \\ \beta_2 \\ \beta_3 \\ \beta_4 \end{bmatrix} = M^{-1} \begin{bmatrix} X_1 \\ X_2 \\ X_3 \\ X_4 \end{bmatrix} \quad (3.37)$$

With the matrix M of the form:

$$M = \begin{bmatrix} -E_c & 0 & (-E_c)^2 & (-E_c)^3 \\ -2E_c & 0 & (-2E_c)^2 & (-2E_c)^3 \\ zE_c & (zE_c)^2 & 0 & (zE_c)^3 \\ -zE_c & 0 & (-zE_c)^2 & (-zE_c)^3 \end{bmatrix} \quad (3.38)$$

With the values of the β constants, the hysteresis curve can then be computed, having excellent agreement with the experimental results, as seen in Fig. 3.26a.

The function can be implemented in COMSOL. In this case, as step function, the one of COMSOL is used. The values of the M matrix are firstly obtained with MatLab and then fed to the model. With them, the β constants are computed. Then, $X(E)$ is introduced as analytic function. In particular, two functions are needed, one for positive and one for negative coercive fields. They will be denoted as $X_1(E)$ and $X_2(E)$, respectively. In the same way, two $\alpha(E)$ functions are generated, namely $\alpha_1(E)$ and $\alpha_2(E)$, where the first employs $X_1(E)$ and the second $X_2(E)$. Finally, the analytic function of polarization is given to the model, and is weighted with time by the $Step(t, t_c)$ functions:

$$P = P_s(2\alpha_1 - 1)(Step(t, t_{c1}) + Step(-t, -t_{c2})) + P_s(2\alpha_2 - 1)(1 - Step(t, t_{c1}) - Step(-t, -t_{c2})) \quad (3.39)$$

Using the same procedure explained in the previous model, also the butterfly curve can be reproduced, as shown in Fig. 3.26b. Although the greater agreement of the hysteresis curve, the butterfly one shows a lower degree of accordance to the

experimental results. Therefore, in the current stage of development of the model, both the Polarization curves are kept, the first one to build the S vs. E curve and the second one to build the P vs. E one.

In order to have a further validation of the model, the curve of the dielectric constant can be extracted from the hysteresis curve. In fact, as first approximation, ε_r can be obtained as:

$$\varepsilon_r = \frac{1}{\varepsilon_0} \frac{dP}{dE} \quad (3.40)$$

The experimental hysteresis curve, as well as the ones obtained with the two models in COMSOL, have been numerically derived with Matlab. The results are shown in Fig. 3.27. As it can clearly be observed, the second model gives much better agreement with the curve extracted from the experimental data. The only mismatch is found for values of the field close to the maximum and the minimum, for which the smoothed edges of the curve create a singularity.

As already mentioned, the study was a time dependent one, for which the system is evaluated for times going from 0 to T . Actually, given the structure of the model, it is easily extended to the case of a stationary study. In fact, the analytical

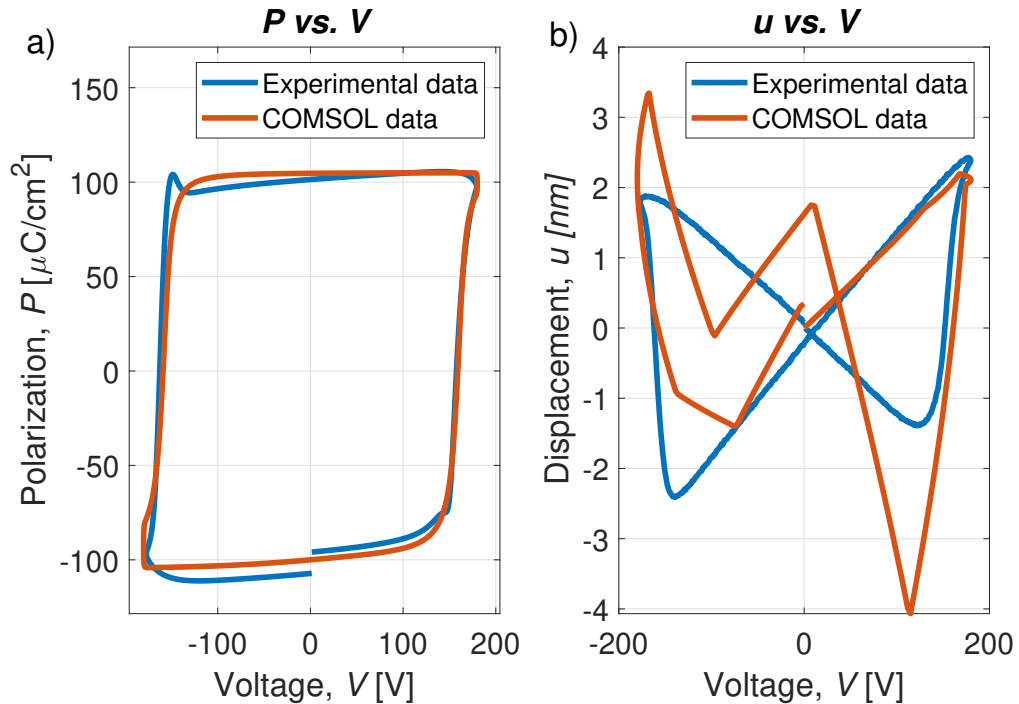


Figure 3.26: Comparison of the experimental curves of P vs. V (a) and of u vs. V with the improved model made by the 4-points-fit described in [35].

function defining the polarization and the strain is dependent on the time. In the same way, also the applied field is function of time. That time is swept in a time dependent study, but can be set at any value in a stationary one. Therefore, by freezing the time, the system is constrained in the relative polarization state. In this way, different configurations can be simulated. Fig. 3.28 show the values of polarization and strain of the ferroelectric capacitor frozen at $t = 0, T/4, 3/4T$, validating the model.

The last and most important step is to integrate ferroelectricity into the simulation of a piezoelectric MEMS resonator. The first thing to do is to extend the model to a 2D simulation. This is done by changing the coordinate system from **Global coordinates** to **Material XZ-plane system**. Another way is to apply all the functions to the Y coordinate instead of the Z one. The next steps will refer to the first method. In order to simulate a resonator response, as shown in Chapter 2, the study is a frequency domain one. In this case, the same strategy of the stationary study can be applied: the system is frozen at a specific time, which defines the polarization state. Nevertheless, in this case a further step is taken: the resonator is assumed to have been polarized in a certain state by the application

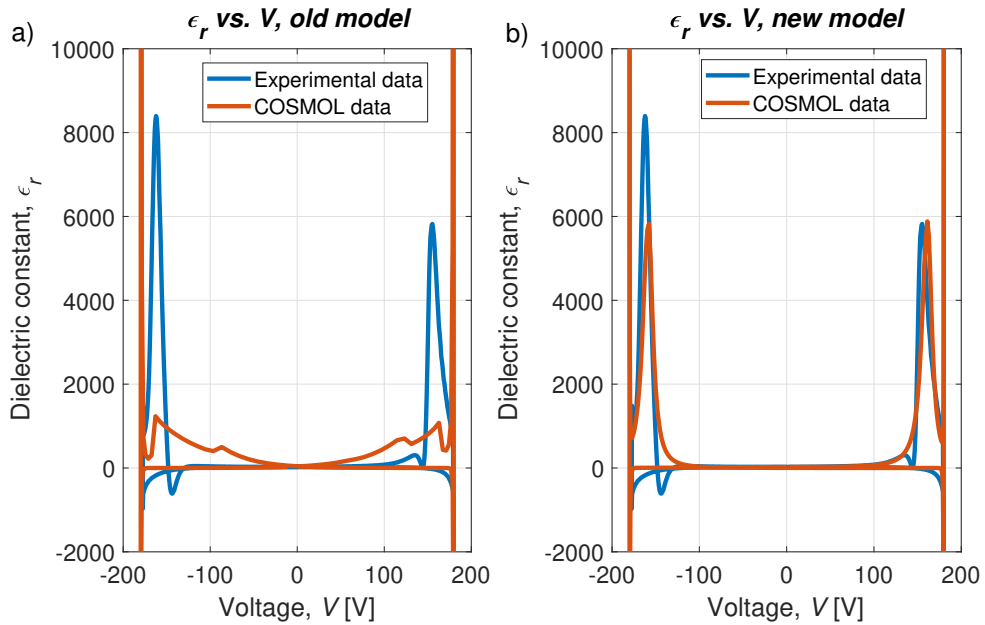


Figure 3.27: Comparison of the extracted curve of ϵ_r vs. V from the experimental data with (a) the extracted curve from the old model and (b) the one obtained with the new one. The y-axis has been limited in order to be able to better capture the plots. The singularity is due to the smoothed edges of the hysteresis curves obtained with analytical models.

of a DC bias. Then, the bias is removed, and the switched resonator is simulated. This means that the sinusoidal voltage will not be applied to the terminal anymore, only the AC signal is applied to it. This does not constitute a problem, since also the applied voltage which appears in the polarization function is dependent on the time. Therefore, there is no need to physically apply the DC signal, it can just be taken into account into the field applied to the polarization, which is defined as $P = P(t, E(t))$. Concerning the strain, since the DC voltage is not considered to be applied and since it is null for null or small-valued field applied, it is not included in the model.

To make the model accurate, also the changes in the material properties have been taken into account, in particular the ones of the piezoelectric coefficient d_{33} and of the relative permittivity ε_r . At the current state of the model development, the changes in the elastic properties of the material with the polarization have not been taken into account. To superimpose the new values of the the piezoelectric and dielectric coefficients to the ones on natural ScAlN, two custom functions have been applied to them under **Solid Mechanics** \rightarrow **Piezoelectric Material** \rightarrow **Coupling Matrix, Voigt notation** and **Relative permittivity**, respectively. The relative permittivity function is the one shown in Fig. 3.27, to which the singularities have been removed. Concerning the d_{33} coefficient, it is obtained by

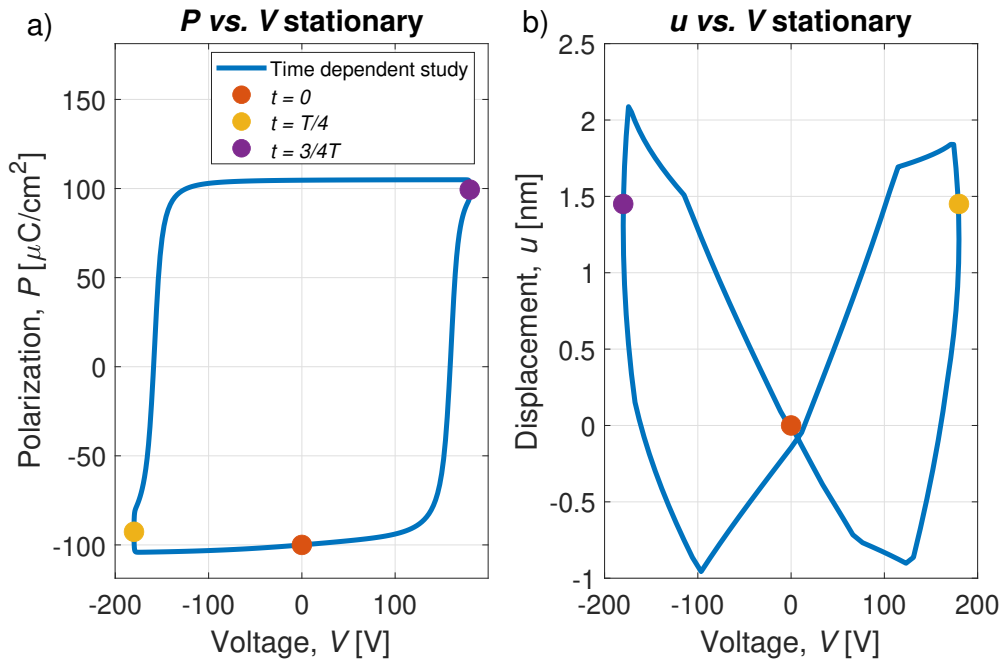


Figure 3.28: Showcase of the correct functionality of the model's extension to the stationary study case.

deriving the strain curve with respect to the field:

$$d_{33} = \frac{dS}{dE} \quad (3.41)$$

Since the agreement with the experimental data for the butterfly curve is not yet perfect, in this case the experimental curve has been derived numerically. After that, given its roughness, it has been smoothed before being given to COMSOL. Fig. 3.29 shows the comparison of the original and the smoothed curves. Both the ε_r and d_{33} functions are expressed with respect to time, and therefore can be controlled by it as well.

Finally, the resonator response is simulated. The kind of simulated resonator is an FBAR. The reason lies in its only dependence on d_{33} for the resonance, while, as shown in Chapter 2, a CLM resonant mode also depends on the piezoelectric

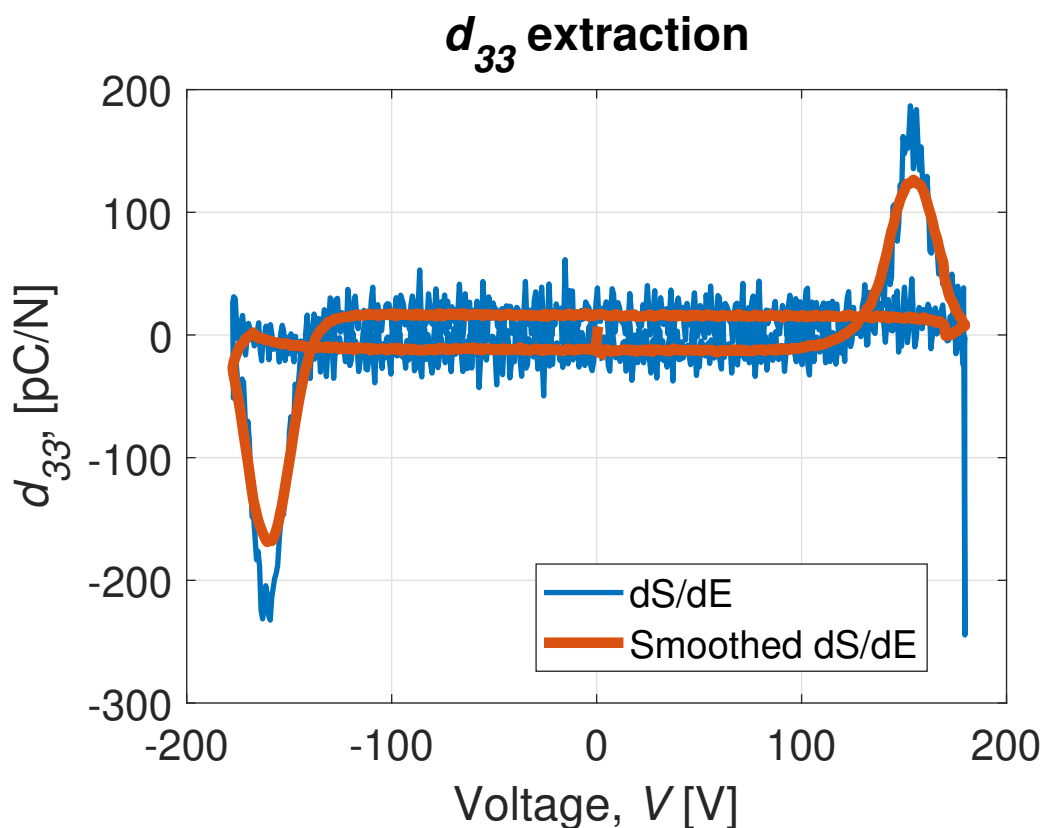


Figure 3.29: Curve of the piezoelectric coefficient d_{33} extracted by deriving the butterfly curve with respect to the electric field. The function is shown either in its natural form and in a smoothed form. The latter is the function that has been given to COMSOL.

coefficient d_{31} , for whose variation there is no experimental data. In order to make sure that the model is formally correct, the value of polarization for $t = 0$ has been set to 0, and the dielectric and piezoelectric coefficients for $t = 0$ have been set as the one of natural ScAlN. In this way, when simulating the resonator for $t = 0$, the response will be the one of a non-switched, non-ferroelectric one. The comparison of the admittance curves for a non-ferroelectric and a ferroelectric FBAR at $t = 0$ for 30% Sc concentration is shown in Fig. 3.30.

As a last step, the FBAR for different times is simulated, and the result is shown in Fig. 3.31. The values of t , P , ε_r and d_{33} used in the simulation are listed in Table 3.1. As it can be observed from the figure, the static capacitance C_0 is different for the different times, meaning that the dielectric constant has varied. In particular, it has increased. Moreover, also the spontaneous polarization has the effect of increasing the static capacitance. What can also be observed is that

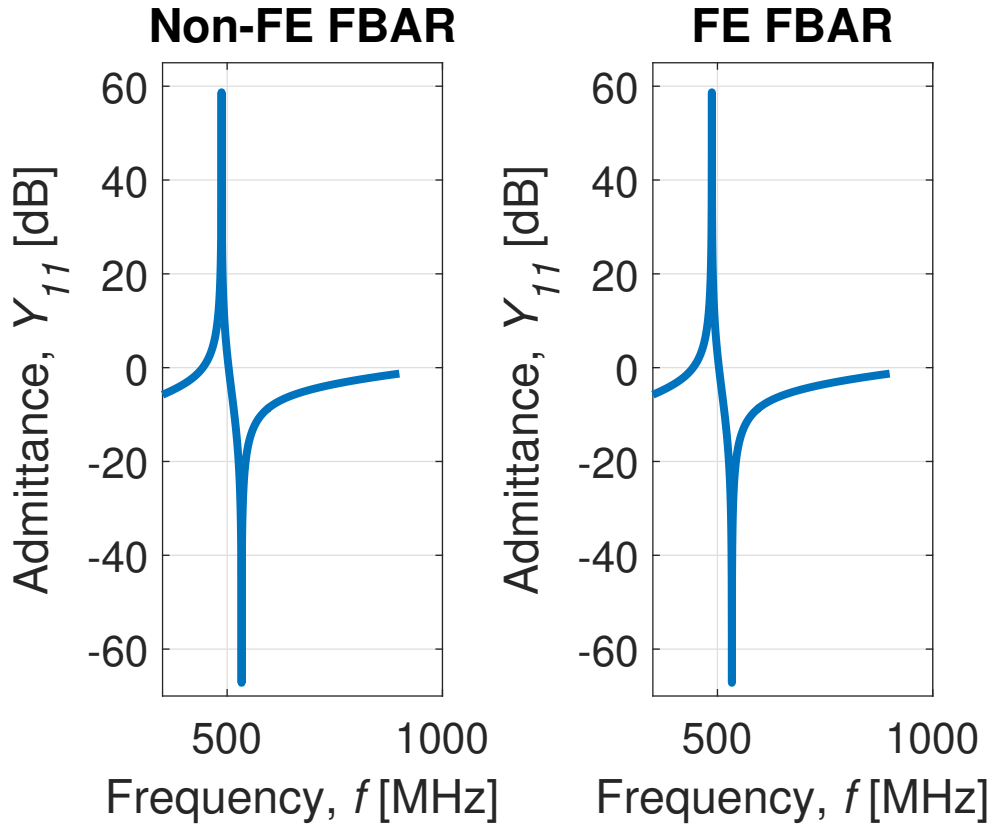


Figure 3.30: Comparison of the admittance curves of 30% ScAlN FBARs. In a), a piezoelectric resonator has been simulated. In b), the same resonator but with the ferroelectric model with $t = 0$ is shown. As it can be observed, the curves coincide.

it seems that the presence of the polarization is destroying the resonant mode, regardless of the increase in the piezoelectric coefficient.

t [s/T]	P [C/m ²]	ϵ_r	d_{33} [pC/N]
0	0	14.11	15.8
0.25	0.61	3101	9.1
0.5	1	21.7	16.66
0.75	-0.002	1485	-31.9
1	-1.05	24.32	6.79

Table 3.1: Values of time, polarization, dielectric constant and piezoelectric coefficient used in the simulation of Fig. 3.31.

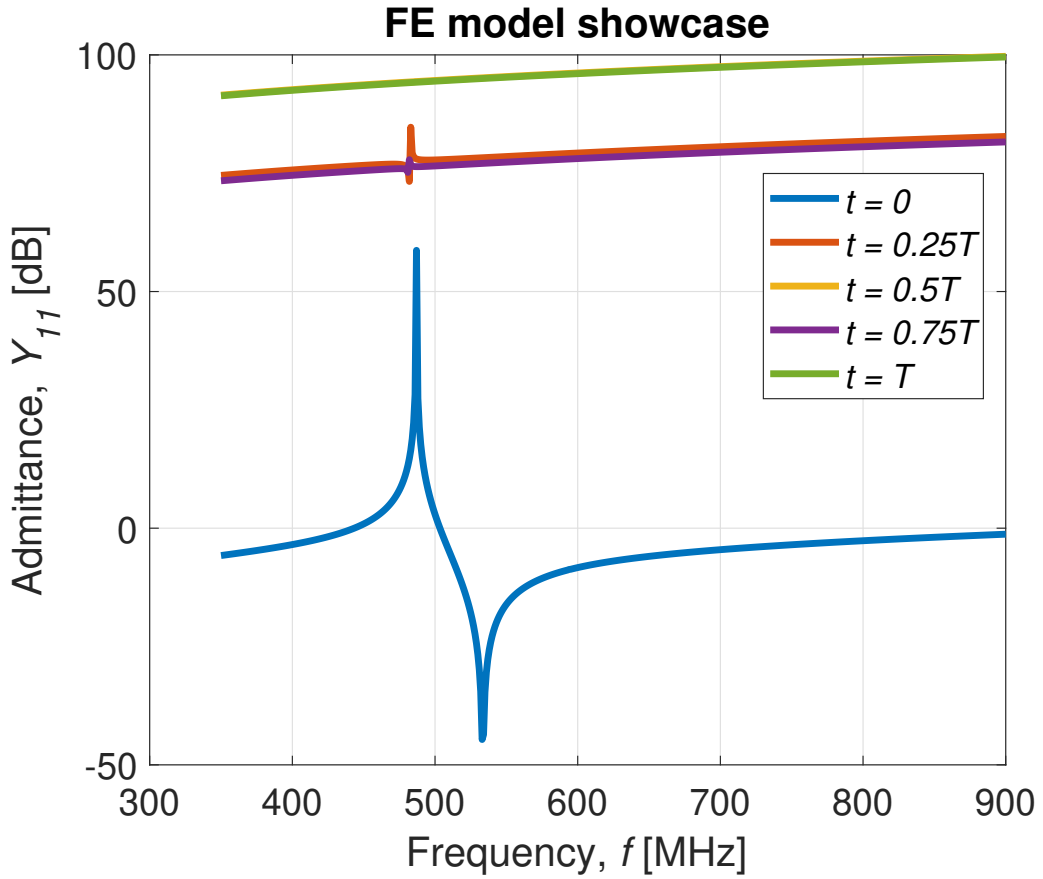


Figure 3.31: Showcase of the admittance of the ferroelectric FBAR for different times.

The results of the simulations are not yet reliable, since there has been no experimental verification. The latter would prove to be very useful to firstly better comprehend what is actually happening inside the resonator, and secondly to fine tune the model by a process of trial and errors. Nevertheless, this ferroelectric model has proven to be able to show plausible results.

Future work will be done to improve it and finally to document it. Although the early stage of development, the potentialities of the model are huge: the possibility of simulating ferroelectric structures before fabricating them will be a great improvement both for academia and industry in terms of cost-and time-efficiency. Moreover, in the framework of the DARPA project TUFEN, i.e. the one which sets the goal of extracting all the coefficients of ScAlN and then use this material to build innovative structures exploiting its ferroelectricity, this model will play a vital role.

Chapter 4

Conclusions and future work

This Section provides a brief summary of the major results and accomplishments obtained in the present Master's Thesis work. Furthermore, there is a listing of the possible future tasks that can be done following the guidelines provided in the last Chapters, posing themselves as an expansion or a refining of the Thesis work.

1. It has been shown how to numerically optimize CLMRs in order to maximize the electromechanical coupling coefficient. The optimization regards not only the geometry of the resonators, i.e. the best h/λ_x ratio, the IDT thickness and the topology, but also the possible electrode material that can be employed, even the case in which two different metals are combined. Moreover, for the first time, a systematic analysis on the impact of Sc-doping of AlN thin films on CLMR performances has been done. Experimental plans have been designed to verify the simulative analysis, and to push the resonant frequency of the devices to higher values compared to the main choices of today's technology. The aforementioned analysis has been documented in a paper presented in the IEEE conference IUS 2020.
2. Experimental results concerning the fabrication and the characterization of ScAlN thin films have been obtained, regarding both the piezoelectric and ferroelectric properties. This is of particular interest, since the topic is very new and promising, both in the field of MEMS devices and in the one of ferroelectric memories.
3. The first prototype of a COMSOL model able to simulate ferroelectric materials has been developed. This model is in accordance with experimental results obtained on ScAlN. Moreover, the model has been embedded in the simulation

of ferroelectric MEMS resonators, giving plausible results. The variations of the piezoelectric coefficient d_{33} and of the dielectric permittivity have been included.

4. Simple and handy models to estimate the static capacitance and the parasitic resistance of CLMRs have been developed and included as Appendices.

Concerning the future work, the next steps are:

1. As regards the CLMR optimization, the designs have to be fabricated and tested to experimentally verify the obtained results. After that, the optimization can be extended to the quality factor, which has been put in second place compared to the electromechanical coupling coefficient, the real focus of the present optimization work.
2. Regarding the ScAlN characterization, further data points concerning the evolution of the mechanical and dielectric properties with film thickness and Sc concentration have to be gathered, with *ad hoc* suspended resonators test structures. The whole study, starting from the films fabrication up to its complete fabrication, will be documented in a journal paper.
3. Concerning the ferroelectric model, the first step to be taken is its experimental validation concerning the simulation of ferroelectric resonators. Moreover, after obtaining experimental results on ScAlN constants, they can be added to refine it. In particular, a refining of the piezoelectric and dielectric constants is expected, together with the introduction of the variation of the mechanical properties. Finally, as regards the simulation of ScAlN, a single model able to take into account all the doping levels is expected to be developed and documented in a paper.

Chapter 5

Appendix A: Modeling of the static capacitance of CLMRs

As stated in Section 1.3, in most of applications involving resonators or resonator filters, some sort of matching is desired. The reason is to transfer to the load the maximum amount of power as possible, i.e. minimize power reflections between the source and the load. To achieve such condition, the following relation must be satisfied:

$$Z_{Load} = Z_{Source}^* \quad (5.1)$$

where Z represents the impedance and the superscript $*$ indicates the complex conjugate. The most common value for the impedance of the source is 50Ω . Therefore, in general, resonators and filter have to be 50Ω -matched. For piezoelectric resonators modeled through the BVD model, this means that:

$$\frac{1}{2\pi C_0 f_{res}} = 50\Omega \quad (5.2)$$

where C_0 is the static capacitance. Thus, its value is the one that has to be properly engineered to match the devices. Therefore, a way to model C_0 has to be found.

As an example, let's see how the static capacitance is modeled in the case of an FBAR. This is probably the simplest case: as shown in Fig. 5.1, C_0 is nothing more than the capacitance of a parallel plate capacitor made by the electrodes with the piezoelectric film between them. The formula is shown inside the figure, where A is the area of the electrodes, d is the piezoelectric thickness, ϵ_0 and ϵ_r are the dielectric permittivities of vacuum and of the piezo-layer, respectively.

The case of a CLMR is more complicated. As stated in Section 2.2, in order to tune its resonant frequency, the horizontal acoustic wavelength λ_x is tuned. This means changing the width of the resonator which, in order to reach higher frequencies, is extremely thinned. This results in a conspicuous reduction of the static capacitance, which cannot match the required 50Ω . In order to match CLMRs, several unit cells are mechanically coupled through the employment of IDTs. The resulting capacitance is the sum of the ones of the single cells, while the resonant frequency is not changed. Actually, also the capacitance between the cells has to be taken into account.

As mentioned in Section 2.2, three CLMR configurations have been studied in the present work: TFE, LFE and BE CLMR. In order to match each of them, a model for C_0 has been developed. Intuitively, among other things, the capacitance is determined by the length of the electrodes L_e and their number of pairs. By pair, one refers to the number of couples of opposite polarity IDT fingers. In particular, in the LFE and BE CLMR this number will coincide to the total number of fingers minus one, while for the TFE case, the number of pairs is exactly the number of fingers of one of the two IDTs.

Let's start with the simplest case, i.e. the LFE CLMR. Its unit cell is shown in Fig. 5.2. As in Fig. 5.1, a lumped capacitor has been added to visualize from where the capacitance originates. The simplest way to model the capacitance is using the formula of the parallel plate capacitor between the electrodes. Nevertheless, in [37] a more complicated yet more precise model to describe the capacitance of LFE capacitors has been developed and is reported here. It will be referred as the

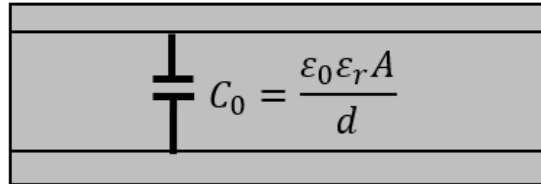


Figure 5.1: Showcase of the static capacitance of an FBAR.

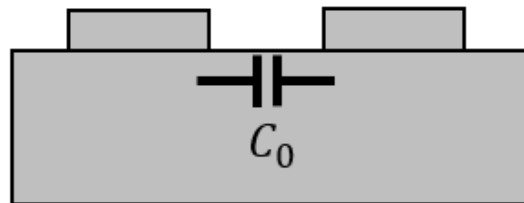


Figure 5.2: Showcase of the static capacitance of a LFE CLMR.

'Elliptic integral model' in the following. According to it, the capacitance per unit length between two electrodes can be expressed as:

$$\overline{C} = \varepsilon_0 \varepsilon_{eff} \frac{K(k'_0)}{K(k_0)} \quad [F/m] \quad (5.3)$$

where $K(k)$ is the complete elliptic integral of the first kind and k is the elliptic integral function. In particular, k_0 and k'_0 can be calculated as:

$$k_0 = \frac{g}{W_e + g} \quad (5.4)$$

$$k'_0 = \sqrt{1 - k_0^2} \quad (5.5)$$

where W_e is the width of the electrode and g is defined as:

$$g = \frac{(1 - \alpha)p}{2} \quad (5.6)$$

where α is the metallization ratio and p the pitch. So g is nothing more than the part of the pitch not occupied by the electrode divided by two. The relative permittivity ε_{eff} is calculated as:

$$\varepsilon_{eff} = 1 - (\varepsilon_{piezo} - 1)q_1 \quad (5.7)$$

where q_1 has the form:

$$q_1 = \frac{1}{2} \frac{K(k'_1)K(k_0)}{K(k_1)K(k'_0)} \quad (5.8)$$

and k_1 and k'_1 are:

$$k_1 = \frac{\tanh(\frac{\pi g}{2h})}{\tanh(\frac{\pi(W_e + g)}{2h})} \quad (5.9)$$

$$k'_1 = \sqrt{1 - k_1^2} \quad (5.10)$$

being h the film thickness.

In order to find the total static capacitance of the resonator, the result of Eq. 5.3, i.e. the capacitance density per unit length per pair, is then multiplied by the IDT length and the number of pairs. The reason is that all the lumped capacitances calculated are in parallel.

$$C_0 = \overline{C}_0 \cdot N_p \cdot L_e \quad (5.11)$$

The case of the TFE CLMR is shown in Fig. 5.3. As it can be observed, the lumped capacitors are now four: two for the lateral field (C_{0LAT}) and two for the

vertical (C_{0VERT}). In the TFE configuration, with electrode pair is meant the couple made by the top IDT finger and the corresponding bottom one. Therefore, Fig. 5.3 is showing two pairs. The reason is to take into account the interactions between the various pairs, i.e. the lateral field capacitances. Their value is computed in the same way as the previous case, i.e. with the Elliptic integral model and they are all in parallel. Concerning the vertical capacitors, their capacitance density value can be computed with the formula of the parallel plate one:

$$\overline{C_{0VERT}} = \varepsilon_0 \varepsilon_r \frac{W_e}{h} \quad (5.12)$$

Also in this case, all the capacitors are in parallel, and are in parallel with the lateral ones. For each couple two C_{0LAT} are included. Therefore, the resulting capacitance density is then:

$$\overline{C_0} = 2 \overline{C_{0LAT}} + \overline{C_{0VERT}} \quad (5.13)$$

The final capacitance value, in order to take into account the correct number of C_{0LAT} has to be reduced by two of the letters:

$$C_0 = \overline{C_0} \cdot N_p \cdot L_e - 2 \overline{C_{0LAT}} \cdot L_e \quad (5.14)$$

Finally, the BE CLMR case is shown in Fig. 5.4. It is a bit trickier due to the presence of the floating BE. As in the LFE case, a pair is made by two adjacent

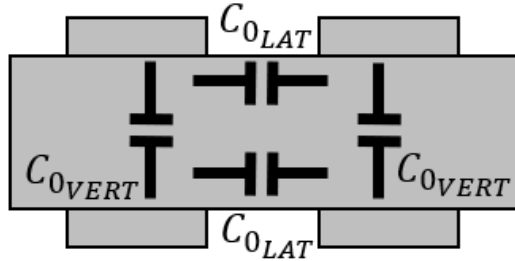


Figure 5.3: Showcase of the static capacitance of a TFE CLMR.

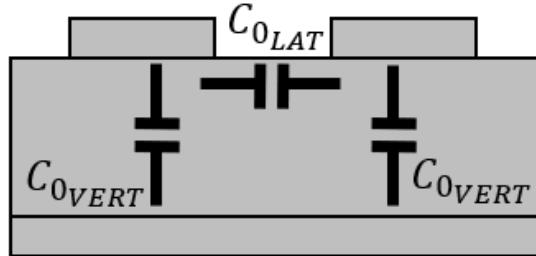


Figure 5.4: Showcase of the static capacitance of a BE CLMR.

and opposite-polarities electrodes. The lateral field capacitance is computed with the Elliptic integral model, and for each pair the contributions are in parallel. Concerning the vertical capacitances, they are computed with Eq. 5.12. As shown in the figure, there are two for each pair. Being the BE floating, they are in series. Nevertheless, before putting them in series, the C_{0VERT} associated to all the electrodes of the same polarity are in parallel. To be more clear let's consider the case of four electrodes: there would be three C_{0LAT} in parallel with the series of the parallel of two C_{0VERT} . The schematic of this example is shown in Fig. 5.5. Therefore, the final formula to compute the capacitance is:

$$C_0 = \overline{C_{0LAT}} N_p \cdot L_e + \overline{C_{0VERT}} \cdot L_e \cdot \frac{N_p}{4} \quad (5.15)$$

With this very simple and approximated model, one can estimate the correct number of fingers and/or the IDT length required to have the desired impedance matching.]

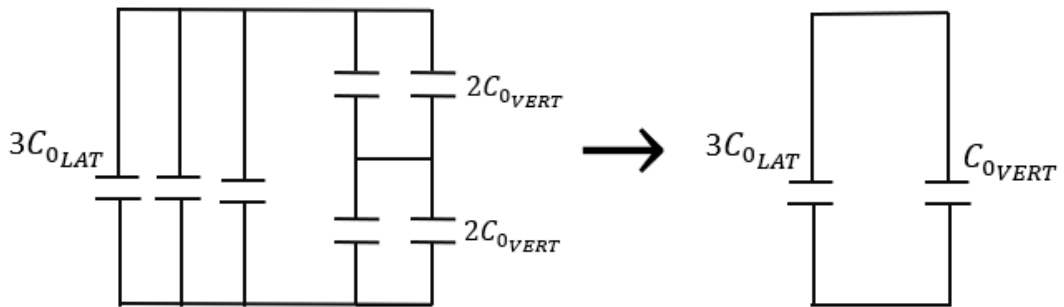


Figure 5.5: Example of the schematic of the capacitance for a BE CLMR with four electrodes (three pairs).

Chapter 6

Appendix B: Modeling of the parasitic resistance of CLMRs

As mentioned in Section 2.6, in order to design high quality factor resonators, the losses due to electrical loading have to be taken into account. In the experimental plan designed on AlN, those loss mechanisms have to be carefully mitigated due to the high resistivity of Pt, the employed electrode material. It is not the case of the ScAlN one, in which there is the usage of Al as top electrode which, having a very low resistivity, is not the main quality factor limiter.

The sources of electrical loading are both the IDTs and the routing. Given R_m the BVD motional resistance of the resonator, and R_s the parasitic resistance introduced by the finite resistivity of the metal, the equation defining the loaded quality factor, i.e. the final Q measured by the VNA is [38]:

$$Q_l = Q_u \frac{R_m}{R_m + R_s} \quad (6.1)$$

where Q_u is the unloaded quality factor, i.e. the one obtained if the metal introduced no resistance. From this equation it is straightforward to notice that, if R_m and R_s are comparable, the Q is severely limited, and therefore the losses are increased.

In order to have an estimation of the parasitic resistance, a simple lumped model has been developed. In this model, all the routing and IDTs have been treated as separate elements and their resistance put in series. In particular, let's consider as a showcase the structure of a TFE CLMR. Indications on how to extend it to the other CLMR topologies are given in the following. Given the structure of a resonator as it appears on the GDSII file, let's identify the various sources of

electrical loading. They are shown in Fig. 6.1 on the left. On the right, the series of the lumped resistors modeling each routing component is shown.

Let's now analyze each contribution singularly and compute their resistances using the simple formula:

$$R = \rho \frac{L}{S} \quad (6.2)$$

where ρ is the metal resistivity, S the cross-section and L the length of each routing component.

1. **PAD**: the pad is a simple square of metal used to land the probe in the measuring phase. Its resistance will be:

$$R_{pad} = \rho \frac{L_{pad}/2}{W_{pad}t} \quad (6.3)$$

where L_{pad} , W_{pad} and t are the length, width and thickness of the pad, respectively. The pad thickness is the same as all the other interconnects taken into consideration.

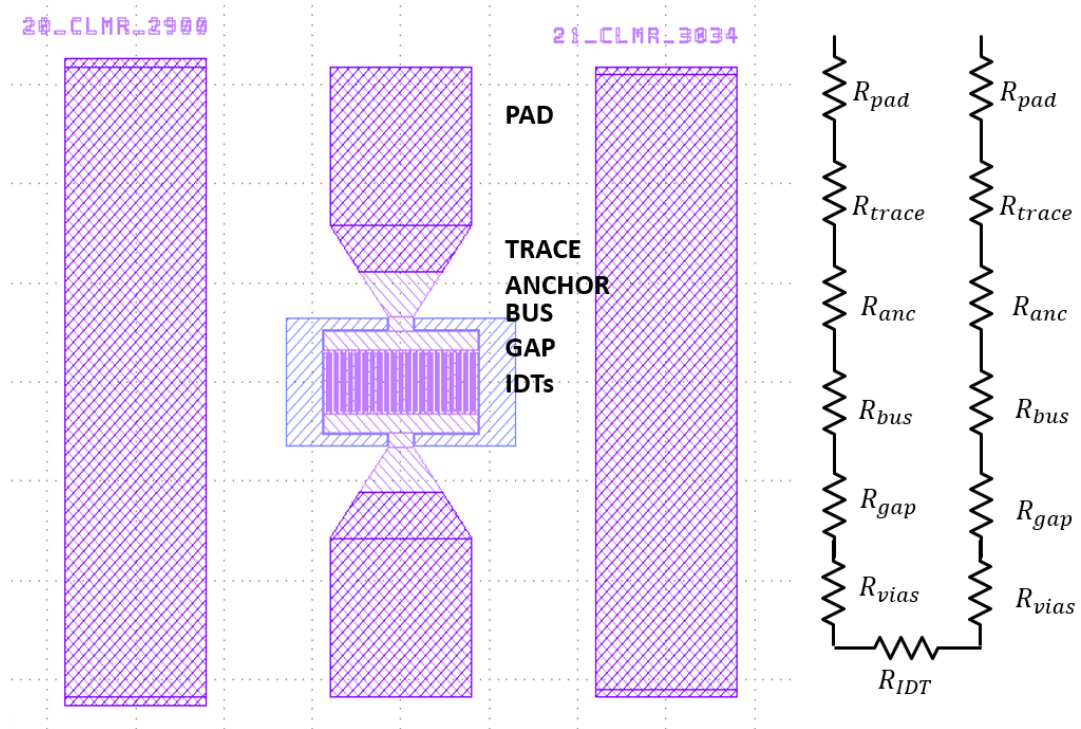


Figure 6.1: Left: visualization of the routing elements that introduce electrical loading as they appear on the GDSII file. On the right, the complete lumped model of the resistance of a CLMR.

2. **TRACE**: the traces connect the pads to the anchors of the resonator. In the current implementation, they consist of a trapezoidal structure. The resistance that introduce is:

$$R_{trace} = \rho \frac{L_{trace}}{\frac{W_{pad} + W_{anc}}{2} t} \quad (6.4)$$

where L_{trace} is the trace length and W_{anc} is the anchor width.

3. **ANCHOR**: the anchor is simply a block that connects the suspended resonator to the substrate. In order to transfer the electrical signal to the IDTs, also the anchors have metallic interconnections and introduce a parasitic resistance given by:

$$R_{anc} = \rho \frac{L_{anc}}{W_{anc} t} \quad (6.5)$$

where L_{anc} is the anchor length.

4. **BUS**: the bus provides the routing of the electrical signal to the IDT fingers. Its resistance is computed by shunting the two bus branches, each of which with a resistance of $R_{bus}/2$, where R_{bus} is:

$$R_{bus} = \rho \frac{L_{bus}}{W_{res} t} = \rho \frac{L_{bus}}{N_f \frac{\lambda_x}{2} t} \quad (6.6)$$

where L_{bus} is the bus length, W_{res} the resonator width and N_f the number of fingers.

5. **GAP**: the gap is the portion of the IDT which is not interdigitated and, together with the above mentioned resonator components, is part of the inactive region. All the fingers are considered in parallel.

$$R_{gap} = \rho \frac{L_{gap}}{W_{el} t} \frac{1}{N_f} = \rho \frac{L_{gap}}{\frac{\lambda_x}{2} c t} \frac{1}{N_f} \quad (6.7)$$

where L_{gap} is the gap length, W_{el} the electrode finger width and c the coverage.

6. **VIAS**: the vias are the electrical connections between the top and bottom electrode. Their resistance is generally a few Ohms, and in the present work has been considered as equal to 1Ω . In the case of LFE and BE CLMRs, there are no vias and so no R_{vias} contribution.

7. **IDTs**: the IDTs constitute the active region of the resonator, and are responsible for the transduction. Their resistance is computed as:

$$R_{IDT} = \frac{2}{3} \rho \frac{L_{IDT}}{W_{el} t} \frac{1}{N_f} = \frac{2}{3} \rho \frac{L_{IDT}}{\frac{\lambda_x}{2} c t} \frac{1}{N_f} \quad (6.8)$$

where L_{IDT} is the IDT length, and the factor $2/3$ arises from the progressive loss of charge inside the fingers, which makes them have a resistance as if their length were $2/3$ of the real one. In this kind of resonators, R_{IDT} constitutes the main source of parasitic resistance.

To sum up, Fig. 6.2 shows all the lumped elements and their resistance.

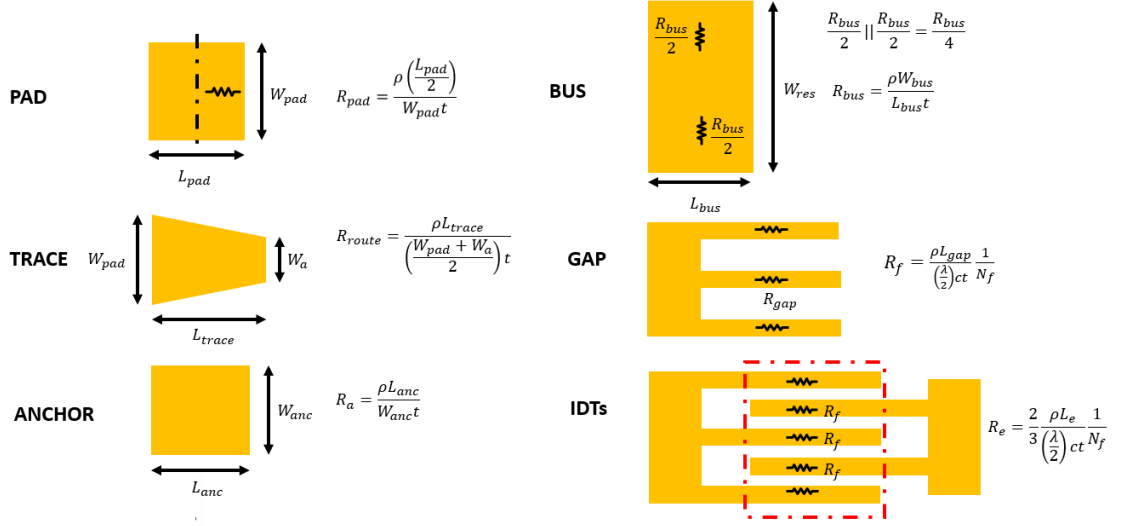


Figure 6.2: All the lumped model contributions to the parasitic resistance in a CLMR with the relative equations. The VIAs resistance is missing since it has been considered to the fixed value of 1Ω .

This model is very simple to be understood and implemented, and provides an estimation of the parasitic resistance, very useful in the design phase.

Bibliography

- [1] Yole Développement. «MEMS Markets: Status of the MEMS Industry—Market Technology Report». In: 2018 (cit. on p. 1).
- [2] Yilong Hao and Dacheng Zhang. «Silicon-based MEMS process and standardization». In: *Proceedings. 7th International Conference on Solid-State and Integrated Circuits Technology, 2004*. Vol. 3. 2004, 1835–1838 vol.3 (cit. on p. 1).
- [3] «MEMS MARKET - GROWTH, TRENDS, AND FORECAST (2020 - 2025)». In: 2019 (cit. on p. 1).
- [4] H. C. Nathanson, W. E. Newell, R. A. Wickstrom, and J. R. Davis. «The resonant gate transistor». In: vol. 14. 3. 1967, pp. 117–133 (cit. on pp. 2, 3).
- [5] B. Bahreyni J. Lee R. Abdolvand and F. Nabki. «Micromachined resonators: a review». In: 2016 (cit. on pp. 2, 3).
- [6] W. C. Tang, T. - H. Nguyen, and R. T. Howe. «Laterally driven polysilicon resonant microstructures». In: *IEEE Micro Electro Mechanical Systems, , Proceedings, 'An Investigation of Micro Structures, Sensors, Actuators, Machines and Robots'*. 1989, pp. 53–59 (cit. on p. 3).
- [7] D. Weinstein and S. A. Bhave. «Internal Dielectric Transduction of a 4.5 GHz Silicon Bar Resonator». In: *2007 IEEE International Electron Devices Meeting*. 2007, pp. 415–418 (cit. on p. 3).
- [8] Charles S. Smith. «Piezoresistance Effect in Germanium and Silicon». In: vol. 94. Apr. 1954, pp. 42–49 (cit. on p. 4).
- [9] S. J. Rupitsch. «Piezoelectric Sensors and Actuators». In: 2019 (cit. on pp. 5, 6, 8, 10).
- [10] J. F. Rosenbaum. «Bulk acoustic wave theory and devices». In: 1988, pp. 389–391 (cit. on p. 10).
- [11] G. Piazza H. Bhugra. «Piezoelectric MEMS Resonators». In: 2017 (cit. on p. 11).

- [12] C. Cassella, Y. Hui, Z. Qian, G. Hummel and M. Rinaldi. «Aluminum Nitride Cross-Sectional Lamé Mode Resonators». In: *Journal of Microelectromechanical Systems*. Vol. 25. 2. Apr. 2016, pp. 275–285 (cit. on pp. 12, 25, 26, 28).
- [13] K. Kurokawa. «Power Waves and the Scattering Matrix». In: vol. 13. 2. 1965, pp. 194–202 (cit. on p. 12).
- [14] G. Piazza, P. J. Stephanou, and A. P. Pisano. «Single-Chip Multiple-Frequency ALN MEMS Filters Based on Contour-Mode Piezoelectric Resonators». In: vol. 16. 2. 2007, pp. 319–328 (cit. on pp. 15, 16).
- [15] S. Fichtner, N. Wolff, F. Lofink, B. Wagner. «AlScN: A III-V semiconductor based ferroelectric». In: *Journal of Applied Physics*. 2019 (cit. on pp. 16, 59, 60, 62, 72, 77).
- [16] D. Damianovich. «Ferroelectric, dielectric and piezoelectric properties of ferroelectric thin films and ceramics». In: 1998 (cit. on pp. 16, 18–20).
- [17] R. Ruby and P. Merchant. «Micromachined thin film bulk acoustic resonators». In: *Proceedings of IEEE 48th Annual Symposium on Frequency Control*. 1994, pp. 135–138 (cit. on p. 21).
- [18] Matteo Rinaldi, Chiara Zuniga, Chengjie Zuo, and Gianluca Piazza. «Super-High-Frequency Two-Port AlN Contour-Mode Resonators for RF Applications». In: *IEEE Transactions on Ultrasonics, Ferroelectrics, and Frequency Control*. Vol. 57. 1. Jan. 2010 (cit. on p. 24).
- [19] J. Zou, C. Lin, C. S. Lam, and A. Pisano. «Transducer design for AlN Lamb wave resonators». In: *Journal of Applied Physics*. Vol. 121. 2017 (cit. on pp. 28–30, 36, 38).
- [20] L. Colombo, A. Kochhar, C. Xu, G. Piazza, S. Mishin, and Y. Oshmyansky. «Investigation of 20% scandium-doped aluminum nitride films for MEMS laterally vibrating resonators». In: *2017 IEEE International Ultrasonics Symposium (IUS)*. 2017, pp. 1–4 (cit. on pp. 28, 33).
- [21] Z. A. Schaffer, G. Piazza, S. Mishin, and Y. Oshmyansky. «Super High Frequency simple process flow Cross-sectional Lamé Mode Resonators in 20% Scandium-Doped Aluminum Nitride». In: *MEMS 2020* (cit. on pp. 30, 33).
- [22] M. A. Caro, S. Zhang, T. Riekkinen, M. Ylilampi, M. A. Moram, O. Lopez-Acevedo, J. Molarius, and T. Laurila. «Piezoelectric coefficients and spontaneous polarization of ScAlN». In: *Journal of Physics: Condensed Matter*. Vol. 27. 24. May 2015 (cit. on pp. 32, 33, 35, 75, 78, 80).

- [23] X. Zhao and C. Cassella. «On the Coupling Coefficient of ScyAl_{1-y}N-based Piezoelectric Acoustic Resonators». In: *2019 Joint Conference of the IEEE International Frequency Control Symposium and European Frequency and Time Forum (EFTF/IFC)*. 2019, pp. 1–4 (cit. on p. 33).
- [24] M. Akiyama, K. Nagao, N. Ueno, H. Tateyama, T. Yamada. «Influence of metal electrodes on crystal orientation of aluminum nitride thin films». In: *Vacuum*. Vol. 74. June 2004, pp. 699–703 (cit. on p. 42).
- [25] C. Cassella, N. Singh, B. W. Soon, and G. Piazza. «Quality Factor Dependence on the Inactive Regions in AlN Contour-Mode Resonators». In: vol. 24. 5. 2015, pp. 1575–1582 (cit. on p. 48).
- [26] J. Segovia-Fernandez and G. Piazza. «Analytical and Numerical Methods to Model Anchor Losses in 65-MHz AlN Contour Mode Resonators». In: vol. 25. 3. 2016, pp. 459–468 (cit. on p. 49).
- [27] C. Cassella, G. Chen, Z. Qian, G. Hummel, M. Rinaldi. «Cross-Sectional Lamé' Mode Ladder Filters for UHF Wideband Applications». In: *IEEE Electron Device Letters*. Vol. 37. 5. May 2016 (cit. on p. 58).
- [28] G. Chen, C. Cassella, T. Wu, M. Rinaldi. «Single-Chip Multi-Frequency Wideband Filters Based on Aluminum Nitride Cross-Sectional Lamé' Mode Resonators with thick and apodized electrodes». In: *IEEE MEMS 2018* (cit. on p. 58).
- [29] M. Zolfagharloo Koochi and A. Mortazawi. «Reconfigurable Radios Employing Ferroelectrics». In: 2020 (cit. on pp. 61–63).
- [30] T. Schenk, U. Schroeder, and T. Mikolajick. «Correspondence - Dynamic leakage current compensation revisited». In: *IEEE Transactions on Ultrasonics, Ferroelectrics, and Frequency Control* 62.3 (2015), pp. 596–599 (cit. on p. 77).
- [31] A. De Andes A. Lopez and P. Ramos. «Finite Element Model of a Ferroelectric». In: 2010 (cit. on pp. 79, 80).
- [32] S. Hong K. Lim K. Kim and K. Lee. «A semi-empirical cad model of ferroelectric capacitor for circuit simulation». In: vol. 17. 1997, pp. 97–104 (cit. on p. 79).
- [33] C. Alemany R. Jimenez M. Calzada. «Processing effects on the microstructure and ferroelectric properties of strontium bismuth tantalate thin films». In: vol. 75. 2002, pp. 607–615 (cit. on p. 80).
- [34] H. El Hisiny et al. «The role of PbTiO₃ layers in piezoelectric multilayer composite films based on Pb(Mg_{1/3}Nb_{2/3})O₃-PbTiO₃». In: 2017 (cit. on p. 82).

- [35] B. Shrestha. «Modeling Polarization and Capacitance Hysteresis of Ferroelectric Capacitors». In: 2012 (cit. on pp. 84–86, 88, 90).
- [36] Y.-L. Wang et al. «Simulation of Hysteresis Loops for Polycrystalline Ferroelectrics by an Extensive Landau-Type Model». In: vol. 373. 2009 (cit. on p. 85).
- [37] Amr Nassr, Wael Ahmed, and Wael El-Dakhakhni. «Coplanar capacitance sensors for detecting water intrusion in composite structures». In: vol. 19. June 2008 (cit. on p. 100).
- [38] L. Colombo, A. Kochhar, G. Vidal-Álvarez, and G. Piazza. «High-Figure-of-Merit X-Cut Lithium Niobate MEMS Resonators Operating Around 50 MHz for Large Passive Voltage Amplification in Radio Frequency Applications». In: vol. 67. 7. 2020, pp. 1392–1402 (cit. on p. 104).